UNIVERSITÀ DEGLI STUDI DI PADOVA

Dipartimento di Fisica e Astronomia "Galileo Galilei"

Master Degree in Physics

Final Dissertation

Follow-Up Analysis of Icecube Neutrino Alerts:

new approaches to increase the signal-to-noise ratio

Thesis supervisor
Prof. Elisa Bernardini

Candidate
Elena Manao

Academic Year 2021/2022

Contents

Abstract

The breakthrough discovery of an astrophysical flux of neutrinos between TeV and PeV energies with the IceCube experiment in the year 2013 is a milestone in multi-messenger astrophysics. Identifying the sources of this cosmic flux remains to date a challenge. Traditional time-integrated searches for point-like sources of neutrinos showed evidence of cumulative excess of events with respect to the expected atmospheric neutrino background in correspondence of four known sources, in order of importance NGC 1068, TXS 0506+056, PKS 1424+240 and GB6 J1542+6129. However, the significance of such excesses, 3.3σ, is still too low to announce the discovery of a source of astrophysical neutrinos.

Several astrophysical scenarios are considered good as candidate neutrino emitters and, among those, a good fraction exhibits large variations in their non-thermal electromagnetic emission. This suggests that neutrino signals shall likely be variable in time as well.

The IceCube Neutrino Observatory features the capability to observe the entire sky with a full-duty cycle. This opportunity enables to continuously search for transient neutrino emissions and alert the astrophysical community with the lowest possible latency in case of detection of potential astrophysical neutrinos. To ensure good efficiency in collecting possible neutrino flares, IceCube implemented an infrastructure that generates alerts whenever a flare is detected above a predefined significance threshold.

In September 2017, the IceCube neutrino alert produced by the IC170922A event triggered follow-up observations over a wide range of frequencies, from radio to gamma-ray energies, which found the neutrino event to be coincident with the known blazar TXS 0506+056, observed to be in a flaring state. The chance coincidence of these events is statistically disfavoured at the level of 3σ, meaning that TXS 0506+056 is a candidate source of neutrinos. Additionally, this observation demonstrated the potentialities of real-time multi-messenger studies.

To increase the coverage of electromagnetic data during potential neutrino flares, the alerts are being distributed to the astrophysical community with a relatively low threshold on the significance. As a consequence, the majority of the alerts are expected to be due to statistical fluctuations of the background.

This thesis focuses on the development of new strategies for a follow-up analysis of real-time IceCube alerts to single out a possible sample of pure astrophysical neutrino flares. The main challenge will be represented by mitigating the consequent loss in signal collection efficiency.

First of all, a detailed study of the performances of the core algorithm and of the typical characteristics of the alerts are performed. Then, new strategies to increase the signal-to-noise ratio of the alerts are considered, focusing, in particular, on the conditions the neutrino events need to fulfil to trigger the analysis. Different tests are performed and the effects on the performance of the algorithm and on the characteristics of the neutrino alerts are discussed.

Chapter 1

Introduction

The discovery of cosmic rays by Victor Hess in 1912 [1] marked the beginning of a new branch of physics, astroparticle physics, which focuses on the study of high energy particles produced in astrophysical sources.

Despite the discovery of this radiation dates back to more than a century ago, its origin is yet to be fully understood, especially for what concerns extreme high energy signals, that are expected to be produced in cosmic accelerators, following some of the most abrupt phenomena in the Universe.

Not only charged particles are produced in such environments, but also photons and neutrinos have been proven to contribute to the non-thermal radiation coming from astrophysical sources. All of these particles are known as cosmic messengers, and the branch of astrophysics that studies the combined information obtained from different messengers is called multi-messenger astrophysics.

Among all, neutrinos are the messenger whose signature provides the most interesting information about the origin of high energy cosmic radiation. In fact, they are produced after the interaction of cosmic rays with a dense target, and, being very weakly interacting, they can travel enormous distances without being deflected, thus they represent a direct probe of high energy processes in astrophysical sources.

The detection of astrophysical neutrinos is particularly challenging because of the high background and low fluxes, and combining the information coming from different messengers could help increase the significance of signal excesses.

The discovery of astrophysical neutrinos is quite recent, it was announced by IceCube experiment in 2013 [2]. Up to now, the search for astrophysical sources of neutrinos didn't lead to any conclusive result, but some objects are starting to emerge as candidate neutrino sources [3].

IceCube features the capability of observing the full sky with an almost 100% uptime, continuously searching for transient neutrino emissions. In order to enhance the probability of multi-messenger, an alert infrastructure was implemented to notify the astrophysical community whenever a significant neutrino event is detected [4].

In September 2017, a neutrino alert allowed the multi-messenger observation of a high energy neutrino in coincidence with the flaring blazar TXS 0506+056. Thanks to this observation, which proved the potentialities of real-time multi-messenger studies, blazars are now considered candidate sources of astrophysical neutrinos [5].

In order to favour similar detections, IceCube Neutrino Observatory is currently involved in the *Gamma-ray Follow-Up* program, which aims at identifying neutrino flares coming from known gamma-ray emitters in real-time and notify significant detections to Imaging Air Čerenkov Telescopes (IACTs) with the smallest possible latency sending the so-called *GFU neutrino alerts* for follow-up observations. However, to increase the coverage of electromagnetic data, these alerts are released with a relatively low threshold on their significance, thus the majority of them are due to background fluctuations.

This work focuses on the development of new approaches to increase the signal-to-noise background of IceCube neutrino alerts, with the purpose of outlining a sample of astrophysical pure neutrino flares. This will be done by acting on the conditions that the events need to fulfil in order to trigger the analysis that produces the GFU alerts.

This thesis is structured as follows: in Chapter 2 an overview of Multi-Messenger astrophysics, the cosmic messengers, and the principal detection techniques will be given, in Chapter 3 the IceCube detector will be presented, Chapter 4 is dedicated to IceCube real-time infrastructure, with a particular focus on the Gamma-ray Follow-Up (GFU) analysis, in Chapter 5 we will report the results of the test of the performances of the GFU analysis and the reproduction of the last GFU results, Chapter 6 is dedicated to the new approaches to increase the signal-to-background ratio of the neutrino alerts and, finally, in Chapter 7 we will draw our conclusions and discuss the future perspectives of neutrino astrophysics at IceCube.

Chapter 2

Multi-messenger Astrophysics

Cosmic rays are high energy charged particles that propagate through space for long distances before interacting in the Earth atmosphere producing a shower of secondary particles. Their discovery dates back to 1912, when Victor Hess measured the rate of ionising radiation at different altitudes while being on a balloon. The results showed that the ionisation rate increased with increasing altitude and, after ruling out the possibility of this radiation to be caused by the Sun, he concluded that *"The results of the observations seem most likely to be explained by the assumption that radiation of very high penetrating power enters from above into our atmosphere."* [1]

The discovery of cosmic rays marked the beginning of a new branch of physics: astroparticle physics, which focuses on the study of radiation of astrophysical origin and its relation with astrophysics and cosmology.

Cosmic rays are not the only extra-terrestrial kind of radiation that can be studied. There are four different messengers that provide insights about the nature of astrophysical phenomena. These are:

- cosmic rays
- photons
- neutrinos
- gravitational waves.

The information provided by two or more different messengers coming from the same astrophysical environment can be combined allowing for a more comprehensive understanding of the phenomena. This approach is the so-called *multi-messenger approach*.

During the past years, some of the most relevant results of multi-messenger astrophysics were achieved. In August 2017, the detection of the gravitational wave event GW170817 observed by LIGO interferometer [6] and the independent observation of a gamma-ray burst from the same direction performed by the Fermi-LAT satellite [7] allowed to observe the merger of two neutron stars and gave proof that gamma-ray bursts can be powered by this kind of events [8]. In 2017, instead, the detection of a high energy neutrino, IceCube event IC170822A, in coincidence with the observation of the flaring blazar TXS 0506+056 allowed to identify blazars as candidate neutrino sources [5].

In this cgrhapter, the most relevant characteristics of all the messengers will be introduced, with a focus on their role from a multi-messenger perspective.

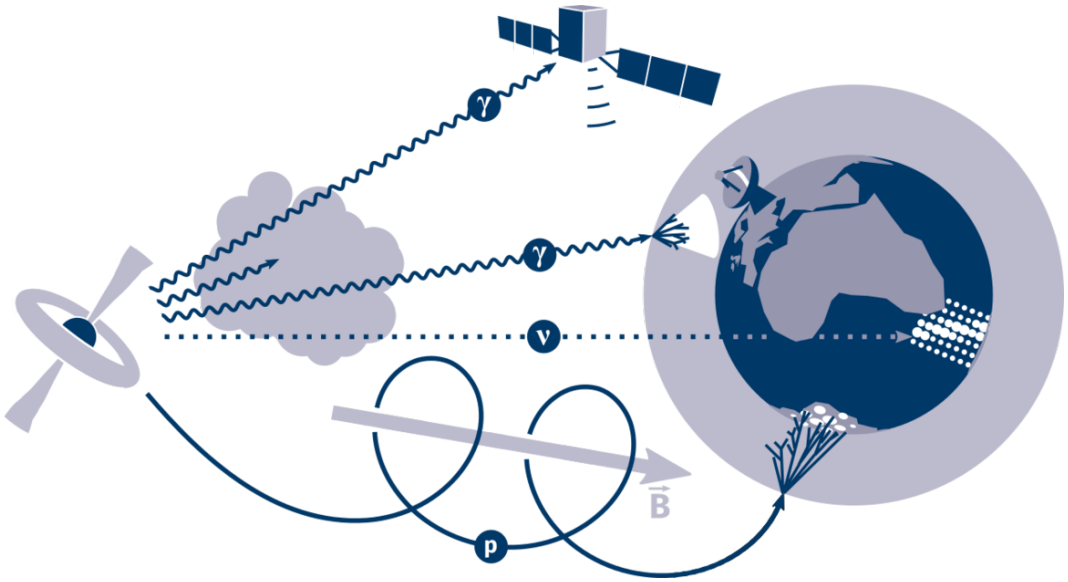

Figure 2.1: Graphic representation of possible detection techniques of different cosmic messengers. In particular, surface array detectors for cosmic rays detection, neutrino telescopes, and Air Imaging Čerenkov telescopes and satellites for high-energy are shown. (Image credit: `https://iihe.ac.be/icecube`)

2.1 Cosmic Rays

Cosmic rays are charged particles produced both in our galaxy and in extra-galactic environments that cover a wide range of energies, from the GeV scale up to hundreds of EeV, several orders of magnitude greater than the energies achievable in man-made particle accelerators. As it can be easily observed in Figure 2.2, their energy spectrum is characterised by steeping falling fluxes. So, the detection of these particles becomes more and more difficult at increasing energies. The cosmic rays spectrum can be modelled by an unbroken power law:

$$\frac{d\phi}{dE} = \phi_0 \cdot \left(\frac{E}{E_0}\right)^{\gamma} \tag{2.1}$$

where ϕ_0 and E_0 are normalisation constants and γ is the spectral index.

Some of the unsolved questions about cosmic rays regard the changes in the spectra: the so-called *knee* and *ankle*. The knee corresponds to the region of the spectra around 3 PeV energy where a change of the spectral index from ≈ -2.7 to ≈ -3.1 is observed. It is believed to be the region where extra-galactic cosmic rays take over the galactic component. The nature of the ankle, the region of the spectra around 5 EeV energy, where the spectral index becomes ≈ -2.5, is still debated.

There are different satellites and ground-based experiments dedicated to the study of cosmic rays. In the GeV and TeV energy range, where the expected rate of particles is $\approx$ 1particle/m^{2}s, satellite experiments, as, for example, AMS-02, managed to characterise properly the cosmic rays spectrum. At increasing energies, and exponentially decreasing rates, surface array detectors, such as Auger, which covers an area of 3000 km^2, are necessary to explore the properties of those particles.

Cosmic rays having energies above 1 EeV are known as *Ultra High Energy Cosmic Rays (UHECR)*. They are particularly relevant because, thanks to their extremely high energy, their trajectory is not bent while travelling through extra-galactic and galactic magnetic fields. So, these particles are able to carry information about the sources in which they

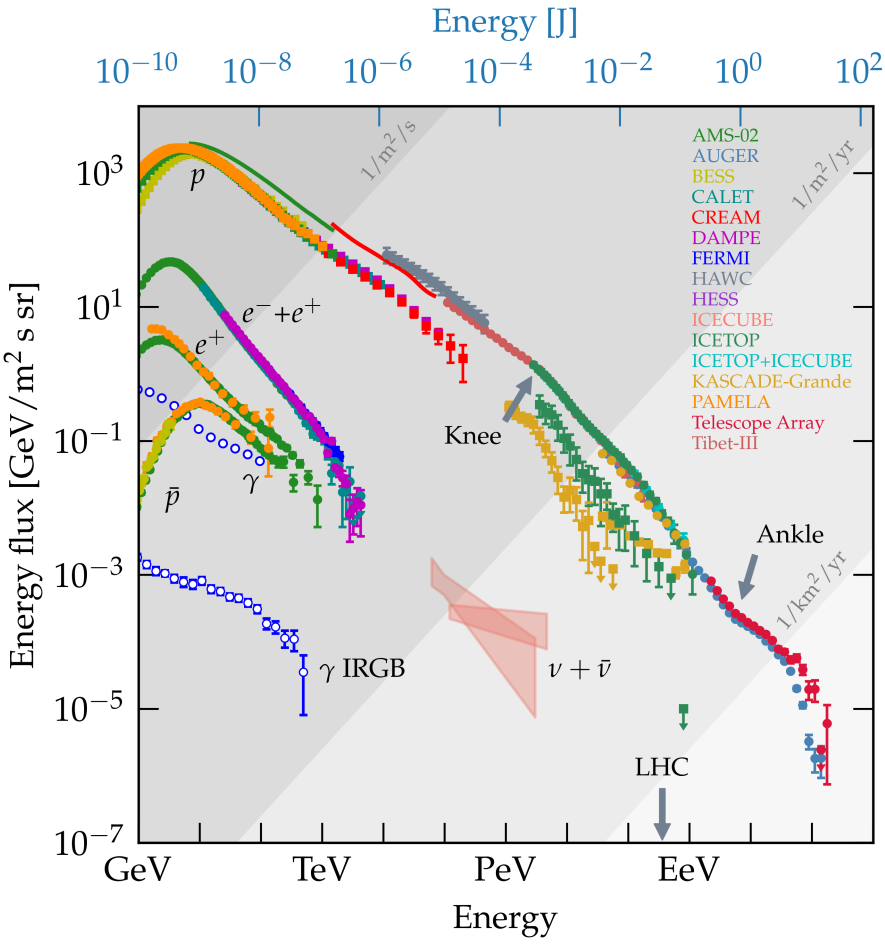

Figure 2.2: Cosmic Rays energy spectrum. Data coming from different experiments are shown. The grey shaded areas represent the expected detection rates. In this plot also the results for the leptonic component of cosmic rays, antiprotons, gamma-rays and neutrinos are shown. (Image credit: `https://tinyurl.com/68nuppwt`)

are produced, which is one of the long-standing puzzles about cosmic rays. Above 100 EeV energies, a strong suppression of the flux is observed. Its origin is an other open question regarding cosmic rays. It may be due to the fact that cosmic rays accelerators, whose functioning is yet to be understood, can not exceed this energy or to the so-called Greisen-Zatespin-Kizmin (GZK) cut-off [9], which consists in the interaction of UHECRs with a photon from the Cosmic Microwave Background (CMB) producing a Δ^+ resonance that suddenly decays in two possible channels, causing this suppression. The processes are the following:

$$p + \gamma_{CMB} \rightarrow \Delta^+ \rightarrow \begin{cases} p + \pi^0 \\ n + \pi^+ \end{cases} \tag{2.2}$$

The needed proton energy for this process to happen is $5 \cdot 10^{19}$ eV, and this kind of interaction is supposed to be happening for any proton that has energy exceeding this threshold.

Charged particles produced in astrophysical environments that strike onto our planet are known as *primary* cosmic rays. Primary cosmic rays are mainly composed of hadrons (98%) and, only for a small fraction (2%), of leptons. The hadronic component is primarily made of protons (88%), α particles are also a relevant component (11%), and the remaining fraction is made of heavier nuclei (Z>2) and a small fraction of anti-protons.

Primary particles are very likely to interact with heavy nuclei in the atmosphere. The inter-

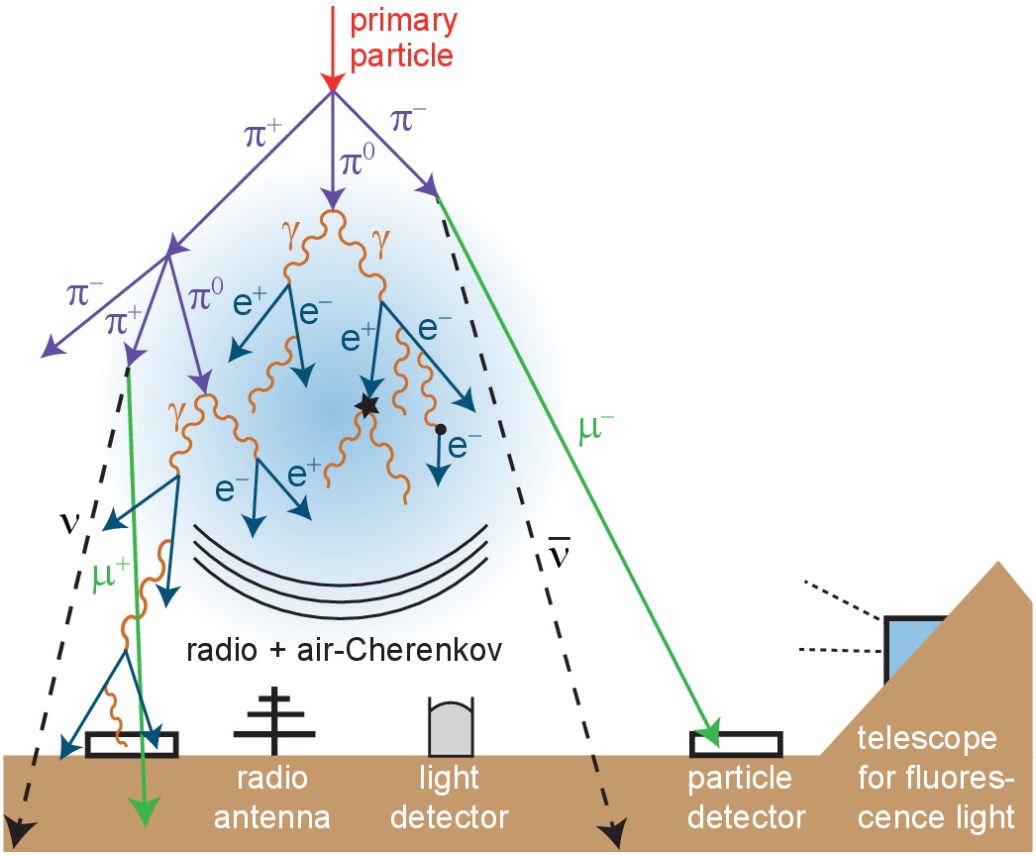

Figure 2.3: Sketch of the development of a hadronic air shower. Assuming the primary particle is a proton, right after the interaction the most abundant particles in the shower will be pions, which will decay according to (2.3) and (2.4). The products of the decays will then decay or interact until their detection or absorption in the atmosphere. Taken from [10].

action produces the so-called particle showers, which are made of protons, neutrons, mesons and low mass nuclei. Among all, mesons produced from the interaction of primary cosmic rays quickly decay into charged and neutral pions, the lightest mesons. The development of a hadronic air shower is displayed if Figure 2.3. Neutral and charged pions will be the major component of air showers soon after the interaction takes place. Neutral pion decay in almost 100% of cases in two photons:

$$\pi^0 \rightarrow \gamma + \gamma \tag{2.3}$$

while charged pions will decay in a muon-neutrino pair as it follows:

$$\begin{aligned} \pi^+ &\rightarrow \mu^+ + \nu_\mu \\ \pi^- &\rightarrow \mu^- + \bar{\nu}_\mu \end{aligned} \tag{2.4}$$

producing the so-called atmospheric neutrinos. Additional atmospheric neutrinos will then be produced in the (anti)muon decay. Those neutrinos are particularly relevant for this work because they constitute the major source of irreducible background for the analysis treated in this work. In fact, the analysis carried out in this work aims at identifying astrophysical neutrino flares, which, as we will see in the next section, have similar characteristics to those of atmospheric neutrinos.

The last open question about cosmic rays that we need to introduce for the purpose of this work addresses the acceleration mechanism of cosmic rays. For what concerns galactic cosmic rays, the Sun and Supernovae remnants (SNRs) are believed to be candidate sources of

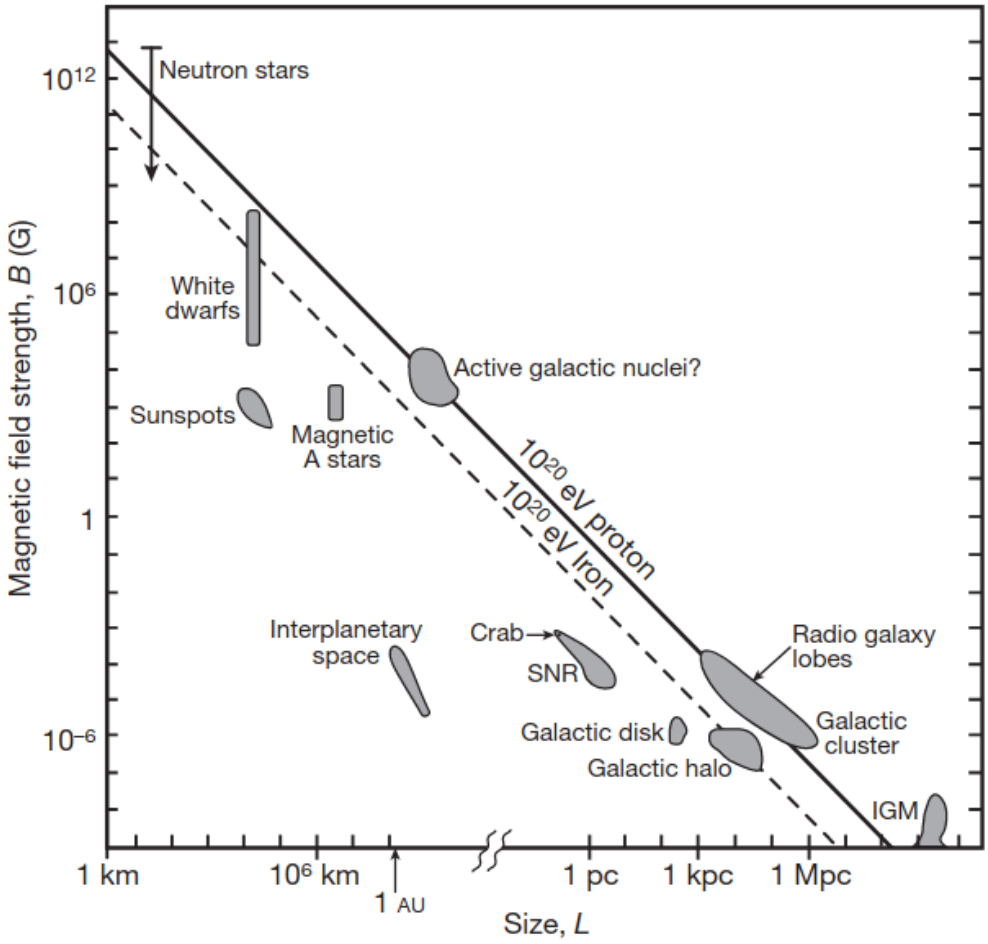

Figure 2.4: Hillas diagram. The diagram shows the candidate sites of acceleration of UHECRs as a function of their size and their magnetic field. Taken from [14].

cosmic rays [11]. Fermi satellite found evidence of hadronic interactions in SNRs, proving that they contribute to the galactic flux of cosmic rays [12]. For what concerns extra-galactic sources of cosmic rays, Auger measurement suggests a correlation between UHECRs arrival direction with nearby Active Galactic Nuclei (AGNs) [13]. However, no conclusive results were achieved up to now.

There are two models that describe cosmic rays acceleration in supernovae. The *first-order Fermi acceleration mechanism* takes place when primary cosmic rays encounter moving magnetic shock fronts that can be approximated by a plane wave. Assuming that the primaries have initial energy E_0 and that the shock front moves at velocity β, charged particles are scattered by turbulent magnetic fields and are able to exit the shock fronts with a higher energy $E > E_0$. The expected energy spectrum for this acceleration mechanism follows a power-law with spectral index $\gamma = -2$. However, the interactions that take place during the journey of the particle through Earth soften (i.e. increase the modulus) the spectral index. The *second-order Fermi acceleration mechanism*, instead, assumes that the interaction of primary particles takes place at the boundaries of moving, magnetised interstellar clouds, for which the plane wave approximation of the shock front doesn't hold. As a consequence, particles undergo random scattering, providing a lower energy gain.

The maximum achievable energy in astrophysical sources can be approximated as follows:

$$E_{MAX} \approx ZeBuL \tag{2.5}$$

Where Ze is the charge of the particle, B is the magnetic field, u is the velocity of the shock

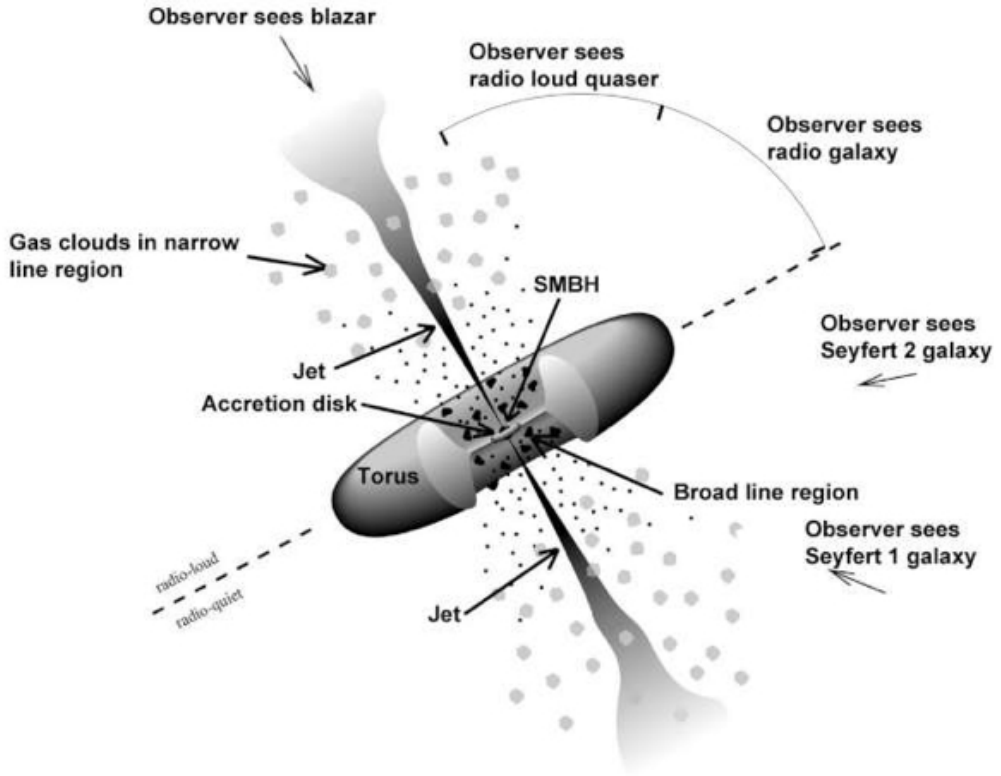

Figure 2.5: Unified model of Active Galactic Nuclei (AGN). According to the direction of the opaque torus and the jets towards the observer's line of sight, these objects present different features and can be studied using different approaches. (Image credit: `https://fermi.gsfc.nasa.gov/science/eteu/agn/`)

front and L is the size of the accelerating magnetic field.

A useful tool to understand which kind of sources could be capable of accelerating particles up to a certain energy is the *Hillas diagram*, shown in Figure 2.4. The Hillas diagram is constructed in this way: the horizontal axis shows the size (L) of the candidate sources of UHECRs, and in the vertical axes the magnetic field (B) is shown. The possible sources are positioned in the (L,B) plane and diagonal lines show the boundaries on the maximum attainable energy according to (2.5). As we can see, the only known objects that are capable of accelerating protons up to an energy of 10^{20} eV are Active Galactic Nuclei and Radio Galaxies.

From a multi-messenger point of view, we are interested in studying sources that are able to emit more than one type of particle. For this purpose, Active Galactic Nuclei (AGNs) are particularly interesting objects. A schematic representation of AGNs is shown in Figure 2.5. AGNs host a super massive black hole, i.e. having $M_{BH} \approx 10^6 \sim 10^{10} M_\odot$, in their centre, around which matter is accreted. Matter falling into the black hole conserves its angular momentum forming a rotating accretion disk. Accreted matter rotating around the black hole emits radiation in a wide range of frequencies, from radio up to gamma-ray energies. In about 10% of AGNs, infalling matter creates two collimated jets of relativistic radiation that shoot out in opposite directions, usually perpendicular to the disk [15]. Additionally, the accretion disk is surrounded by a dust torus, which is opaque, i.e. it absorbs part of the radiation emitted by the accretion disk.

Active galactic nuclei are classified into different categories according to the orientation of the torus and the jets with respect to our line of sight. If the jet points toward our direction

we see only the boosted radiation accelerated in the jets and we call these objects *blazars*. As the angle of sight with respect to the jet increases, the compact object inside the torus will be visible, in this case, we are dealing with a *quasar*. Finally, if our line of sight points directly to the torus the black hole is hidden, but we see the jets and we directly observe the radiation emitted by the torus. In this case, we call these objects *radio galaxies*. This classification is known as *unified model of AGN* [15]. We point out the three major classes of AGNs according to this model, a more detailed representation of all the possible classifications of these objects is depicted in Figure 2.5.

Besides being candidate sites of acceleration of cosmic rays, charged particles accelerated in jets are also likely to interact producing other particles, including neutrinos and gamma-rays. This is why these objects are widely studied in multi-messenger astrophysics.

2.2 Neutrinos

Neutrinos are fundamental particles of Nature, they are neutral leptons having spin 1/2 and they come in three flavours: electron neutrinos ν_e, muon neutrinos ν_μ and tau neutrinos ν_τ. The Standard Model of particles predicts the neutrino mass to be equal to zero. However, the discovery of flavour oscillations proved that neutrinos have a mass [16], and opened a window towards unveiling new aspects of the *Beyond Standard Model* physics. Additionally, neutrinos are very weakly interacting particles, they only interact through the weak force, making them extremely difficult to detect. On the other hand, these particles, being neutral and not interacting electromagnetically, are able to travel enormous distances without losing information about their energy and original direction.

In Figure 2.6 we show the neutrino energy spectrum. Likewise cosmic rays, it follows an unbroken power-law (2.1), and it covers several decades in energy. At extremely low energies, $O(\mu\text{eV} \sim \text{meV})$, we find the Cosmological neutrinos, i.e. neutrinos that decoupled from the thermal bath in the early universe producing the so-called Cosmological neutrino background, which are still to be detected. In the energy range between keV and GeV energies there are different species of neutrinos: solar neutrinos, reactor neutrinos, supernovae neutrinos and terrestrial neutrinos, that are widely studied in various underground experiment like, for example, Super-Kamiokande [17], T2K [18] and JUNO [19] experiments. At increasing energies the flux drastically decreases making the detection of these neutrinos more and more difficult. The GeV energy range is dominated by atmospheric neutrinos produced in hadronic air showers according to (2.4). Atmospheric neutrinos reach energies up to $O(10)$ TeV, where also an other type of neutrino start to arise: astrophysical neutrinos, which are the ones this work is about. The discovery of those neutrinos dates back to 2013, when the IceCube neutrino observatory declared the observation of 28 neutrino events of astrophysical origin having energies between 30 and 1200 TeV [2]. In Figure 2.6 astrophysical neutrinos are denoted as ν *from AGN*, but these are only one of the candidate sources of astrophysical neutrinos. Finally, in the PeV and EeV energy range, cosmogenic neutrinos appear. These neutrinos are the neutrinos produced by the GZK cutoff mechanism introduced in the previous section according to the reaction (2.2). Their existence would prove that the GZK cutoff is actually working, but the current instruments aren't capable of detecting neutrinos at these energies.

As we already mentioned, astrophysical neutrinos are likely to be produced from the interaction of cosmic rays in a dense target, but their small cross section makes them extremely difficult to detect, needing for new detection techniques to be developed. The operation principle for the detection of astrophysical neutrinos is the following: high-energy neutri-

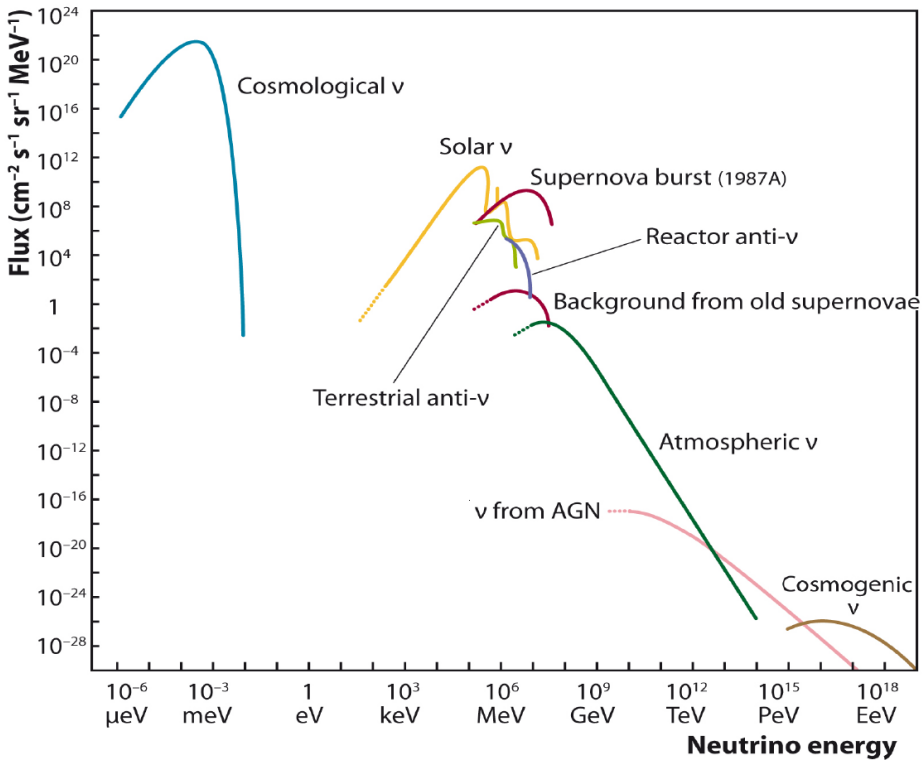

Figure 2.6: Neutrino energy spectrum. The fluxes of all the known neutrino types are displayed as a function of the energy. Image taken from [20].

nos, after the interaction with a dense medium, yield charged particles that move faster than the phase velocity of light in the medium, leading to the production of Čerenkov light, that is detected by optical sensors. Due to the steeping falling fluxes and low interaction probabilities, very large instruments are needed. Large volumes of dense medium available in nature are found in glaciers and at the bottom of the sea. In fact, water and Ice have good scattering and absorption properties, making these environments feasible for performing a precise reconstruction of charged particles travelling through the instrumented medium.

This principle of operation has been exploited in different experiments in the past decades. DUMAND [21] experiment consisted of a string of seven optical detectors deployed in the Pacific Ocean at a depth between 2000 and 4000 m with the purpose of detecting the Čerenkov light produced by atmospheric muons. The Baikal [22] experiment studied the properties of deep underwater Čerenkov light using three instrumented strings of 12 optical sensors each, deployed at the depth of the Baikal lake (Russia) and gave proof that the concept of neutrino telescopes actually works thanks of its detection of high-energy atmospheric neutrinos [23]. ANTARES [24] was a neutrino telescope located in the Mediterranean sea, that has been working from 2008 up to 2022 with the purpose of collecting Čerenkov light from atmospheric muons. The first attempt of neutrino astronomy was performed by the AMANDA [25] experiment, located at the Amundsen-Scott station at the South Pole, consisting of an array of 677 optical sensors mounted on 19 different strings deployed in the antarctic glacier. In 2005, AMANDA was dismissed and the construction of its successor project, IceCube neutrino observatory [26], began. IceCube is the largest working neutrino telescope ever built, and it instruments a volume of 1 km^3 of ice. The architecture of the experiment is described in detail in Chapter 3.

IceCube is a pioneering experiment, whose construction is motivated by a number of reasons. First of all, as we can see in Figure 2.7, the high-energy Universe is opaque to photons

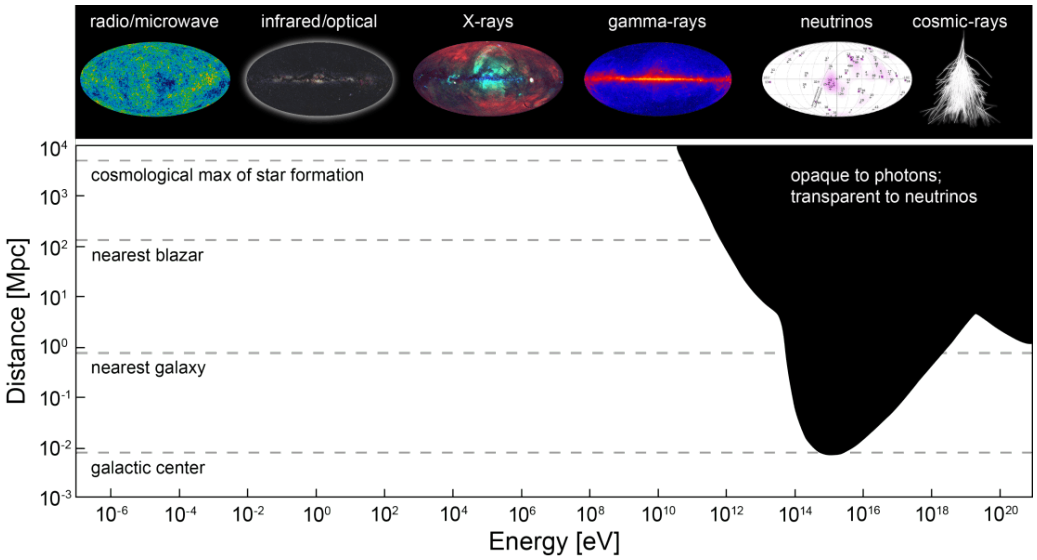

Figure 2.7: Energy and wavelength spectra as a function versus distance of the visible Universe. The black area represents the region of the Universe that is opaque to photons. In those regions, neutrinos and cosmic rays become the privileged messengers to study the most abrupt phenomena in the Universe. (Image credit: `https://icecube.wisc.edu/science/research/`)

but not to neutrinos, indicating that they are feasible for exploring the most abrupt phenomena in the Universe. Additionally, the discovery of sources of astrophysical neutrinos could allow to shed light on the long-standing puzzle about the origin of Cosmic Rays and the mechanisms through which they are produced. Astrophysical neutrinos are a smoking gun signature of cosmic rays interactions. Assuming the primary cosmic rays are protons, there are two main channels of production of cosmic rays: photo-hadronic interaction, and hadro-nuclear interactions. The first one consists in the interaction of a proton with a photon giving rise to these products:

$$p + \gamma \rightarrow \Delta^{+} \rightarrow \begin{cases} p + \pi^{0} \\ n + \pi^{+} \end{cases} \tag{2.6}$$

The hadro-nuclear channel, instead, consists in the interaction of a proton with a nucleus, which gives rise to:

$$p + N \rightarrow \pi^{\pm} + K^{\pm}, + ... \tag{2.7}$$

Both of these reactions lead to the production of neutrinos, but there is still no evidence of which of the two channels is the preferred one, if there is one. A relevant result in this context is the detection of a particle shower compatible with a Glashow resonance declared by IceCube in 2021 [27]. A Glashow resonance process consists in the resonant formation of a W^{-} boson after the scattering of an electron with an electron antineutrino:

$$e^{-} + \bar{\nu}_{e} \rightarrow W^{-} \tag{2.8}$$

IceCube detected a particle shower induced by a W boson hadronic decay compatible with a Glashow resonance process at 2.3σ level. The detection of this event, besides providing evidence of a Standard Model process that had never been observed before, suggests the presence of electron antineutrinos in the astrophysical flux and provides a feature to distinguish neutrinos from antineutrinos. Since the expected rate of neutrinos and antineutrinos is different for the two aforementioned processes, the detection of anti-neutrinos could provide a tool to understand if astrophysical acceleration sites produce neutrinos via hadro-nuclear or photo-hadronic interactions.

The choice of 1 km^3 detector is also motivated by the so-called *Waxman-Bachall* bound [28]. This bound states that the minimum needed volume to manage to detect astrophysical neutrinos is $\approx$ 1km^3. It is obtained according to the UHECR observations and it consists in an upper limit on the neutrinos flux produced in hadronic interactions, in particular, on neutrino production by either AGN or Gamma-Ray Bursts (GRBs).

In 2013, two years after its completion, IceCube proved that a $\sim$ km^3 size detector of instrumented ice is capable of detecting astrophysical neutrinos [2] and also announced the discovery of an astrophysical diffuse flux of neutrinos [29]. In 2018, the multi-messenger observation of a high energy neutrino event with the flaring blazar TXS 0506+056 [5] allowed to classify blazars as candidate sources of astrophysical neutrinos, giving proof of the consistency of the Waxman-Bachall bound. Additionally, time-integrated searches of neutrino signal excesses allowed to classify the Seyfert Galaxy NGC 1068 as an other candidate source of neutrinos [3]. On the other hand, similar searches for neutrino events from GRBs, the other astrophysical sources for which the Waxman-Bachall bound is expected to hold, didn't lead to any evidence [30].

Nevertheless, after 11 years of almost continuous of observation, both time-integrated and time-dependent approaches are expected to provide enough significance to produce a discovery. In particular, for what concerns time-dependent searches, the atmospheric background is highly reduced on short timescales and the evidence of correlation between signals related to different messengers coming from the same source also contributes to increasing the significance of the observations. For this reason, a real-time infrastructure based on a fast online analysis, described in detail in Chapter 4, was developed starting in 2005 with AMANDA and later on with IceCube. This analysis aims at favouring multi-messenger observations of the electromagnetic counterpart of clusters of neutrino flares through the transmission of alerts to the astronomical community. This work focuses on the test of the performances of the algorithm for the real-time analysis that produces the neutrino alerts (Chapter 5) and on the development of new approaches to increase their signal-to-noise ratio (Chapter 6).

2.3 Photons

Photons are massless particles, they are the carriers of electromagnetic force and the first messenger ever detected. They are electrically neutral, therefore their arrival direction points directly to the source they come from. Their cross section is much higher than the neutrino cross section, making impossible to study the Universe through high-energy photons. In fact, in Figure 2.7, we can see that approximately one-fifth of the sky cannot be studied using photon-based experiments at high energy. This is due to the fact that photons are very likely to interact with the Extragalactic Background Light (EBL), which is the radiation produced in stellar formation processes throughout the whole cosmic history. This radiation covers a wide range of wavelengths, from the near-infrared up to the ultraviolet region [15]. The interaction of high-energy photons with EBL photons produces an electron-positron pair, and this process drastically reduces the high-energy gamma-rays flux limiting the observations of distant gamma-ray sources.

Different techniques are used for detecting photons depending on the energy range of the observations. In the multi-messenger context, we are particularly interested in the ones used for detecting photons in the high-energy range. The first distinction consists in satellite and ground-based experiments. In the 50 MeV$\sim$300 GeV energy range, photons would be absorbed by the atmosphere, so, satellite experiments are needed. The NASA Fermi-LAT

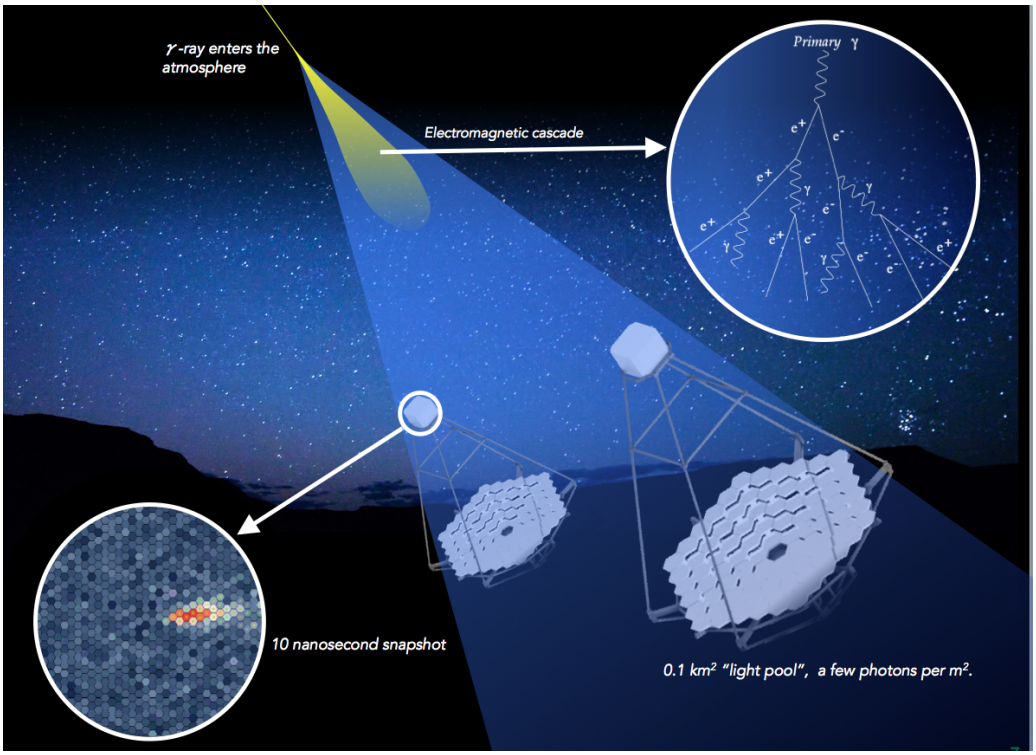

Figure 2.8: Sketch of IACTs detection technique. A gamma-ray enters the atmosphere and interacts producing an electromagnetic shower. The charged particles (e^+ and e^-) produced in the shower emit Čerenkov radiation, which is collected by the telescopes and used to reconstruct the direction of the primary photon. (Image credit: `https://www.cta-observatory.org/astri-detects-crab-at-tev-energies/`)

mission [7] has been monitoring the whole sky since 2008 collecting an enormous amount of information about gamma-ray sources in the GeV energy range. At higher energies, the gamma-ray flux is suppressed due to the interaction with the EBL, large effective areas are needed. Imaging Air Čerenkov Telescopes (IACTs) are ground-based experiments that detect Čerenkov radiation by electron and positrons produced in the photo-induced electromagnetic showers to estimate the energy of the primary photon that interacted in the atmosphere, as it is shown in Figure 2.8. These telescopes are sensitive in the so-called Very-High Energy regime, characterised by $E_\gamma > 50$ GeV. Some examples of IACTs are the MAGIC telescope in the Canary islands [31, 32], VERITAS in Arizona [33] and H.E.S.S. in Namibia [34]. The TeV energy range, instead, is still poorly explored, but future experiments as Čerenkov Telescope Array (CTA) will substantially increase the sensitivity at those energies [35].

While satellite experiments such as Fermi-LAT are able to monitor the whole sky, ground-based experiments can observe only a small portion of the sky and they can operate efficiently only on dark and clear nights. For this reason, multi-messenger observations can be favoured through the transmission of alerts that suggest follow-up observations of interesting events. This is what happened in September 2017, when, after an IceCube neutrino alert, MAGIC telescope observed the flaring blazar TXS 0506+056 [5]. This approach favours particularly the observation of fast and variable events, that need to be observed in real-time. Not only blazars present a large variability in their radiation emission, other phenomena that could be feasible for this kind of approach are Gamma Ray Bursts (GRBs), which are one of the most abrupt phenomena in the Universe. They are connected to supernovae [36] or neutron star mergers [8] and they are capable of releasing up to 10^{54} erg in gamma-rays on time scales that last from seconds to minutes.

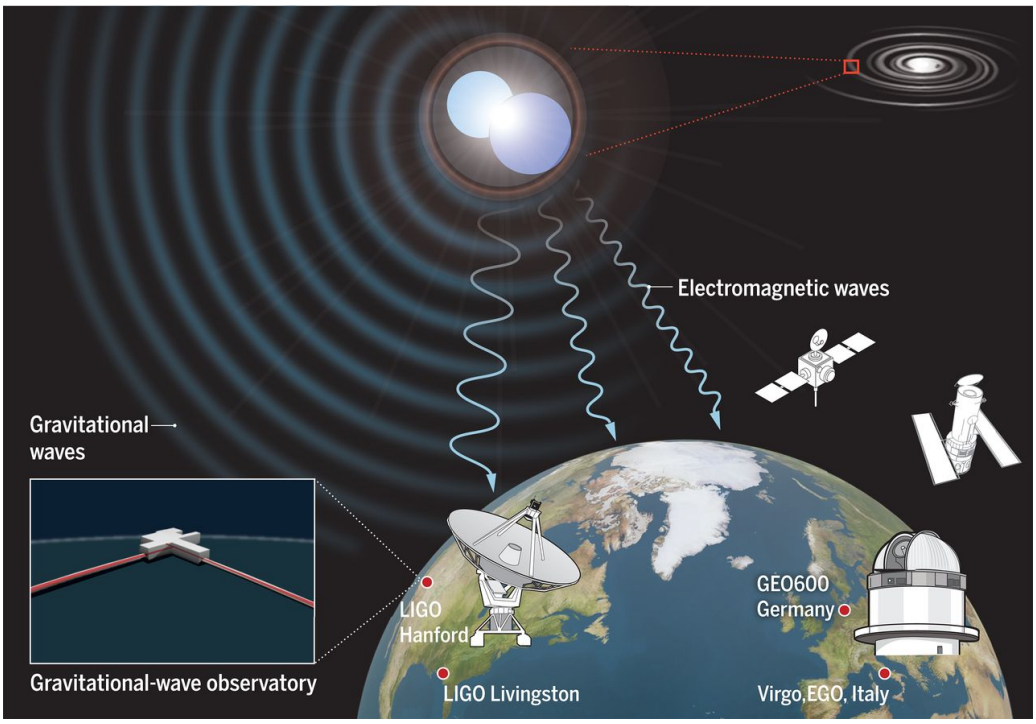

Figure 2.9: Example of multi-messenger observation of a gravitational wave event and a gamma-ray burst. (Image taken from [39])

2.4 Gravitational Waves

Gravitational waves are ripples in space-time that propagate at the speed of light. Their existence was postulated by Einstein in 1916 as a prediction of the general theory of relativity [37]. Every asymmetric motion of masses can produce gravitational waves. Nowadays we are only capable of detecting the ones produced by huge masses in acceleration.

The detection of the first transient gravitational wave signal, produced from a binary black hole merger, was announced by LIGO and VIRGO collaborations in 2016 [38].

Gravitational waves are emitted during the rotation of two astrophysical objects one around the other, which is shown in Figure 2.9. The waves propagate through space-time, and they are detected on Earth by orthogonal interferometers, that are capable of measuring the stretch of the arms caused by the gravitational waves.

Together with the emission of gravitational waves, during the merging of binary systems also other messengers, like neutrinos and photons, are likely to be produced. The observation of the gravitational wave event GW20170817 in coincidence with a Gamma-Ray Burst is the first multi-messenger observation involving gravitational waves ever performed [8]. For what concerns neutrinos, up to now no evidence of a correlation between gravitational wave events and neutrinos was found [40].

However, while gravitational waves provide information about the deformation of space-time, neutrinos are expected to be produced from relativistic photons and the external radiation field emitted from the source. Thus, they are complementary messengers.

Since gravitational waves are transient phenomena, also gravitational wave observatories can alert the astrophysical community for follow-up observations from IACTs and searches for neutrino signal excesses in the direction of the incoming gravitational wave.

Chapter 3

The IceCube Detector

As mentioned in section 2.2, in order to observe high energy neutrinos, large-scale detectors are needed. The physical mechanism that allows to detect the signature of such high-energy particles is the Čerenkov light emission by charged particles produced after neutrino interaction travelling in a dense medium with a phase velocity greater than the light velocity in the medium. Čerenkov radiation is detected using optical sensors sparsely deployed in the medium. In order to allow a good reconstruction of the particles emitting Čerenkov radiation, large absorption and scattering lengths are required. The only environments that are able to satisfy both the need of large volumes at a reasonable cost and the presence of a clear medium can be found in the depth of the seas or lakes, e.g. ANTARES [24], Baikal [41] and the upcoming KM3Net [42] and P-One [43], and in ice, as IceCube [26] and its predecessor AMANDA [25].

The IceCube Neutrino Observatory is the world's biggest working instrument capable of observing neutrinos between the TeV and PeV energy range.

In this chapter we will motivate the choice of building such an experiment in the antarctic ice and the hardware of the IceCube experiment and hardware will be described. Additionally, we will illustrate the typical event signatures detected by IceCube and its potentialities for real-time studies.

3.1 Detector Design

3.1.1 Optical properties of the ice

IceCube is located at the geographic South Pole and embeds a total volume of approximately $1\,\mathrm{km}^3$ of ice.

The antarctic ice has been proven to be one of the most efficient environments for Čerenkov light detection. Measurements proved that it is even clearer than the ice produced in laboratories [45]. In fact, the pressure operated by the glacier above the detector removes the air bubbles reducing the scattering processes of the photons. Additionally, in seawater, which has an average absorption and scattering coefficients of approximately a factor two greater than antarctic ice ones [45], the radioactive isotope $^{40}\mathrm{K}$ represents an additional source of noise in the signal detected by the optical modules, which is not present in the antarctic ice.

Despite being one of the clearest available mediums, in the antarctic ice both absorption and scattering phenomena still take place. The scattering is caused mainly by dust particles

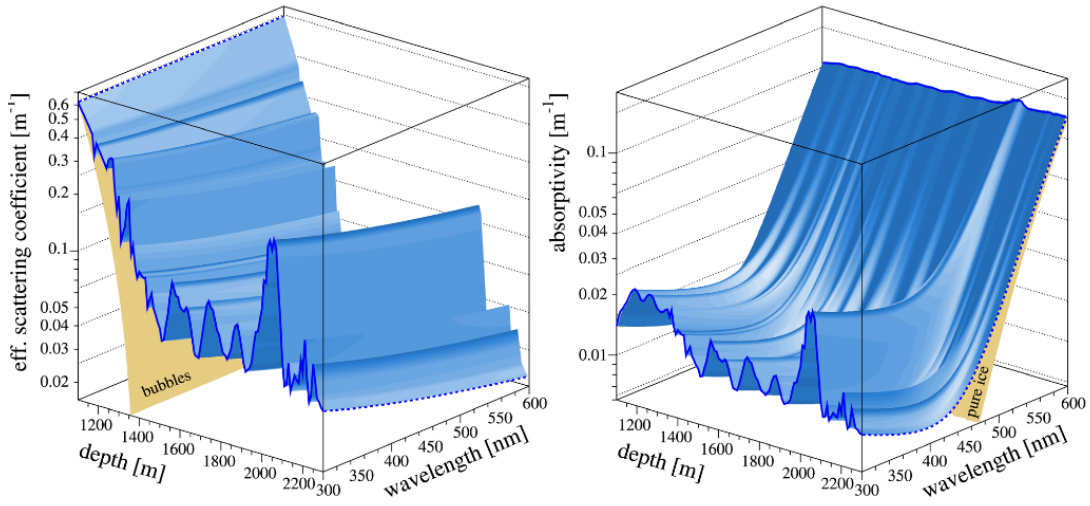

Figure 3.1: Scattering and absorption properties of the antarctic ice. The effective scattering coefficient (left) and the absorpitivity (right), i.e. the inverse of, respectively, the scattering and absorption mean free paths as a function of the wavelength and of the depth. Taken from [44].

such as sea salt crystals and mineral grains, while absorption takes place because of the presence of insoluble dust. In Figure 3.1 the effective scattering coefficient (left) and the absorptivity (right) are shown as a function of the wavelength and the depth. The yellow surfaces represent, respectively, the contribution to the scattering due to air bubbles and the pure ice absorption properties. The blue ones, instead, show the features of the South Pole ice accounting for all the impurities.

From a depth of about 1400 m, both the effective scattering coefficient and the absorptivity are minimal, except for some little variations. A big peak in both quantities is observed around a depth of 2000m. The presence of these peaks can be imputed to the presence of dust accumulated $\approx$ 65000 years ago [46].

The description of the ice properties has been refined several times over the years and new measurements allowed to implement a model describing the depth-layered structure of the ice, including the parametrization of the absorption and scattering lengths and ice anisotropy.

3.1.2 Construction and hardware

The IceCube detector is located at the geographic South Pole. Its construction began in 2004 and the detector has been working in its final configuration since 2011.

IceCube consists of 86 vertical strings deployed in the ice. Each string is almost 3 km long and connects the surface laboratory, IceCube Lab, with the bottom of the detector. Each string hosts 60 Digital Optical Modules (DOMs), for a total of 5160 modules, positioned between 1450 m and 2450 m of depth, and a cable that connects the DOMs to the IceCube Lab.

In Figure 3.2 a schematic sketch of the detector is shown. IceCube embeds a total volume of approximately 1 km^3 of ice. The primary detector is made of 78 strings, arranged in a hexagonal grid. The spacing between two strings is 125 m and the DOMs are deployed at a distance of 17 m one from each other. The minimum energy that is possible to detect with this configuration is of the order of 100 GeV. The large-scale detector is mainly dedicated to neutrino astronomy and astrophysics.

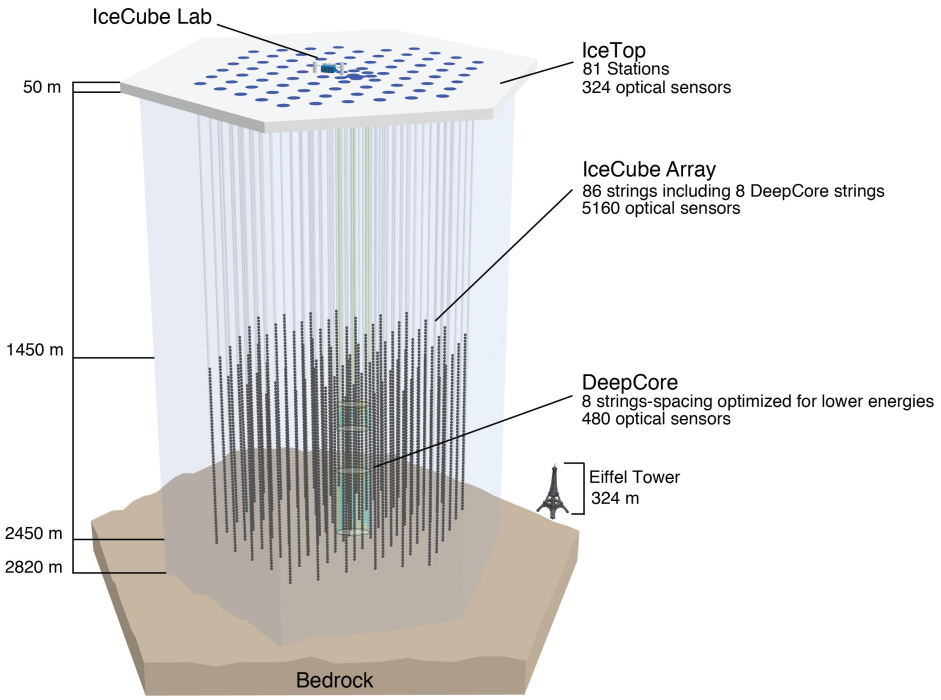

Figure 3.2: Schematic picture of the IceCube Detector. (Image taken from [26].)

In addition to the primary detector, 8 strings have been deployed with a lower distance among themselves, 72 m compared to the 125 m of the primary detector, and the DOMs are placed at a distance that goes from 7 m to 10 m apart. This set of strings is called *Deep Core*, and it is dedicated to the detection of lower energy neutrinos with a minimum detectable energy of approximately 10 GeV. The Deep Core strings are dedicated to the study of atmospheric neutrino oscillations and sterile neutrino searches.

On the surface, an array of 81 stations called *IceTop* is located. Each station is composed of two tanks filled with ice, each containing two DOMs. IceTop is used as a veto and it is sensitive to cosmic rays induced muon showers in the energy range between PeV and EeV, which is the energy at which UHECRs start to emerge. However, IceTop, covering a surface of only $\approx$ 1km^2, isn't capable of studying the UHECR spectrum because of the extremely low event rate at these energies. In fact, experiments such as Auger, occupy enormous areas (3000 km^2) to allow the detection of these events.

3.1.3 The Digital Optical Modules (DOMs)

Digital Optical Modules host the principal sensor components of the detector. As depicted in Figure 3.3, a DOM is a 13 ″ glass sphere split in half at the equator. The bottom part of the module hosts the 10 ″ photomultiplier tube (PMT). In the upper part, instead, the support electronics are placed.

The glass sphere protects the electronic and the PMT from the external pressure operated by the glacier. A 16 mm hole allows the cable to leave the module.

The PMT is sensitive to wavelengths between 300 nm and 650 nm, its quantum efficiency is of 25% at 390 nm. In the Deep Core, DOMs have a quantum efficiency of 34%. A wire mesh grid surrounding the PMT has the purpose of shielding it from magnetic fields, which would otherwise degrade the collection efficiency and the single photoelectron resolution.

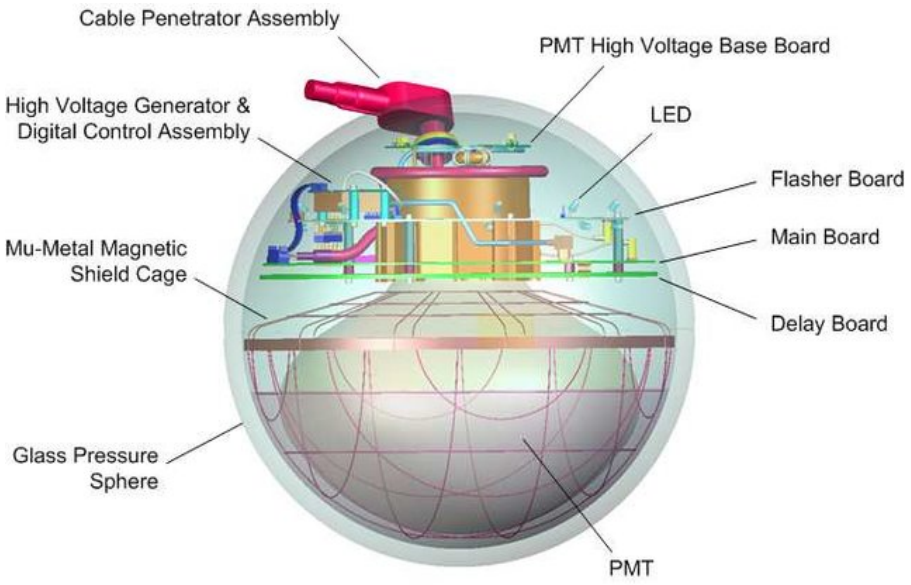

Figure 3.3: Schematic picture of a Digital Optical Module (DOM). (Image taken from [49].)

The PMT is connected to circuit boards which are responsible for power supply, data acquisition, communication and calibration. The maximum supply voltage for the PMTs is set to 2047 V.

The *Flasher board* is responsible for the calibration of the module. It contains 12 LEDs which can emit light at different wavelengths. The waveforms recorded by the PMT can vary widely, with amplitudes ranging from 1 mV to 2 V, and widths from 12 ns to 1500 ns, depending on the energy of the observed particle and the distance to the DOM. A discriminator starts recording the waveform once the voltage threshold, which is set to 0.25 photoelectrons, is recorded. The *delay board* allows to record the waveform starting from 75 ns before the trigger. In the case of the detection of a single photon, the waveform is available until 6.4 μs after the trigger. The PMT signal is captured and digitised by the Analog Transient Waveform Digitizers (ATWD) and a fast Analog to Digital Converter (fADC) [47]. The ATWD collects the first 427 ns of the waveform, the fADC, instead, continuously samples the waveforms, so it has a lower rate, but the same resolution.

The digitised waveform is proportional to the collected charge. The outputs of the ATWD and fADC modules are fitted using templates of pulsed produced in the laboratory or in previous studies [48]. The information transmitted daily by satellites to the IceCube computing centre in Madison (WI), is the output of the fit, which includes the time, the charge and the width of the pulses. In general, the full digitised waveform is not included.

3.2 Neutrino Interactions and Event Signatures in IceCube

IceCube is able to detect neutrinos that undergo deep inelastic scattering with an atomic nucleus producing a charged lepton that, travelling through the effective volume of the detector, emits Čerekov light.

This means that the interaction doesn't need to happen inside the detector. This will be the case of muons produced after a charged current interaction with a nucleus. This interaction is described by:

$$\nu_l + X \xrightarrow{W} l + X' \tag{3.1}$$

where l indicates one of the three lepton families (e, μ, τ) and X and X' are the mother and daughter nuclei.

Neutrinos can also interact through neutral current interactions. In this case, the process can be summarised as:

$$\nu_l + X \xrightarrow{Z} \nu_l + X' \tag{3.2}$$

These two processes can happen also for anti-neutrinos ($\bar{\nu}$). The only difference is the charge of the lepton produced in charged current processes. Except for very rare cases, e.g. Glashow resonance events, mentioned in Section 2.2, IceCube is unable to distinguish between neutrinos and anti-neutrinos. For the scope of this work, there is no difference in considering the particle or the anti-particle. So, from now on, when we will mention *neutrinos* we will mean both neutrinos and anti-neutrinos.

These interactions produce different kind of signatures inside IceCube detector. The most common signatures are shown in Figure 3.4. First of all, we need to distinguish between particles that produce electromagnetic or hadronic showers and linear tracks.

Linear tracks are produced by particles crossing the detector volume without decaying or interacting. The only particles that are capable of producing such a signature are muons. In Figure 3.4(a) we can see an example of a linear track. The displayed event corresponds to an up-going track, i.e. a muon crossing the detector volume from below. A down-going track, instead, is a linear track that crosses the detector in opposite direction, i.e. coming from above.

Linear tracks can be divided into two sub-categories, *through-going tracks*, which correspond to muons produced outside the detector volume that cross IceCube effective volume, and the so-called *starting tracks*, which are the signature left by muons produced inside the detector. Depending on the kind of interaction, starting tracks could be coupled with a shower produced by the other products of the charged-current interaction (3.1). Linear tracks usually have a good directional reconstruction, with an angular uncertainty of approximately 0.3° for 1 TeV energies. In contrast, the energy reconstruction is more difficult, because the particles are produced outside the detector and they may have lost energy before crossing IceCube volume. Further details about the energy and directional reconstruction of linear tracks will be given in Section 4.1.

The other characteristic signature that can be observed in IceCube are *cascades*. While linear tracks can be produced only by muons, cascades can be related to a great multiplicity of events. Neutral current interaction (3.2) leave this kind of signature, representing the decaying of the daughter nucleus after the interaction, but cascades can also be related to decaying particles and to a number of other scattering interaction that can take place in ice, not necessarily involving neutrinos. So, this kind of signature is strongly affected by the background. Both electromagnetic and hadronic showers usually develop for several meters, but, with respect to the string spacing, they appear to be point-like, so they leave a spherical signature, as shown in Figure 3.4(b). Since these kind of interaction are usually almost completely contained inside IceCube volume, the energy reconstruction of these events has an uncertainty of the order of $\approx 10\%$. In contrast with linear tracks, the directional reconstruction of these tracks is more difficult and it is of the order of 10° for a 100 TeV energy [51].

The other two signatures displayed in Figure 3.4 represent other kinds of event topologies that is possible to observe in IceCube. The bottom-left one represents the signature of muons produced by an air shower produced by the interaction of a cosmic ray in the atmosphere., i.e. a high-energy proton interacting in the Ice producing a hadronic cascade. The proton, after the interaction, produces unstable mesons that decay into muons, which penetrate the

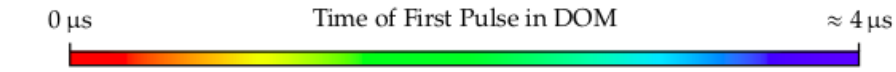

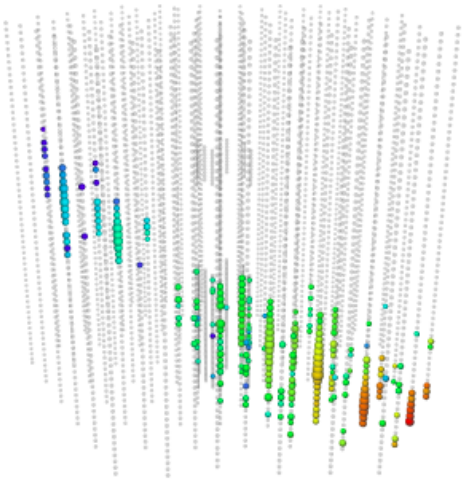

(a) Up-going track of a 75 TeV muon.

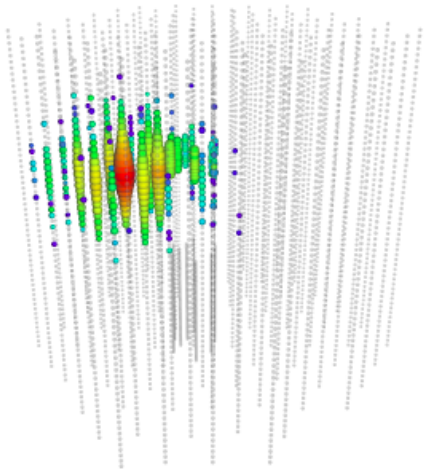

(b) A very energetic particle shower.

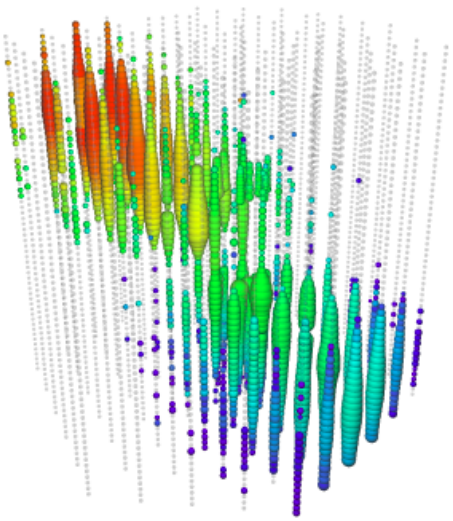

(c) Muons from an air shower, induced by a 100 EeV cosmic-ray proton.

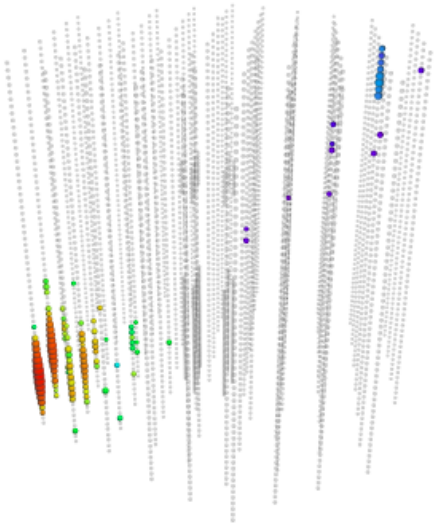

(d) Two coincident atmospheric muons.

Figure 3.4: Examples of event signatures in IceCube. In the upper left figure a through-going track is shown, in the upper right a cascade event is displayed. In the bottom part on the left there is a so-called muon bundle and on the right a signature left by two atmospheric muons is shown. The colour code indicates the temporal evolution of the events. (Image taken from [50].)

ice and cross the entire volume of the detector without interacting. So, the event displayed in Figure 3.4(c) is a convolution of several muons travelling in the same direction. These kinds of events are called *muon bundles*.

Figure 3.4(d), instead, shows the signature of two separated atmospheric muons that entered IceCube volume in coincidence. In fact, when particles leave a signature in a time interval of less than a few nanoseconds, the recorded pulses are considered correlated, and thus produced from the same process. This kind of event could be misidentified as a through-going track, but it is eventually recognised as an atmospheric event during the event processing,

that will be described in detail in the next chapter.

All of the three through-going events displayed in Figure 3.4 present a lower pulse density in the central region of the detector with respect to the upper and lower parts. This is due to the presence of the dust layer that we mentioned in the previous section, that substantially decreases the scattering and absorption lengths of Čerenkov photons in ice, reducing the number of detected photons.

3.3 Real-time Astronomy at IceCube

IceCube has the great capability of observing almost continuously the full sky: over an ordinary week, IceCube has an uptime above 99.8%. In fact, except for software upgrades, power outages or DOM calibration, IceCube is continuously collecting data [4]. In case of DOMs failure or malfunctioning of strings, the involved DOMs are excluded while the others continue the data taking.

This characteristic makes IceCube suitable for real-time studies. In fact, IceCube notifies the astrophysical community with public and private alerts whenever an interesting event is detected. There are several real-time analyses currently running. They concern primarily the detection of high-energy neutrinos with a high probability of having astrophysical origin and the detection of neutrino flares.

Spreading these alerts to the astrophysical community has the purpose of favouring multi-messenger observations of highly significant events.

The alerts related to the detection of high energy neutrino-induced muon tracks that have a high probability of being of astrophysical origin are released publicly on Astrophysical Multi-messenger Observatory Network (AMON) as Gamma-ray Coordinate Network (GCN) notices [4]. They contain information about the energy, the direction, the angular uncertainty and the probability of the event of being of astrophysical origin and they can be viewed in [52]. The most relevant result associated to this kind of alerts is the coincident detection of the high energy neutrino 170922A event and the observation of the flaring blazar TXS0506+056 [5]. This is one of the most relevant results of multi-messenger astrophysics and the proof of the potentialities of real-time multi-messenger studies.

The alerts related to the detection of significant neutrino flares, that are produced by the Gamma-ray Follow Up (GFU) alert system, instead, have a different treatment. The motivation behind the production of this kind of alerts has to do with the fact that known gamma-ray emitters are also believed to be candidate sources of high-energy neutrinos. Most of these sources are variable in their non-thermal radiation emission. This motivates the development of a time-dependent analysis that aims at identifying possible neutrino flares in real-time with the purpose of favouring multi-messenger observation of high energy neutrinos and gamma-rays. The development of this analysis started in 2005 with AMANDA and MAGIC collaborations [53] and it was implemented in IceCube starting from 2012 [4]. IceCube now collaborates with three IACTs: MAGIC [31, 32], VERITAS [33] and H.E.S.S. [34] for the GFU program. GFU alerts related to neutrino flares coming from known gamma-ray emitters monitored by Čerenkov telescopes are kept private and shared only with the partner telescopes, that are encouraged to perform follow-up observations. In more recent times, also an unbiased search of possible flares over the entire sky was implemented. The alerts related to this analysis are called *GFU all-sky alerts*. These alerts are shared publicly on GCN/AMON [4].

This work focuses on a follow-up analysis of GFU from known gamma-ray sources, the so-called source catalogue analysis. This analysis will be described in detail in Chapter 4 and in Chapter 5 its performances and the historical results will be discussed.

Chapter 4

Real-Time Alert System and Analysis

Before being able to perform data analysis, the enormous amount of data collected by the IceCube experiment needs to be filtered, cleaned and selected in order to obtain data samples suitable for analyses.

There are several kind of analyses performed within the IceCube Collaboration. The various steps of the event reconstruction procedure differ according to the purposes of the analysis, the kind of events that need to be selected, and if an online, yet fast, analysis is required.

The analysis treated in this work aims at identifying interesting neutrino flares in real-time. This means that the filtering and reconstruction of raw data need to be very fast in order to allow to notify relevant results to the astrophysical community with the shortest possible latency and favour follow-up observations of interesting events.

In this chapter, the architecture and the analysis of the IceCube real-time system that is used for this work will be described. First of all, we will outline the major steps of the event selection starting from the PMT pulses collected by the DOMs at the South Pole up to the so-called Gamma-ray Follow-Up (GFU) filter, which allows to define the GFU event sample, that is the one used for this work. Then we will introduce the likelihood analysis and, finally, particular attention will be given to the algorithm that is used to produce the GFU neutrino alerts: the *Time-Clustering algorithm*.

4.1 Event Selection and Reconstruction

Figure 4.1 shows a sketch of the major steps of the event selection procedure, starting from the pulses recorded by the DOMs up to the identification of a candidate neutrino-induced muon.

As we mentioned before, since we are dealing with a real-time analysis, we need to use fast algorithms, especially in the first steps of the analysis, which are performed directly at the South Pole, when the event rate is still very high.

4.1.1 Level1 (L1) Trigger

The first step of the event selection is the so-called **Level1 Trigger**. Its goal is to arrange the stream of pulses received by the DOMs in physics events. After observing a hit, the so-called Hard Local Coincidence (HLC) checks the neighbouring and next-to-neighbouring DOMs on the same string for coincident hist within $\pm 1\,\mu$s. For each HLC the full digitised

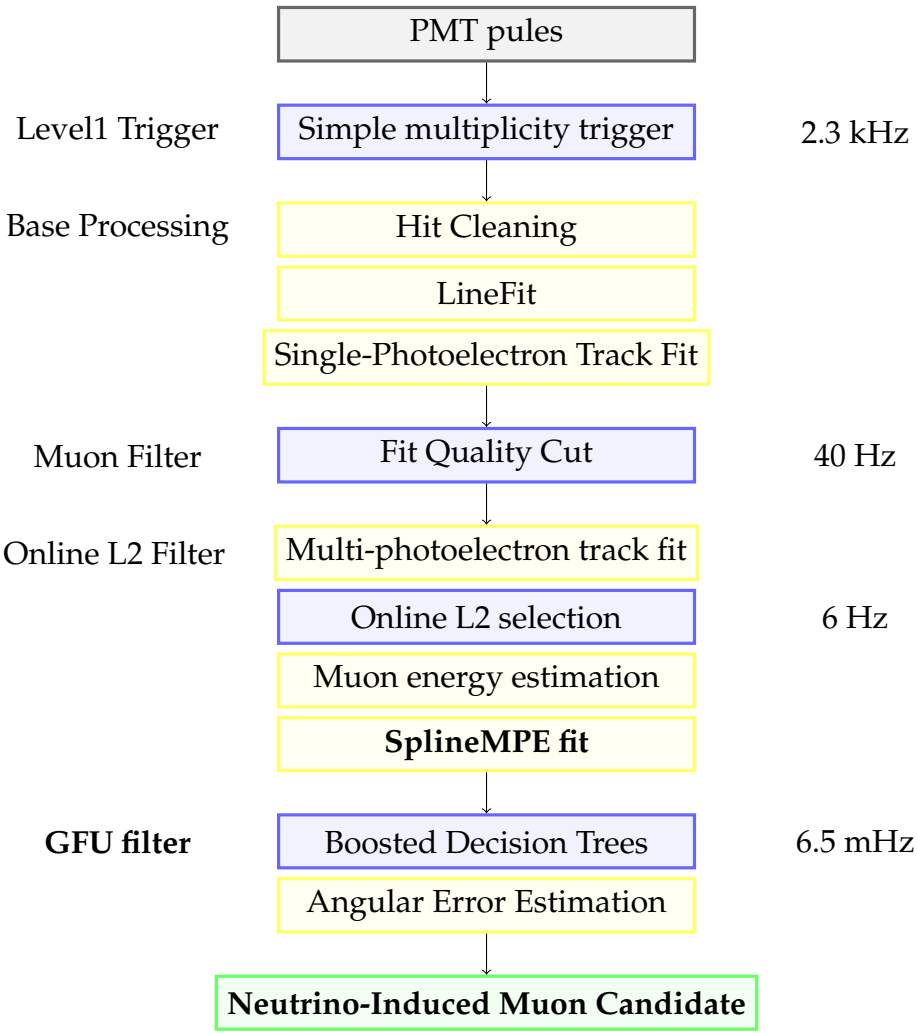

Figure 4.1: Sketch of the filtering and reconstruction procedure. The names of the modules are on the left. Each module can be composed of one or more steps. Yellow boxes represent the reconstruction steps, the blue ones represent the filters that allow to reduce the data rate. The approximate frequencies after the cuts are reported on the right. Adapted from [50].

waveform is stored. If the hit doesn't satisfy the HLC requirement, it is classified as a noise hit, and only the pulse amplitude is stored and transmitted to the computers on the surface.

This first step allows to reject noise hits. In fact, only the information stored in the HCL unit is used by the **Simple Multiplicity Trigger (SMT-8)**, which is a filter that discriminates the time window during which interesting pulses are collected. It requires the detection of a minimum of 8 HCL hits during a sliding time window of 5 μs. Realising the SMT-8 condition marks the start of the trigger time window, which ends once the sliding time window does not contain any more HLC hits. The trigger windows from this and other triggers are merged into a global trigger window. All the hits recorded during this global trigger window are sent to the event builder and written to disk, where it is picked up by the **Processing and Filtering (PnF)** system for the next steps [54].

At this point of the analysis, we are still dealing with DAQ events and the rate is still very high ($\approx$ 2.7 kHz, see Figure 4.1). Some DAQ events may correspond to multiple overlapping events that were merged inside the same time window. The **trigger splitting** procedure is able to separate the tracks of two muons arriving very close in time. At this stage, only temporally separated events are split. The spatially separated but temporally coincident events are kept unchanged because, at this stage, it is difficult to discriminate if those tracks

are independent or they represent a signature of some particular kind of event, like a muon traversing the dust layer which could be misidentified as two independent muons (see Figure 3.4 for a reference).

4.1.2 Base Processing

After the **Level1 Trigger**, there is the so-called **Base Processing** step, which aims at reconstructing the original direction of the neutrino candidates. The underlying hypothesis of this step is that we are working with neutrino-induced through-going muon tracks. Since we want to study point-like neutrino sources, the directional reconstruction is one of the most delicate steps of the whole reconstruction chain. It is particularly challenging because, at this stage, where we just passed the Level1 Trigger, the rate is still high and, at the same time, we need to use fast algorithms in order to perform an efficient real-time analysis.

Four different algorithms are used for the directional reconstruction, each providing a more precise reconstruction than the previous one. Those algorithms are: *LineFit*, *Single Photoelectron (SPE) Fit*, *Multi Photoelectron (MPE) Fit* and *Spline Multi Photoelectron (SplineMPE) Fit*.

The **LineFit** is a basic reconstruction method which is based on the hypothesis that a plane wave of light passes through the detector and produces the observed pulses in each DOM. The position $\vec{r}(t)$ of a through-going muon at the time t can be modelled as:

$$\vec{r}(t) = \vec{r_0}(t_0) + (t - t_0)\vec{v} \tag{4.1}$$

where $\vec{v}$ is the muon velocity and $\vec{r_0}$ corresponds to the point the muon crosses at t_0.

The algorithm minimises the squared distance between the track hypothesis and the position of the DOM that recorded the pulses:

$$\min_{v,\vec{r_0}} \sum_{i=1}^{N} ||\vec{r}(t_i) - \vec{x}_i|| \tag{4.2}$$

where N is the number of hit DOMs, $\vec{x}_i$ is the DOM position and $\vec{r}(t_i)$ the track hypothesis at time t_i.

Since the computation can be carried out without the need of a time-consuming minimizer, the output of this step represents a first guess of the direction, and it will be used as a seed for the following computations. Additionally, this fit provides an estimate of the velocity $|\vec{v}|$ which is used as a parameter in the final event selection. In fact, for well reconstructed tracks, we expect the velocity to be close to the speed of light and higher than the speed of light in ice, otherwise Čerenkov emission wouldn't be possible.

A first improvement to the LineFit method consists in modelling the light emission along the muon track as described in Figure 4.2. A muon travelling faster than the phase velocity of light in ice produces Čerenkov light cone. The associated wavefront is emitted with respect to the muon track under the so-called Čerenkov angle:

$$\cos(\theta_c) = \frac{1}{n\beta} \tag{4.3}$$

where β is the velocity of the muon ($\beta \approx 1$) and n is the refractive index of the ice ($n \approx 1.32$).

In Figure 4.2 we show the geometry of the muon track. A muon travels along the direction $\vec{v}$ passing through an arbitrary point $\vec{r_0}$ and it emits Čerenkov light at an angle θ_C. The

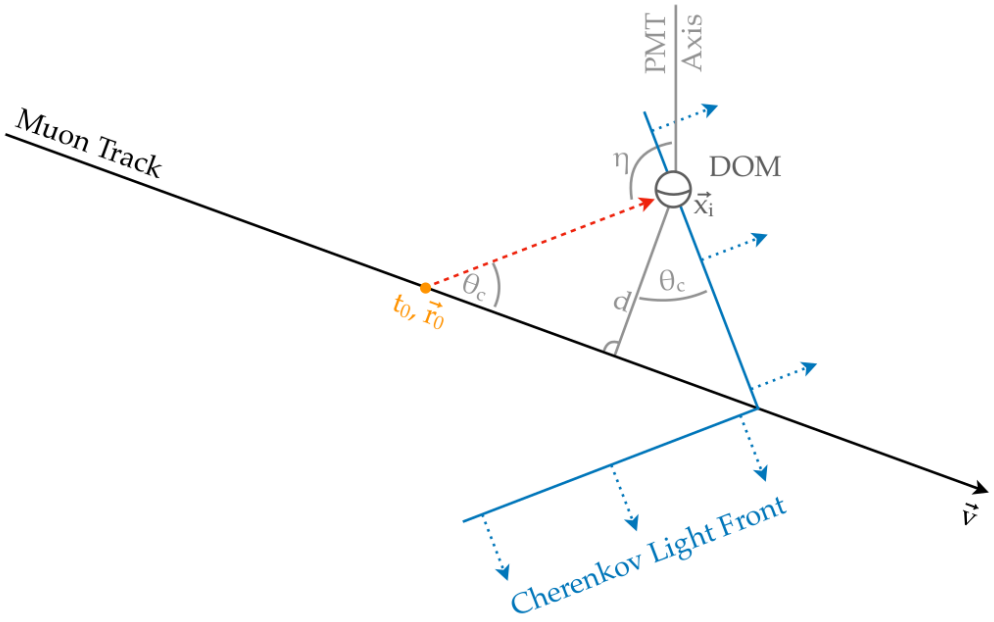

Figure 4.2: Sketch of the Čerenkov light emission of a muon travelling at relativistic speed through Ice. (Image taken from [50].)

Čerenkov light reaches the DOM, located in $\vec{x}_i$ at a distance d from the direction of the track. Under the assumption of the absence of scattering, the time at which a photon emitted in $\vec{r}_0$ reaches the DOM can be expressed as:

$$t_{geo} = t_0 + \frac{\vec{v}(\vec{r}_0 - \vec{x}_i) + d\tan\theta_C}{c_{vac}} \tag{4.4}$$

where c_{vac} is the speed of light in vacuum.

The **Single Photoelectron (SPE)** method consists in a likelihood test of the probability that the detected pulses are compatible with the hypothesis of a through-going muon track emitting Čerenkov light with the geometry shown in Figure 4.2. The quantity that is tested is the so-called time residual, i.e. the difference between the observed time and t_{geo}, defined in (4.4):

$$t_{res} = t_{obs} - t_{geo} \tag{4.5}$$

This algorithm considers only the first photon detected by each DOM for the computation of t_{res}. This choice is due to the fact that the first photons to reach the DOM are the ones that are less likely to have scattered, thus they better describe the geometry of the Čerenkov cone. This is why this method is called *Single* Photoelectron fit.

The probability density function used for the likelihood fit is the one modelled by the Baikal experiment for the emission of Čerenkov light in water [55] and adapted by AMANDA [56] for the emission in the ice. It is called *Pandel* function and it has the following analytical form:

$$p_1(t_{res}) = \frac{1}{N(d)} \cdot \frac{\tau^{-\frac{d}{\lambda}} t_{res}^{\frac{d}{\lambda}-1}}{\Gamma(\frac{d}{\lambda})} \cdot \exp\left[-t_{res}\left(\frac{1}{\tau} + \frac{c}{n\lambda_a}\right) - \frac{d}{\lambda_a}\right] \tag{4.6}$$

with

$$N(d) = \left(1 + \frac{c\tau}{n\lambda_a}\right)^{-\frac{d}{\lambda}} \cdot \exp\left[-\frac{d}{\lambda_a}\right] \tag{4.7}$$

where λ_a is the absorption length, and λ and τ are the fit parameters determined from Monte Carlo simulations, which represent, respectively, the expected scattering probability and expected time residual according to the model.

The likelihood fit performed by this reconstruction algorithm is defined as:

$$\mathcal{L} = \prod_{i=1}^{N_{ch}} p_1(t_{res,i}|\vec{r}_0, \theta, \phi) \tag{4.8}$$

where N_{Ch} is the number of hit DOMs.

The likelihood maximisation provides a refined estimate of the muon direction $(\vec{r}_0, \theta, \phi)$ and a quality factor that allows to judge the hypothesis that the fit parameters well describe the distribution of the detected pulses, thus the event is well reconstructed and it is likely to be a through-going muon track.

At this point of the processing, the information gained by the SPE fit is enough to select the track-like muon signatures, thus the SPE fit is the last step of the Base Processing module.

4.1.3 Muon Filter

The next module, as shown in Figure 4.1, is the **Muon Filter**.

The SPE fit provides a sample of candidate physics events. At this stage we need to reduce the event rate in order to be able to preform more accurate reconstructions. In order to do this, we need to select only the events that have a high probability of actually being muon tracks. After the Muon filter, the rate is reduced of almost two orders of magnitude: from 2.7 kHz up to 40 Hz.

For up-going muon tracks the likelihood fit quality factor is used to evaluate the probability of the track to be associated to a through-going muon. Down-going tracks are more difficult to handle because of the large atmospheric muons background.

Since the astrophysical neutrino flux is expected to be much harder than the atmospheric one, $\gamma_{astro} \approx -2$ while $\gamma_{atm} \approx -3.7$, the muon filters applies a cut on the minimum integrated charge, Q_{tot}, recorded by the DOMs for each event, which is proportional to the energy of the particle and provides an immediate handle of the kind of particle we are dealing with. In fact, the higher is the energy of the particle, the higher is the probability that it produces secondaries. The cuts also depend on the declination and follow this criterion [50]:

$$\begin{aligned} &\tfrac{\log \mathcal{L}}{N_{ch}-3} \leq 8.7 && \text{if} \quad -1.0 \leq \cos\theta \leq 0.2 \\ &\log Q_{tot} > 3.9 \cdot \cos\theta + 0.65 && \text{if} \quad 0.2 \leq \cos\theta \leq 0.5 \\ &\log Q_{tot} > 0.6 \cdot \cos\theta + 2.3 && \text{if} \quad 0.5 \leq \cos\theta \leq 1.0 \end{aligned} \tag{4.9}$$

where $\mathcal{L}$ is the SPE likelihood, N_{ch} is the number of hit DOMs and θ is the declination.

After the muon filter, the event rate is approximately 40 Hz, low enough for allowing daily satellite transmission to Madison for offline analysis and for more complex and time-consuming reconstructions for real-time studies at South Pole, that will be explained in the following. The reason why such a low rate is needed for data transmission is that the South Pole is poorly covered by satellites, resulting in a limited available bandwidth, thus it is important to reduce the amount of data as much as possible before sending them to the North.

Nevertheless, to handle possible bugs, the whole waveform sample of each event before the selection is stored on tapes and shipped to Madison (WI) once a year.

4.1.4 Online Level2 (L2) Filter

The next step of the reconstruction procedure is the **OnlineL2 Filter**. The name *online* is due to the fact that this step is often used for real-time studies, while *L2* stands for Level 2, because this filter is applied after the first level reconstruction described in the previous steps. The main goal of this filtering and reconstruction step is improving the directional estimate of the muons provided by the SPE fit using the Multi Photoelectron Fit first, and refining it using the Spline Multi Photoelectron Fits after the Online L2 selection (see Figure 4.1). In this module, the first estimate of the energy of the muon is also provided. This is a fundamental piece of information because it allows to provide an estimate of the energy spectrum of the sources and this is used to separate the signal and background events.

When muons have an energy of more than 1 TeV, it becomes increasingly likely to detect more than one photon per each DOM. Thus, we have to take into account this effect by modifying the SPE likelihood expression and adapting it for multiple photon detection in each DOM. This algorithm is called **Multi Photoelectron (MPE) Fit** and it consists in a likelihood maximisation similar to the one used for the SPE fit. The expression of the likelihood used by this algorithm is the following [56]:

$$\mathcal{L} = \prod_{i=1}^{N_{Ch}} \left[N_i \cdot p_1(t_{res,i}) \cdot \left(\int_0^{\infty} p_1(t_{res,1}) \right)^{N_i - 1} \right] \tag{4.10}$$

where t_{res} and p_1 are the ones defined in (4.5) and (4.6) respectively.

This likelihood formulation takes into account the probability of observing the first photon out of N_i photons in the i_{th} DOM at the instant $t_{res,i}$. This algorithm uses as seed the outcome of the SPE fit, it provides a better reconstruction of the direction of the muons and allows to identify down-going muons that were previously classified as up-going tracks.

After the MPE fit, the Online L2 selection is applied. This stage reduces the rate from 40 Hz to 6 Hz. Just as for the muon filter, this selection depends on the directional reconstruction of the tracks, on the total integrated charge and on the region of the Sky the tracks come from. Being based on the improved MPE fit, the cuts applied by this filter are tighter because signal and background are better separated. [57].

The fourth and most sophisticated algorithm for the directional reconstruction of the muons is the **Spline Multi Photoelectron (SplineMPE) Fit**. It uses the same likelihood of the MPE fit, but, instead of using the Pandel function (4.6) as PDF, it uses a simulation of the propagation of photons in ice. Instead of using a homogeneous ice model as in the previous steps, the SplineMPE method uses a model that takes into account the depth dependence of the absorption and scattering probability of photons in ice. The results of this simulation are available as interpolating splines[1] [58].

In the OnlineL2 module, the first estimate of the energy of the muon is provided. Since we deal with through-going tracks, the muon is generated outside the detector. So, the particles can travel very long distances, and thus lose energy, before being detected. So, the energy observed by IceCube is only a fraction of the total. However, it provides a lower bound on the energy of the neutrino.

The number of Čerenkov photons produced by the muons and the possible secondary charged particles produced after bremsstrahlung processes is proportional to the track length, which

[1]Spline stands for Segmented Polynomial Line and it is a function defined piecewise by polynomials in such a way that it is continuous up to a certain order derivative. Splines are widely exploited for their simple construction and their accuracy in the evaluation of complex fits.

is proportional to the energy of the particle. The number of detected photons follows a Poisson distribution, so the likelihood has this expression:

$$\mathcal{L} = \frac{\lambda^k}{k!} e^{-k} \tag{4.11}$$

with

$$\lambda = \Lambda E + \rho \tag{4.12}$$

where E is the energy, k is the number of observed photons and λ is the mean expected number of photons given the template Λ, which depends on the location of the emitting track, the location of the observing DOM, and on the relative position between the DOM and the track. ρ, instead, represents the noise contribution.

There are several methods for the estimation of the energy of a particle. They are all based on the underlying hypothesis that the number of detected photons follows a Poisson distribution (4.11), and the main difference consists on the treatment of the stochastic energy losses of Čerekov photons when defining the template Λ.

The estimation used in this work is the so-called **MuEX (Muon Energy Estimation)** and it considers the muon emitting Čerenkov light uniformly along its track. As a consequence, the expected number of photons depends on the distance between the track and the DOM. In modelling the template Λ, the scattering effects are neglected for short distances, resulting in a $1/r$ dependence in the photon density. At larger distances, the diffusive behaviour is approximated with an empirical expression reported in [48]. Under these hypotheses, the MuEX method simply consists in maximising the (4.11) likelihood providing an estimate of the energy E.

The energy estimate of the particle is the last step of the OnlineL2 Filter. At this point, we gained a refined reconstruction of the direction of the track and we are left only with the last step of the event reconstruction chain, the **Gamma-ray Follow-Up (GFU) Filter**.

As we will explain in the following section, the GFU filter is based on machine learning algorithm which aims at providing a sample of the events with the best possible purity. This means that the reconstruction procedure is concluded and that will not be further improved in the next step.

Summing up everything we discussed in the previous sections, in Figure 4.3 we show the median angular error of the four different reconstruction algorithms we described. In constructing these plots simulated events were exploited. The plots show the median difference between the *true* simulated direction and the one provided by the reconstruction algorithm, as a function of the true muon energy (left) and declination (right).

The error difference clearly diminishes with more sophisticated algorithms. The LineFit provides an error of the order of $\approx 1^\circ$, while the Spline has a median error of $\approx 0.1^\circ$. Looking at the SplineMPE performance, the error diminishes, as expected, with increasing energies and starts to increase at very high energies. This is due to the fact that the stochastic emissions, which start to be relevant at very high energies, is not considered in the energy reconstruction. In the Northern Sky, the error increases when approaching the pole because the effects due to Earth absorption arise and the geometry of the detector, with its different lateral and vertical DOM spacing, favours the horizontal tracks.

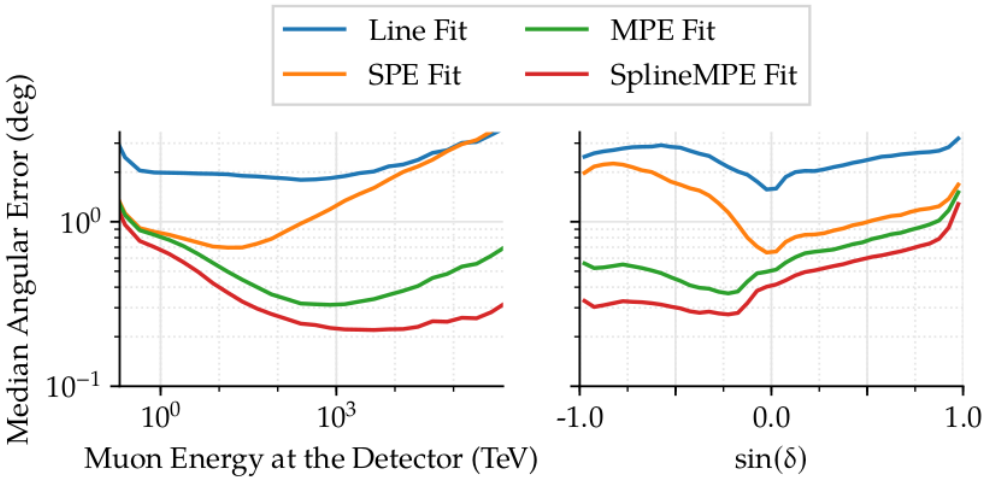

Figure 4.3: Median angular error on the directional reconstruction of through-going muon tracks for all the different algorithms. Left: as a function of the true muon energy, averaged over all the declination range. Right: as a function of the true declination, averaged over all the energy range. (Image taken from [50].)

4.1.5 Gamma-ray Follow-Up (GFU) Filter

The last module of the filtering and reconstruction procedure is the **Gamma-ray Follow-Up (GFU) Filter**. The cuts applied by this filter aim at constructing a sample of events with the best possible purity, i.e. with the highest probability of being neutrino-induced muon candidates. This is done using a machine learning classifier based on Boosted Decision Trees (BDTs). After the GFU filter the event rate is reduced from 6 Hz to 6.5 mHz, which corresponds to approximately 200 000 events per year. After the GFU filter, we obtain the data sample used in this work. The very last step of the event selection and reconstruction consists in the estimate of the angular uncertainty.

The main purpose of the **Boosted Decision Tree** is to select more strictly the interesting events, rejecting the background. The previous cuts (Muon Filter and OnlineL2 Filter) were performed on the basis of a single variable. Since we are dealing with sophisticated algorithms and we are working in a background-dominated scenario, using only one variable is not the most efficient choice. A decision tree is a set of binary decisions. It can be several levels deep, at each node an observable is evaluated and compared to a cut. The events are passed through different nodes over all the levels and, at the final level, they are assigned to the final leaf, which will be characterised by a certain probability of being a signal-like event. If an event ends up in a signal-dominated leaf it gets accepted, otherwise it gets rejected. During the training process, the best set of observables and the values of the cuts are chosen. Then, the *boosting* procedure is performed: the tree is applied to the training sample and the event weights, that are used to define the purity of the leaves, are adjusted depending on whether the event is classified correctly or not, assigning a higher weight on the misclassified events. This is done several times in order to have a set of Boosted Decision Trees. To avoid the over-fit problem, i.e. to avoid the algorithm to be stuck on specific patterns of the training set and lose track of the general structures, a subset of observables is randomly chosen for some nodes. Implementations of the algorithm can be found in the publicly available *scikit-learn* package [59], and in IceCube's internal *pyBDT* implementation.

Before applying the GFU filter the sample is still composed mostly of mis-reconstructed events from down-going particles produced in air showers. At this stage of the event pro-

cessing it is necessary to distinguish between the data coming from the Southern and the Northern Sky. In fact, the dominant kind of background is profoundly different in the two hemispheres, so two separate classifiers are developed using an individual set of variables in each hemisphere.

In the Northern Sky, the major source of background is composed of mis-reconstructed down-going muons or cascades wrongly selected in the previous steps. The Southern Sky, instead, is dominated by the atmospheric background.

Northern Sky

The variables used by the BDT in the Northern Sky, i.e. for up-going events, are:

- An up-going event is defined as an event that has a zenith $\theta > 82^\circ$
- The normalised value of the SplineMPe likelihood fit provides an immediate handle on the compatibility between the event properties and the hypothesis of a muon track
- The shape of the likelihood around the maximum provides information about the reconstruction quality. Thus, the second derivative of the SplineMPE likelihood, which gives information about the width of the maximum is used as a variable. The narrower is the peak, the better is the reconstruction.
- The velocity $|\vec{v}|$ of the particle should be close to the speed of light
- The directional reconstruction of the LineFit and the SplineMPE fit should not be dramatically different. A large difference in the directional reconstruction is a symptom of a mis-classified event
- A difficult class of events to classify are the coincident events. The event splitting procedure can disentangle these events only if they are less than 10 microseconds apart. If two particles interact in different parts of the detector in a time interval of less than $10\,\mu$s the directional reconstruction will try to merge the pulses from two unrelated particles in a common track. In order to spot these cases, the pulses are divided into two subsets and the directional reconstruction is performed independently for the two sets of pulses. If the event is associated to a through-going muon, the two reconstructions need to be compatible with each other and close to the original direction of the muon.
- A Bayesian Prior that provides information about the probability of a down-going track to be reconstructed as an up-going one is incorporated in the likelihood expression of the SplineMPE fit (4.10). This allows to gain rejection power against mis-reconstructed down-going muons
- Muons traversing a large part of the detector are usually well reconstructed. However, skimming tracks, i.e. tracks that pass close to the edge of the detector and are only partially contained in the active volume, can produce ambiguous light deposition and are much more likely to be mis-reconstructed. In order to evaluate the probability of these tracks to be through-going muons, we define the *centre of gravity* of the hits as:

$$\vec{CoG} = \frac{1}{Q_{tot}} \sum_{i=1}^{N_{Ch}} q_i \cdot \vec{x}_i \tag{4.13}$$

  where Q_{tot} is the total integrated charge, q_i is the integrated charge over every single DOM and $\vec{x}_i$ is the DOM position. This quantity provides a tool to reject the events whose centre of gravity is too close to the border of the detector.

- The number of *direct hits* is another variable that can be used to evaluate the quality of a track. In the previous section we defined the time residual (4.5) as the difference between the expected time a photon takes to reach a DOM and the recorded time. A hit is called direct if t_{res} is constrained within a certain time window that takes into account the finite timing resolution of the detector and the probability of the photon to be scattered along its path, which may cause delays in the detection of the photons. The number and the spatial distribution of direct hits per track is an estimator of the quality of the reconstruction.
- The direct length, i.e. the distance between the first and the last direct hits, needs to be large for through-going muons. Thus, this quantity is used in the trees for rejecting starting events.
- The distribution of hits along the track is also informative about the quality of the directional reconstruction of the track. We define the separation length L_{sep} as the distance between the centre of gravity (4.13) and the first quarter of hits. The longer is L_{sep}, the higher is the probability that the track is a through-going muon.
- The distribution of the hits is expected to be uniform along well-reconstructed tracks, thus a *smoothness* parameter, which measures the relative deviation of the direct hits from a uniform distribution is evaluated to judge the quality of the events.
- The light profile (i.e. the collected charge) around the track should be such that the DOMs that are located close to the centre of gravity collect more charge than further DOMs, which should collect a lower number of photons.

Southern Sky

In the Southern Sky, the background is dominated by muons produced in atmospheric showers. This kind of background is present only in the Southern Sky because it is shielded by the Earth in the Northern Sky, and atmospheric muons produce the same signature of a neutrino-induced muon track. In this specific case, we also need to reject the so-called muon bundles, i.e. a set of muons that are produced in an air shower and travel along the same direction. Veto techniques can be used to deal with this kind of events, for example considering only the so-called starting tracks, i.e. tracks that originate inside the fiducial volume of the detector, but this drastically reduces the event rate, from 50 000 events/year to 180 events/year [60], thus it is not applicable in this specific case.

The variables that are used in the BDT are:

- Mis-reconstructed events are only a small concern and they can be treated using the same variables used in the Northern Sky
- Muon bundles are often reconstructed as linear tracks, but some differences in the distribution of the time residuals are usually observed. In particular, some pulses are detected earlier or later than expected. This can be exploited to reject those kind of tracks.
- Also the light deposition profile presents differences between single muons tracks and muon bundles. Single high energy muons will undergo stochastic energy losses, while muon bundles are less likely to undergo this kind of processes. Identifying these losses provides a tool to select single muon tracks.

Further information about the training procedure can be found in [61].

The very last step of the event reconstruction, as reported in Figure 4.1, is the **angular error estimation**. This quantity represents the uncertainty on the reconstructed direction and has the dimension of an angle.

There are three different methods to estimate the angular error of an event: the *Cramér-Rao estimation*, the *Paraboloid Method* and the *Bootstrapping Method*.

The **Cramér-Rao estimation** exploits the Cramér-Rao inequality [62] which states that the best attainable variance of a statistical estimator is bounded from below by the inverse of the Fisher Information Matrix, I, which is defined as follows:

$$I(\vec{x}_i, \vec{x}_j) = -\left\langle \frac{\partial^2}{\partial \vec{x}_i \partial \vec{x}_j} \log \mathcal{L}(\vec{x}|t_{res}) \right\rangle_{t_{res}} \tag{4.14}$$

Defining $\vec{x} = (\vec{r_0}, \theta, \phi)$ the parameters that describe the track, the covariance matrix elements are such that:

$$Cov(\vec{x}_i, \vec{x}_j) \geq I(\vec{x}_i, \vec{x}_j) \tag{4.15}$$

By construction, the diagonal elements of the Fisher matrix correspond to the inverse of the squared angular uncertainties along the zenith and the azimuth. Thus we can extrapolate σ_ϕ and σ_θ and combine them to estimate the total angular uncertainty as follows:

$$\sigma = \sqrt{\frac{\sigma_\theta^2 + \sigma_\phi^2 \sin^2\theta}{2}} \tag{4.16}$$

The great advantage of this method is that it is purely numerical and it doesn't need minimisation procedures, so it is fast ($\approx$ 0.01s per event) [63]. However, it is also the least precise, especially for low-energy events.

The **Paraboloid Method**, instead, exploits the shape of the negative logarithm of the likelihood profile around the minimum to estimate the angular uncertainty. The shape around the minimum is well approximated by a paraboloid, i.e. a two-dimensional Gaussian. The value of the likelihood is estimated using 24 points around the minimum and a these points are fitted to a paraboloid. Since the paraboloid has a Gaussian shape, we know that:

$$-\log \mathcal{L}(x \pm \sigma_x) \approx -\log \mathcal{L}(x) + 0.5 \tag{4.17}$$

and the paraboloid fit allows to estimate the variance of the bi-variate distribution as:

$$\sigma = \sqrt{\frac{\sigma_x^2 + \sigma_y^2}{2}} \tag{4.18}$$

This approach is slower than the previous one, but the estimate of the angular error is more precise.

The last method that can be used to estimate the angular uncertainty of the events is the so-called **Bootstrapping method**. This method is very useful when the theoretical distribution of the random variable is not known, it exploits a random re-sampling with replacement to the available set of observations. In this case the unknown distribution corresponds to direction of the track, and the empirical set of events are pulses received by the DOMs. A bootstrapped event is created by randomly sampling pulses from the empirical distribution, the sampling stops when the total charge of the sampled event equals the total charge of the

	MuEX < 4 TeV	MuEX ≥ 4 TeV
$N_{Ch} < 300$	Paraboloid	Bootstrapping
$N_{Ch} \geq 300$	Paraboloid	Cramér-Rao

Table 4.1: Angular uncertainty estimator based on the reconstructed energy and the number of hit DOMs N_{Ch}. Taken from [50].

original event [64]. The process is repeated several times, in order to construct a sample of re-sampled events. The directional reconstruction is applied to each re-sampled event and the angular uncertainty of the original event is calculated as the median angular difference of the bootstrapped events [65].

Depending on the properties of each event, one of these three approaches is used to estimate the angular uncertainty of each event. A per-event approach is used so that each uncertainty can be computed with the highest possible precision using the appropriate method. In fact, the performances of the different methods depend on the properties of the event. In particular, the number of hit DOMs and the energy of the particle influence the performance of the algorithm. As summarised in Table 4.1, the Paraboloid method works better for relatively low energy events. For high energy events, whose track involves less than 300 DOMs, the Bootstrapping method is the most efficient, while for high energy events that leave a signature on more than 300 DOMs, i.e. very long and well reconstructed tracks, the Camér-Rao method provide the best estimate of the angular uncertainty in the shorter possible time.

One of the key points of this whole process has to do with the fact that the whole filtering procedure needs to be as fast as possible, in order to make this analysis feasible for real-time studies. As a consequence, efforts have been made to construct the fastest and most efficient reconstruction chain possible. From the very first step up to the angular error estimation, the median time to perform the whole online reconstruction is ≈ 1 s [50]. The events are stored using the JavaScript Object Notation (JSON) format and, a part for a set of numbers that are useful for the identification, they contain information about their direction, the energy estimate and the angular uncertainty.

4.1.6 GFU data samples

At this point, the event selection and reconstruction procedure is completed. The rate of the events is ≈ 6.5 mHz and the data that passed the GFU filter are now stored in the GFU samples, that are sent to Madison via the Iridium satellites. The data are now ready to be used for the analysis carried out in this work.

The events stored in the GFU samples are neutrino-induced muon candidates, but it is not guaranteed that the event filtering procedure selects only events of astrophysical origin. In Figure 4.4 the expected contribution to the data sample from different types of events is shown. In the Northern Sky ($\delta > 0^\circ$) the atmospheric muon contribution is suppressed. This indicates that the GFU filter successfully rejects the reconstructed down-going tracks. The main background component is given by atmospheric neutrinos. Then, in order of importance, the major contribution to the data set are given by astrophysical muon neutrinos, astrophysical tau neutrinos and astrophysical electron neutrinos. The smallest contribution is given atmospheric electron neutrinos.

In the Southern Sky ($\delta < 0^\circ$), instead, the data set is almost completely filled with atmospheric muons. This is why the events selection chooses more energetic events in this region

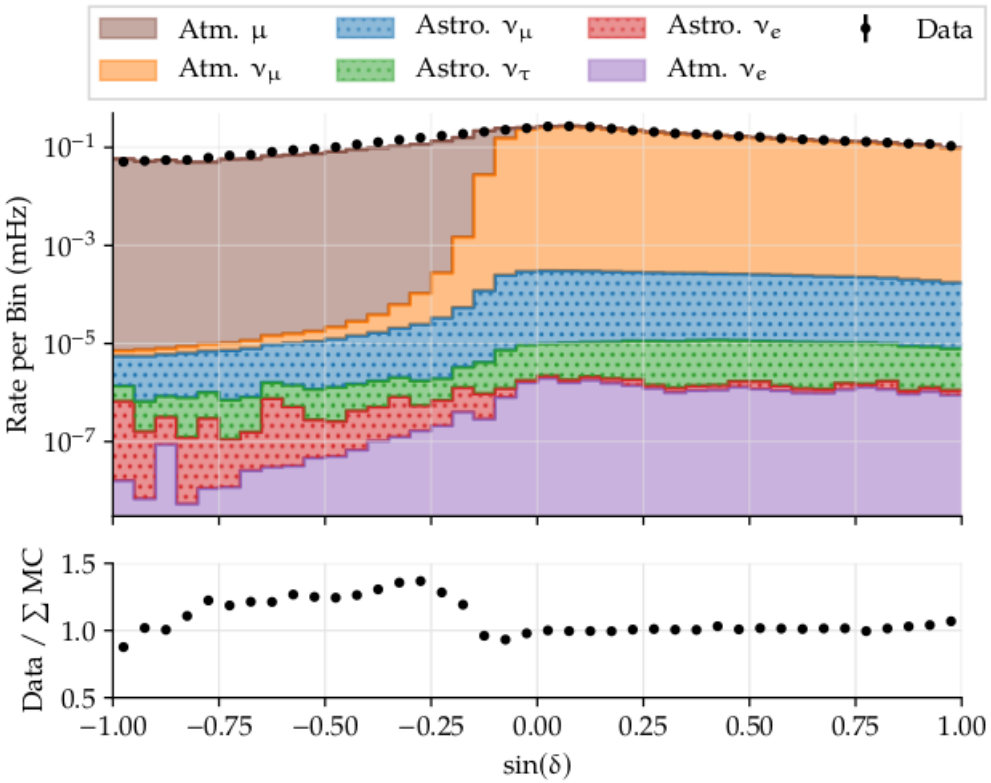

Figure 4.4: Event distribution at the final event selection level as a function of the declination. Data is drawn in black. The coloured areas show the contributions from atmospheric (solid) and diffuse astrophysical (dotted) fluxes based on simulations. Below, the ratio between the total amount of data and the sum of the simulated samples are shown. (Image taken from [50].)

of the Sky. Since a detailed simulation of the expected data in not available for $\delta < 0°$, the agreement between data and simulation is worse than in the Northern Sky.

The GFU sample was originally thought and designed for being employed in multi-messenger studies of high energy neutrinos and gamma-rays, but it is now widely used by the IceCube collaboration for various analyses involved in the search of neutrino sources [66–68].

Two different versions of the GFU sample are currently available for IceCube analyses. The first one is the one we just described, the other sample, which we will refer to as *smoothed* sample, is subject to an additional BDT cut in the Southern Sky, and it is the one that is currently used for the GFU analysis.

The final cut applied in the BDT is chosen such that the best discovery potential to point sources is achieved. The cut assumes different values according to the declination and it is chosen according to the expected spectral index of the flares, which is unknown and thus needs to be assumed a priori. In the Northern Sky the measurement of the astrophysical diffuse flux of neutrinos [29] is used as a reference. In the Southern Sky, where only high energy events are selected, a hard spectral index ($\gamma = -2$) is used. As a consequence, since different hypotheses are used in the two hemispheres, the cut is not continuous around the horizon.

In order to make it continuous and to make sure that the sample can be successfully used for a uniform likelihood analysis, a joined polynomial cut was implemented in the region around the horizon. The function is called *zenith smoothing function*. After this additional cut, the event rate is slightly reduced in the Southern Sky, but both the discovery potential and the sensitivity are unchanged, meaning that the cut only acts on the background.

4.2 Search Method for Time-Variable Point Sources

After constructing a sample of track-like neutrino candidates, a search method for the real-time search of astrophysical sources of neutrinos needs to be implemented. The analysis used in this work follows a time-dependent approach. In this Section, the likelihood method used for this analysis will be introduced, with a particular focus on the Time-Clustering algorithm and on the motivation behind the choice of a time-dependent approach.

4.2.1 Probability density functions

As we mentioned in Section 4.1.6, the GFU sample doesn't contain only events that have an astrophysical origin. Since we need to develop an analysis for the identification of astrophysical sources, the next step is to construct a statistical test that allows to quantify the probability that a certain event is a signal-like event (i.e. it has astrophysical origin) or it is a background event.

So, we assign to each event a probability of being a signal event, S_i, and a background event, B_i. These two probabilities are defined considering two properties of the events: the energy of the events and their direction. So, calling P_{energy} and P_{spatial} the energy and spatial probability density functions, respectively, we define the signal and background PDFs as:

$$\begin{aligned} S_i &= P^S_{\text{energy}}(E|\vec{x},\gamma) \cdot P^S_{\text{spatial}}(\vec{x}|\vec{x}_{src},\sigma) \\ B_i &= P^B_{\text{energy}}(E|\vec{x}) \cdot P^B_{\text{spatial}}(\vec{x}) \end{aligned} \tag{4.19}$$

where $\vec{x}_{src}$ is the location of the source, $\vec{x}$, σ and E are the direction, the angular uncertainty and the energy of the event, and γ is the power-law index of the energy spectrum.

The construction of the spatial PDFs exploits the fact that the background is uniformly distributed in the sky, while astrophysical events should cluster around the source location. P^S_{spatial} quantifies the probability of an event of being of astrophysical origin measured according to the distance of the event from an hypothetical source location.

$$P_{\text{spatial}} = \frac{1}{2\pi\sigma^2} \exp\left(-\frac{\Delta\Psi(\vec{x},\vec{x}_{src})}{2\sigma^2}\right) \tag{4.20}$$

where $\Delta\Psi(\vec{x},\vec{x}_{src})$ is the angular distance between the event and the source. The events that have a better localisation, i.e. they have a small angular uncertainty, are given a higher weight with respect to poorly localised events. The point-spread function is assumed to be a circular, two-dimensional Gaussian distribution.

The background PDF, instead, is constructed from archival data and it quantifies the probability of an event to be found with a particular direction and energy under the background assumption. The background event rate is both zenith-dependent and azimuth-dependent. The zenith dependence is due to the different path length the neutrinos have to traverse in the Earth and the varying filtering efficiency, the azimuthal dependence arises because of the structures in the geometry of the detector.

In Figure 4.5 the background PDF is displayed. The structures produced by the detector geometry are clearly visible. A part from these structures, the azimuthal distribution the PDF is almost uniform. In fact, being IceCube located at the South Pole, the effects due to Earth's rotation are mitigated.

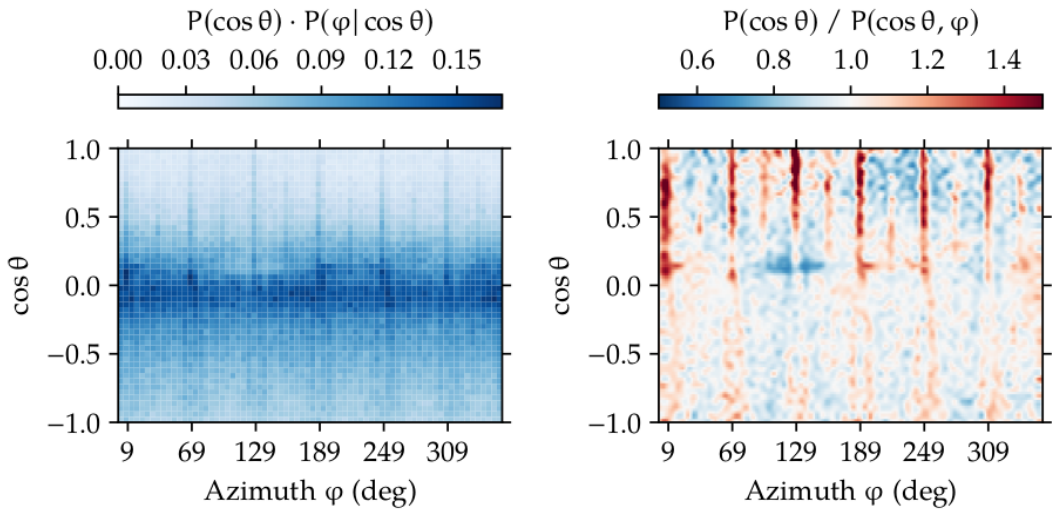

(a) Background PDF (b) Azimuthal asymmetry

Figure 4.5: Spatial background PDF. Left: probability distribution of events in detector coordinates, azimuth ϕ and zenith θ, as it is obtained from archival data. Right: deviation of the two-dimensional distribution from a one-dimensional one, highlighting the symmetry axes of the detector. (Image taken from [50]).

The energy PDF, instead, is constructed from simulations. The distribution of the energy of the neutrinos is expected to follow a E^{-2} spectrum under the assumption of Fermi acceleration, which is close to the spectrum measured for the diffuse astrophysical neutrino flux, $E^{-2.19}$ [29]. In comparison, the atmospheric neutrino flux is much softer, following a power law of roughly $E^{-3.7}$. In order to account for declination dependent effects, the construction of the PDF is performed in declination bands.

The signal PDF is created using the energy estimate provided by MuEX method for different spectral indices. The chosen spectral index ranges from -1, harder than the diffuse astrophysical flux, to -4, softer than the expected neutrino background.

The background PDF in the Northern Sky is created using archival data. In the southern sky, such an approach is not possible due to the poor agreement between data and simulation. So, the background PDF is generated from data, allowing a conservative, but uniform treatment of the entire sky.

4.2.2 Likelihood function

The signal and background PDFs can now be combined into a likelihood. Considering a sample of N neutrino-induced muon events, the likelihood is defined as the product of the probabilities of finding each event [69]:

$$\mathcal{L}(n_s, \gamma) = \prod_{i=1}^{N} \left(\frac{n_s}{N} S_i(\vec{\theta}_i|\gamma) + \left(1 - \frac{n_s}{N}\right) B_i(\vec{\theta}_i) \right) \tag{4.21}$$

where $\vec{\theta}_i$ are the variables that describe the properties of each event (direction, energy and angular uncertainty), n_s (the number of signal events) and γ (the spectral index) are the two free parameters, whose estimates will be the outcome of the algorithm used for this analysis.

The estimate of n_s and γ is obtained through likelihood maximisation. To quantify the probability of the fit to represent a neutrino flare a likelihood ratio test is performed, comparing the likelihood (4.21) with the background-only expectation, which corresponds to the case in which $n_s = 0$, i.e. we don't see any signal event. In the case of $n_s = 0$ the value of γ is irrelevant.

In order to perform this comparison, we define the Test Statistics Λ as:

$$\Lambda = 2 \log \left(\frac{\mathcal{L}(n_s, \gamma)}{\mathcal{L}(n_s = 0)} \right) \tag{4.22}$$

Using the likelihood definition given in (4.21) we can write the Test Statistics as:

$$\begin{aligned} \Lambda &= 2 \log \left[\frac{\prod_{i=1}^{N} \left(\frac{n_s}{N} S(\vec{\theta}_i|\gamma) + \left(1 - \frac{n_s}{N}\right) B(\vec{\theta}_i) \right)}{\prod_{i=1}^{N} B(\theta_i)} \right] = \\ &= 2 \sum_{i=1}^{N} \left[\log \left(\frac{n_s}{N} S(\vec{\theta}_i|\gamma) + \left(1 - \frac{n_s}{N}\right) B(\vec{\theta}_i) \right) - \log B(\theta_i) \right] = \\ &= 2 \sum_{i=1}^{N} \log \left[1 + \frac{n_s}{N} \left(\frac{S(\vec{\theta}_i|\gamma)}{B(\theta_i)} - 1 \right) \right] \\ &= 2 \sum_{i=1}^{N} \log \left[1 + \frac{n_s}{N} \left(w_i - 1 \right) \right] \end{aligned} \tag{4.23}$$

where w_i is the weight of each event. Since the tracks in the GFU sample have an angular resolution of about 1°, the events that are more than a few degrees far from the hypothetical source location are exponentially suppressed (see Equation (4.20)). This means that the signal probability of these events will be ≈ 0, and so will their weight. Assuming that only a number N' of events out of the total N events are sufficiently close to the source to contribute to the analysis we can simplify the expression in this way:

$$\Lambda = 2 \sum_{i=1}^{N'} \log \left[1 + \frac{n_s}{N} \left(\frac{S(\vec{\theta}_i|\gamma)}{B(\theta_i)} - 1 \right) \right] + 2(N - N') \log \left(1 - \frac{n_s}{N} \right) \tag{4.24}$$

so that it will not be necessary to calculate the weight of the $N - N'$ events that are too far from the source to contribute to the likelihood.

Since the logarithm behaves monotonically and the background expectation is uniform we can maximise directly the Test Statistics Λ.

Time Integrated Approach

Up to now, the temporal information has been completely neglected. The likelihood function defined in (4.21) is designed to consider all the events contained in the data sample. However, past time-integrated searches for this kind of events have been inconclusive [65, 70].

The main goal of the Gamma-ray Follow-Up analysis, that will be explained in detail in the next section, is to manage to identify astrophysical neutrino flares from Active Galactic Nuclei. In fact, sources of high energy radiation, which are considered also candidate sources of astrophysical neutrinos, are very variable in their emission, thus, the temporal structure of the high energy particles emission of these objects needs to be taken into account.

Time Dependent approach

In order to take into account the temporal variability of neutrino emission, we need to add the temporal information in the likelihood formulation. The most generic and model independent approach consists in performing the likelihood analysis over a time window, considering only the events contained inside the given interval. In order to use the most general approach possible, the time windows are box-shaped, i.e. bounded by a start time and an end time.

Introducing the temporal information simply by considering subsets of events received over a certain time window has a side effect. In fact, when analysing subsets of events of different lengths, longer flares will suffer the presence of background events much more than shorter flares, resulting in favouring short flares. Thus, a penalty factor for short flares needs to be introduced. The expression of the Test Statistic for the time-dependent analysis is:

$$\Lambda = 2\log\left(\frac{\mathcal{L}(n_s,\gamma)}{\mathcal{L}(n_s=0)}\cdot\frac{\mathcal{U}(t_i,t_j)}{T_{max}}\right) \tag{4.25}$$

where $\mathcal{U}(t_i,t_j)$ is the uptime of the detector during the analysed time window ($[t_i,t_j]$), and T_{max} is the maximum allowed flare duration. The length of tested time windows is not chosen beforehand: it becomes one of the fit parameters.

The algorithm that is used to find the time window that has the highest probability of containing a neutrino flare is the **Time-Clustering algorithm**.

Time-Clustering algorithm

The Time-Clustering algorithm performs the time-dependent likelihood analysis over different time windows and considers different combinations of events. In Figure 4.6 we show a sketch of its working mechanism.

In order to run an efficient analysis, we need to put some constraints. First of all, in order to make the analysis efficient, an upper limit on the flare duration, T_{max}, needs to be set. The choice could be based upon some theoretical predictions, but, in absence of any prior knowledge, the value of T_{max} is optimised, based on simulations, at the point at which the sensitivity becomes comparable to the time-integrated analysis timescale. In the case of the Time-Clustering algorithm, the maximum analysed timescale is set to 180 days.

Additionally, it can be shown that combining events that have a S/B ratio smaller than 1 doesn't lead to positive Test Statistic results. This means that it is not necessary to test *all* the possible combination of events inside a sample, but the algorithm can be designed to test only the time windows that satisfy some specific properties. This also reduces the computational time needed to perform the analysis. the criterion applied in the case of the Time-Clustering algorithm is to perform the likelihood analysis only over time windows that are bounded by two events that have both $\mathrm{S/B} > 1$.

The algorithm is run whenever an event with $\mathrm{S/B} > 1$ is detected. This event is called *trigger* and we consider this event to be the end of the analysed time window. The starting point of the time window is chosen among all the events that have overcome the S/B threshold before the trigger, going back in time up to the maximum flare duration.

The outcome of the Time-Clustering algorithm corresponds to the results of the likelihood fit which lead to the highest test statistics out of all the tested time windows.

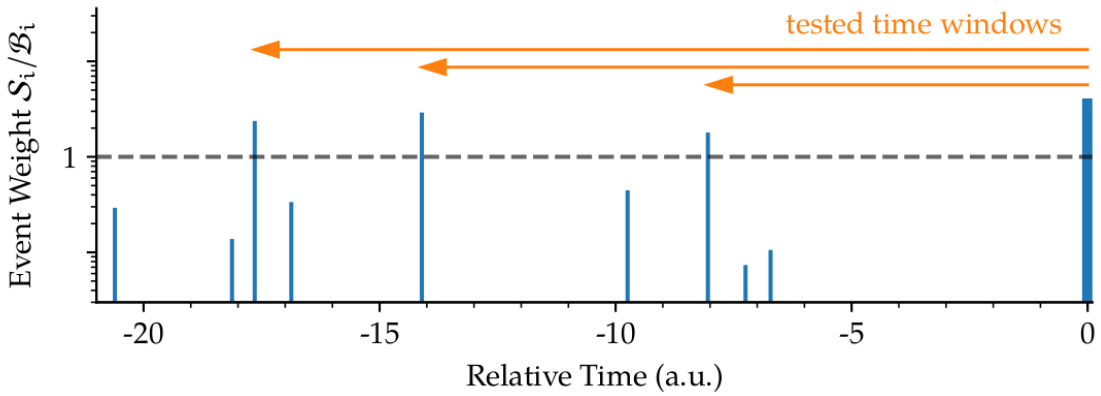

Figure 4.6: Sketch of the Time-Clustering algorithm. The vertical bars represent the weights of the events. The right-most event is the trigger. Orange arrows denote the time windows in which the likelihood analysis is applied. The time windows are bounded by two events whose weight exceeds a defined threshold, which is set to 1 (dashed grey line). (Image taken from [50].)

In Chapter 5 we will discuss in detail the performance of the analysis both in the time-integrated and time-dependent approaches.

4.2.3 Gamma-ray Follow-Up analysis

The Gamma-ray Follow-Up (GFU) analysis employs the Time-Clustering algorithm for real-time studies of selected astrophysical sources (source catalogue analysis) or the whole sky (All-Sky analysis). The main purposes of this analyses are identifying astrophysical sources of neutrinos and favouring follow-up observation of interesting neutrino flares with multi-messenger observations of electromagnetic counterparts. In order to do this, an alert infrastructure that performs the analysis in real-time was implemented. The first version of the IceCube GFU alert system dates back to 2012 [63], but a similar infrastructure was already implemented in AMANDA [53] years before, and it has been updated several times over the years. The current working version of the GFU alert system is the one that is used for the results reported in this work and in [50].

The alerts system is designed to communicate the detection of interesting neutrino flares to the IceCube Collaboration and to the Astrophysical community. The alerts contain information about the significance of the alerts, the events that contributed to the flare, the time window over which the flare was detected, the fit parameters and the position of the source.

The alert production mechanism is sketched in Figure 4.7, where the temporal evolution of the significance of the triggers is displayed. The dots represent the outcome of the Time-Clustering algorithm for each detected trigger. So, each dot corresponds to an event that overcame the S/B threshold and it carries information about the time window in which the highest significance fit was found for that specific trigger. So, each dot corresponds to a different time window and a different combination of events. The real-time analysis, together with IceCube's capability of constantly observing the entire Sky, allows to monitor the candidate neutrino sources by performing the Time-Clustering analysis for each event that is detected in their direction. As soon as the significance of the trigger goes above a predefined threshold, an alert is sent (dark orange dots).

The alert is produced at the IceCube computing server in Madison (WI). The total time needed to produce an alert, starting from the detection and processing of the event that

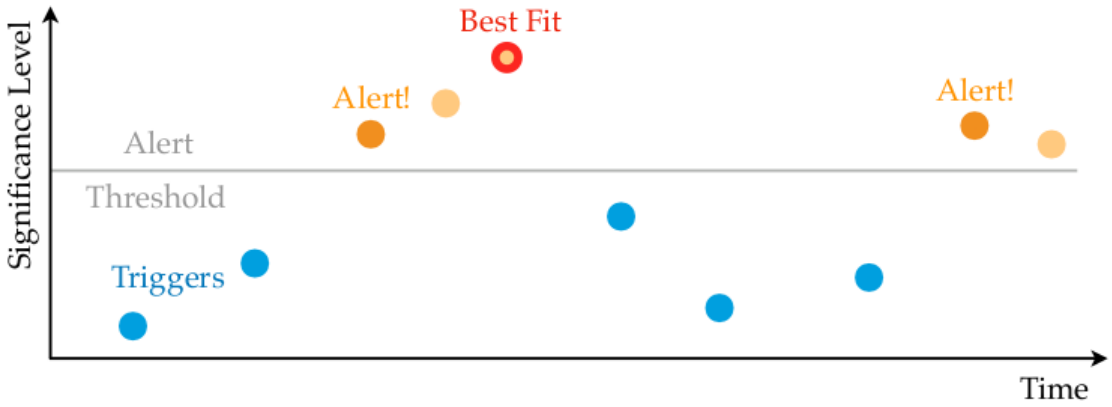

Figure 4.7: Sketch of alert production mechanism. The plot shows the temporal evolution of the significance of the triggers. Each dot represents an outcome of the Time-Clustering algorithm, i.e. a different trigger and, as a consequence to a different time window and a different combination of events. The alert production mechanism is explained in detail in the text. The blue dots represent the triggers that don't overcome the alert threshold, the alerts are displayed in dark orange, the muted triggers in light orange and the best fit is underlined in red. (Image taken from [50].)

triggers the analysis up to the moment in which the alert is released is, on average, 12 minutes [63]. The alerts are usually sent via email to the Real-time Oversight Committee (ROC) of the IceCube collaboration and to partner Čerenkov telescopes.

In order to avoid spamming the collaboration and the partners with emails, a muting mechanism was implemented. After an alert is sent, the information regarding the following triggers above the threshold is not communicated either to IceCube collaboration or to partners, meaning that we are unable to know how the flare develops after the alert is sent (light orange dots). The muting mechanism also allows to preserve blindness and avoid biases in the offline analyses, and it is released only when the significance drops below the significance threshold.

So, the real-time online GFU analysis consists in generating and spreading neutrino flare alerts we just described to the partner telescopes.

The GFU analysis is also periodically run offline. The purpose of the offline analysis is the search for the most significant detected flare, the *best fit*, which cannot be identified through the online analysis because of the muting mechanism that prevents us to observe the full development of the detected flares. In order to preserve blindness, the search for the best fit returns as output only the outcome of the Time-Clustering algorithm that produced the highest value of the Test Statistics of all the tested sources.

The highest significance flare is denoted as *best fit* and it is highlighted in red in Figure 4.7. The purpose of this analysis is to look for high significance flares and check if any flare has overcome the discovery threshold.

There are two GFU analyses currently running. The **Source Catalogue** analysis and the **All-Sky** analysis.

Source Catalogue Analysis

The GFU Source Catalogue analysis monitors a list of known gamma-ray emitters to be observed by the three partner Čerenkov telescopes: MAGIC, VERITAS and H.E.S.S..

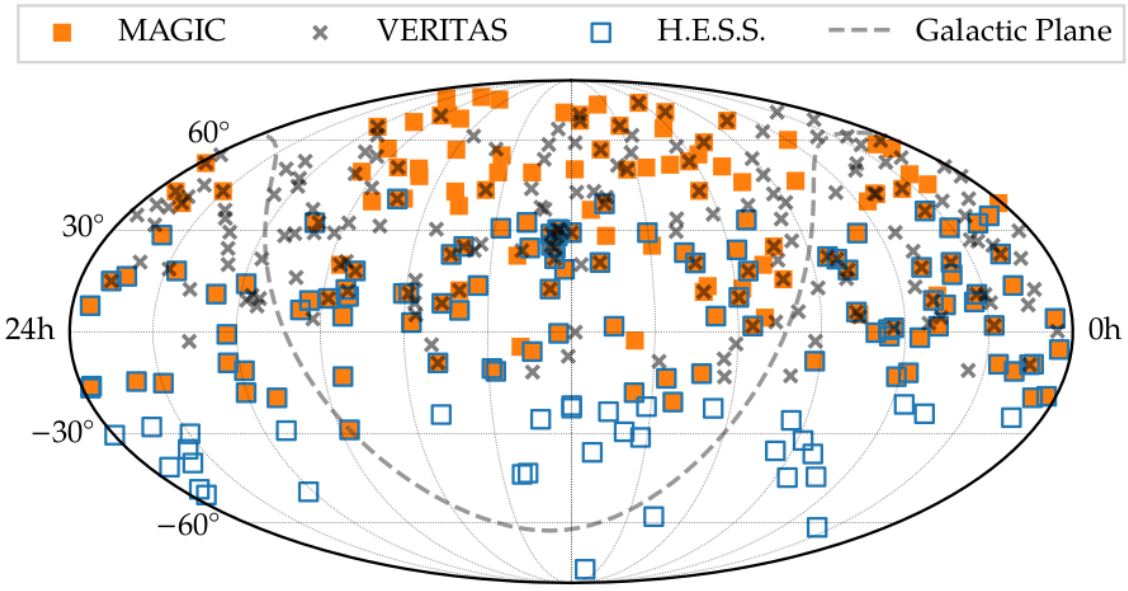

Figure 4.8: Skymap of the monitored Gamma-Ray sources and the corresponding experiments. Due to visibility criteria, MAGIC and VERITAS sources are located mainly in the Northern Sky, while H.E.S.S. sources are in the Southern Sky. (Image taken from [50])

IceCube has been collaborating with MAGIC and VERITAS telescopes since the beginning of the GFU program [63]. In fact, these telescopes are located in the Northern hemisphere, where IceCube has better sensitivity and the atmospheric background is suppressed by Earth absorption. H.E.S.S. telescope, instead, is located in the Austral hemisphere, and it was included in the program in 2018, during the latest update of the GFU platform [50].

The monitored sources are displayed in Figure 4.8. They are selected according to the following criteria, enhancing the probability of positive detections:

- The sources must be visible for some time during the year
- Sources must be extra-galactic, the Redshift z must be known and $z \leq 1$. This constraint corresponds to the most-distant object that has been observed in very high energy gamma-rays. Further objects cannot be observed by gamma-ray telescopes because of the interaction of high energy photons with the Extragalactic Background Light, as we mentioned in Section 2.3. [71]
- The Sources must be variable in their high energy emission
- The flux measured by Fermi-LAT is extrapolated above 100 GeV. The integrated flux above 100 GeV has to exceed the 5σ discovery potential of the telescope in 2 hours (H.E.S.S.: 5 h) of observation.

The selection results in 179 sources for MAGIC, 190 sources for VERITAS, and 139 sources for H.E.S.S.. Taking into account that some sources are present in more than one source list, a total of 339 sources is monitored. A complete list of the monitored sources can be found in [50].

The real-time analysis for catalogue sources consists in running the Time-Clustering algorithm whenever an event with S/B > 1 is detected in the vicinity of a monitored source. Any time a trigger overcomes the significance threshold, which is currently set to 3σ pre-trial, an alert is sent. The expected alert rate at this threshold is of ≈ 10/year for MAGIC

and VERITAS and $\approx 6/\text{year}$ for H.E.S.S. [50].

This work focuses on the Source Catalogue analysis, whose performance will be tested and discussed in the next chapter.

All-Sky Analysis

The All-Sky analysis was implemented with the last GFU update in 2018 and it consists of an unbiased search for signal excesses over the entire sky. This analysis removes the bias of the source lists and may reveal sources that have not been considered for time-dependent neutrino emission.

This means that any event with $S/B > 1$ triggers the Time-Clustering algorithm. Since we are dealing with an unbiased search, i.e. there is no underlying hypothesis about the event that triggers the analysis, the number of triggers will substantially increase, and the trial factors will increases as well. For this reason the alert threshold is set to an higher value, 4.5σ, to mitigate this effect and limit the number of false alerts.

The All-Sky analysis combines the Time-Clustering algorithm with a directional scan. In fact, the main challenge for this analysis consists in selecting the events that contribute to the candidate flares. Lacking a reference position, a tool to understand the location of the candidate sources is needed. The Hierarchical Equal Area isoLatitude Pixelization (HEALPix) [72] software, along with the Python wrapper *healpy*, allows to divide the sky into bins of equal area. The centre of each bin is treated as a source hypothesis, to which the Time-Clustering algorithm is applied.

Once a trigger is received, the area around the direction of the event is divided into a coarse grid (0.92° spacing) and the Time-Clustering algorithm is applied to each of the candidate source positions. The process is then iterated in the area in which the Time-Clustering algorithm returned the highest TS value and it stops for a grid spacing of $\approx 0.1^\circ$. This value is chosen based on simulations. It corresponds to the grid spacing value after which no significant improvement in the fit is observed. This value also corresponds to the average angular uncertainty of the events [50].

The expected alert rate for the All-Sky analysis is $\approx 1/\text{year}$.

The All-Sky analysis is not treated in this work but the latest results about the produced alerts and the best-fit location using archival data can be found in [50].

Chapter 5

Reproduction of Historical Results

In this chapter, we test the performances and the repeatability of the likelihood analysis and of the Time-Clustering algorithm reproducing some relevant historical results. The majority of the results shown in this chapter are obtained from the simulation of scrambled background with the injection of signal-like events. In the first place, we will describe how those simulations are performed. Then, we will introduce the statistical concept of *sensitivity*, we will reproduce the sensitivity curves for our analysis and we will build the Test Statistics (TS) distributions. We will also test the reconstruction of the fit parameters both in the time-integrated and in the time-dependent case and we will provide an estimate of the time needed for the algorithm to trigger an alert according to the characteristics of the injected flares. Finally, we will reproduce the historical online alerts and the previous best fit result of the GFU analysis for catalogue sources.

5.1 Toy Simulation on Scrambled Data

In order to produce the sensitivity curves and test the performances of the Time-Clustering algorithm, we perform toy simulations. We do this using real IceCube data scrambled in time and space coordinates.

For simulating a background scenario it is sufficient to shuffle a sample of events in time and convert the local detector coordinates, expressed in zenith (θ) and azimuth (ϕ), in equatorial coordinates, expressed in right ascension (α) and declination (δ) according to the new event times.
Since IceCube is located at the South Pole, the declination remains the same before and after the time scrambling, while the right ascension can be approximated as:

$$\alpha_{new} = \left(\alpha_{old} + (t_{old} - t_{new}) \cdot \frac{2\pi}{t_{sid}} \right) \mod 2\pi \tag{5.1}$$

where the subscript *new* indicates the new parameters, the subscript *old* the old ones, and $t_{sid} = 0.99726957$ days is the length of a sidereal day with respect to a solar day. This procedure allows to mask any possible signal cluster in the data set and to maintain the characteristics related to the detector effects without the need of performing detector simulations.

If we desire to simulate a neutrino flare, we need to perform an additional step, that consists in injecting a number of signal events into the dataset. The energy and the weight of the events are sampled from the PDFs described in Section 4.2.1. According to the characteristics

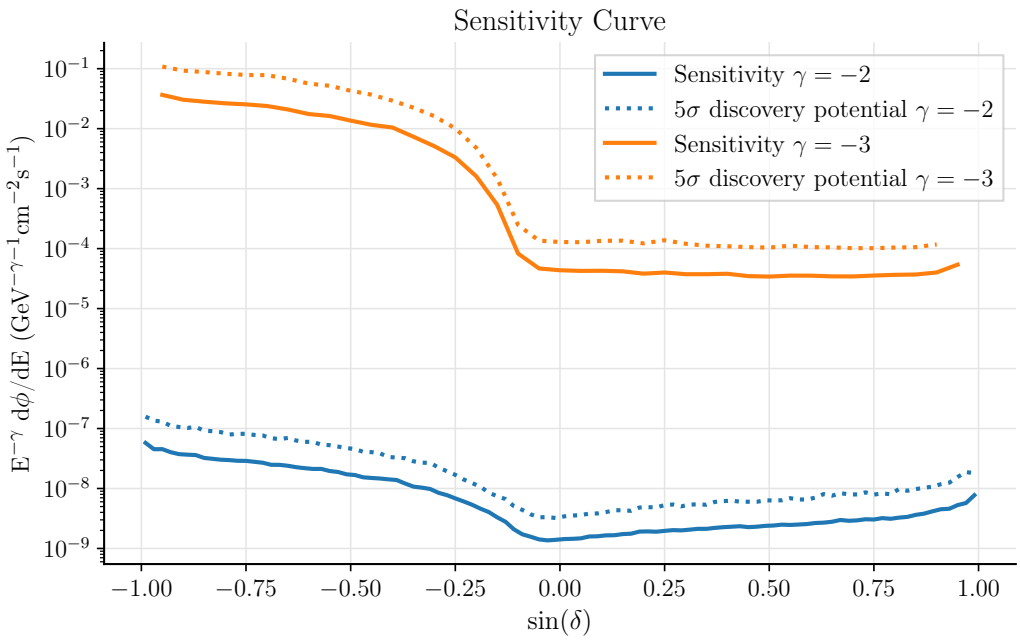

Figure 5.1: Sensitivity (solid) and 5σ discovery potential (dotted) for two different simulated fluxes ($\gamma = -2, -3$) over the whole range of declinations.

of the flare that we want to simulate and on its direction, the events are drawn from a MonteCarlo simulated data sample in a declination band of $\pm 5°$ around the declination of the simulated source. Those simulated events are then added to the background simulations. The injection of the events is uniform for both the time-integrated and the time-dependent simulation. In the latter case, the events are all injected inside a time window of custom duration randomly located inside the whole duration of the scrambled data set. The simulated signal events are then moved towards the direction of the simulated source and, after the coordinate redefinition, they are moved to their original coordinates. This is done in order to recreate a point-like source starting from events drawn from a diffuse flux simulation.

5.2 Sensitivity Curves

As we explained in Section 4.1, the detection of astrophysical neutrinos has to face the important challenge of a large irreducible background. Since the rate of events is low, the underlying statistical probability density is Poissonian.

A relevant parameter describing the experimental potential of a given observation is represented by the capability to constrain a given signal flux. For this purpose, the statistical concept of *sensitivity*, was introduced [73].

The definition of sensitivity depends on the chosen confidence level and on the power of the test, i.e. the probability of rejecting the null hypothesis when the alternative hypothesis is actually true. Within IceCube, the *sensitivity* is defined as the best possible upper limit which can be set on the neutrino flux at a confidence level of 90% in case of non-observation and the *discovery potential* is the flux that yields a 5σ discovery in 50% of cases.

In Figure 5.1 we represent the sensitivity and the 5σ discovery potential for two different simulated fluxes. The results are in agreement with the previous ones [50], indicating that the analysis is correctly reproduced. In the Southern Sky, where the tracks have a worse reconstruction and we suffer the atmospheric background we need higher fluxes in order to

be sure that we are observing a neutrino signal excess.

Moreover, for hard simulated fluxes ($\gamma = -2$) a lower flux is needed to detect a signal excess with respect to a softer flux ($\gamma = -3$), which is more similar to the atmospheric neutrino flux ($\gamma_{\text{atm}} = -3.7$), and, for this reason, is more difficult to be distinguished from the background and can be detected only in the case of intense fluxes.

5.3 Test Statistics Distribution

In Section 4.2.2 we described the likelihood analysis and we introduced the Test Statistics (TS) (4.22). In this section, we study the Test Statistics distribution for both the time-integrated and the time-dependent analysis for different spectral indexes and different signal strengths.

5.3.1 Time-integrated analysis

In Figure 5.2 and 5.3 we show the Test Statistics distributions for the time-integrated analysis for a simulated source at a declination $\delta = 45°$ with spectral index, respectively, of -2 and -3 and for different number of injected events.

In both cases we can see that the higher is the number of injected events, the broader is the distribution and the higher is the average value. This is consistent with the expectations: the higher the number of astrophysical events coming from a certain region in the sky, the higher is the probability of being in presence of a neutrino flare coming from that given direction.

The major difference between an injected spectral index $\gamma = -2$ (Figure 5.2) and $\gamma = -3$ (Figure 5.3) is the width of the distributions. For $\gamma = -3$ the maximum TS value is significantly lower than the ones obtained for a simulated γ of -2. This is due to the fact that, as we mentioned before, in an astrophysical flare with a soft spectral index, some signal events might be misidentified and considered as atmospheric neutrinos. As a consequence, we are able to evaluate with a higher TS value the flares that have a hard spectral index.

5.3.2 Time-dependent analysis

In this case, we show the distribution of the *best fit* value of the Test Statistics for each trial, i.e. the output of the Time-Clustering algorithm that provided the highest value of TS.

In fact, in the time-dependent case, the Time-Clustering algorithm tests all the possible combinations of events over different time windows looking for the most significant neutrino flare candidate. This is why, in the distributions displayed in Figure 5.4 and 5.5, we don't see the accumulation of TS values around zero as we do in the time-integrated case, where the fit is performed considering all the events inside the analysed sample. This indicates that the time-integrated approach is not as efficient as the time-dependent one for identifying neutrino flares.

In Figure 5.4 and 5.5 we show the distributions of the TS for a simulated source at a declination $\delta = 45°$ for a simulated spectral index of, respectively, $\gamma = -2$ and $\gamma = -3$ and for different number of injected events. The higher is the number of injected events, the higher is the average value of the TS and the broader is the distribution.

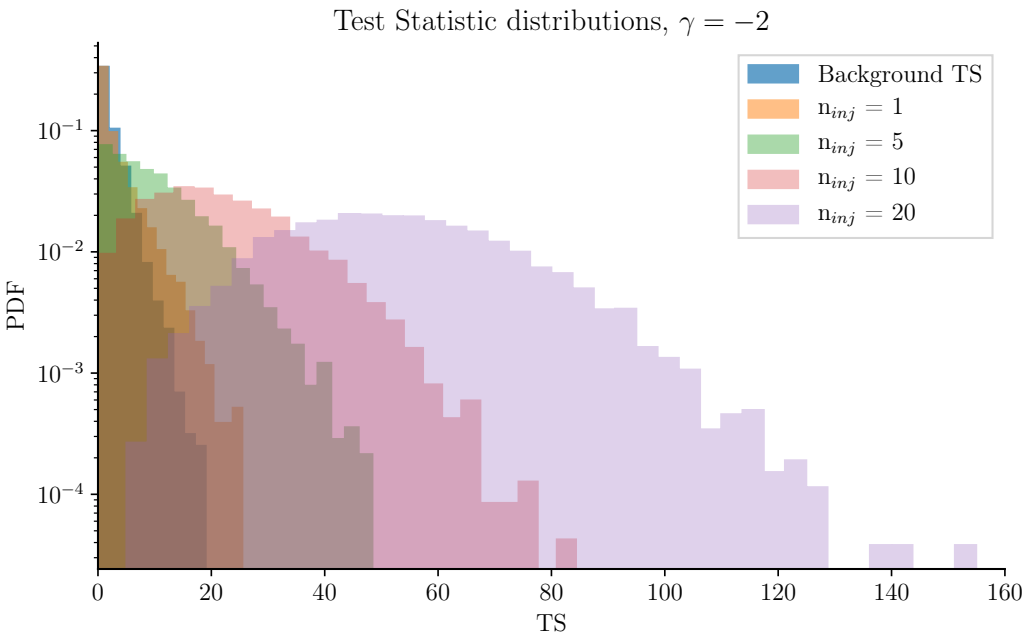

Figure 5.2: Test Statistics distribution for the time-integrated analysis for a simulated spectral index of $\gamma = -2$. The blue histogram represents the background, the others correspond to different numbers of injected signal events.

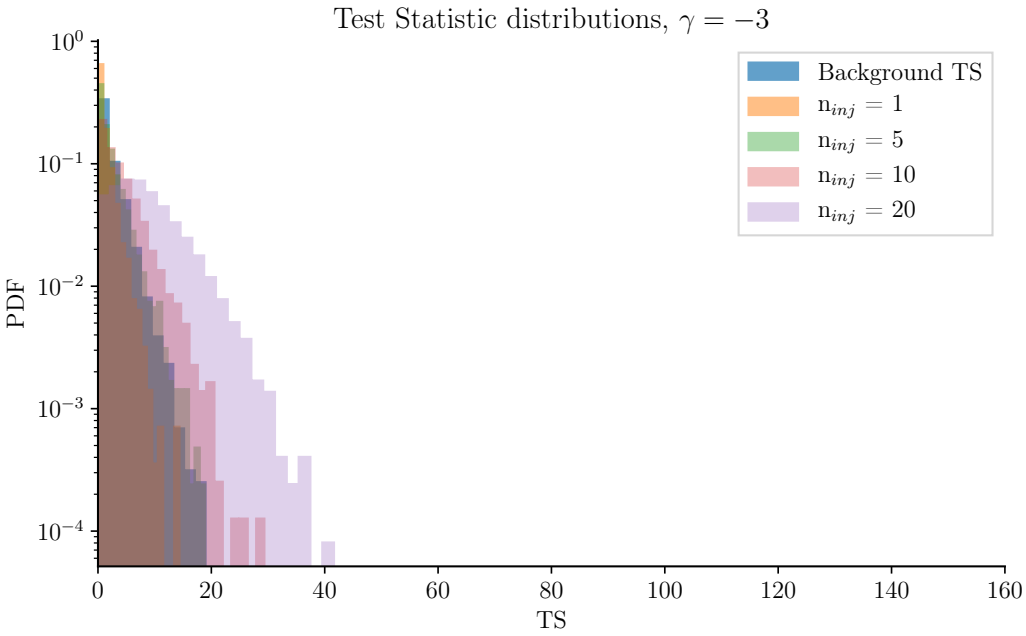

Figure 5.3: Test Statistics distribution for the time-integrated analysis for a simulated spectral index of $\gamma = -3$. The blue histogram represents the background, the others correspond to different numbers of injected signal events.

We notice, that the differences in the TS distributions for the two different spectral indexes follow the same behaviour we already observed for the time-integrated analysis. The softer is the flux (i.e. the closer to the atmospheric background), the more difficult will be the identification of astrophysical flares of neutrinos.

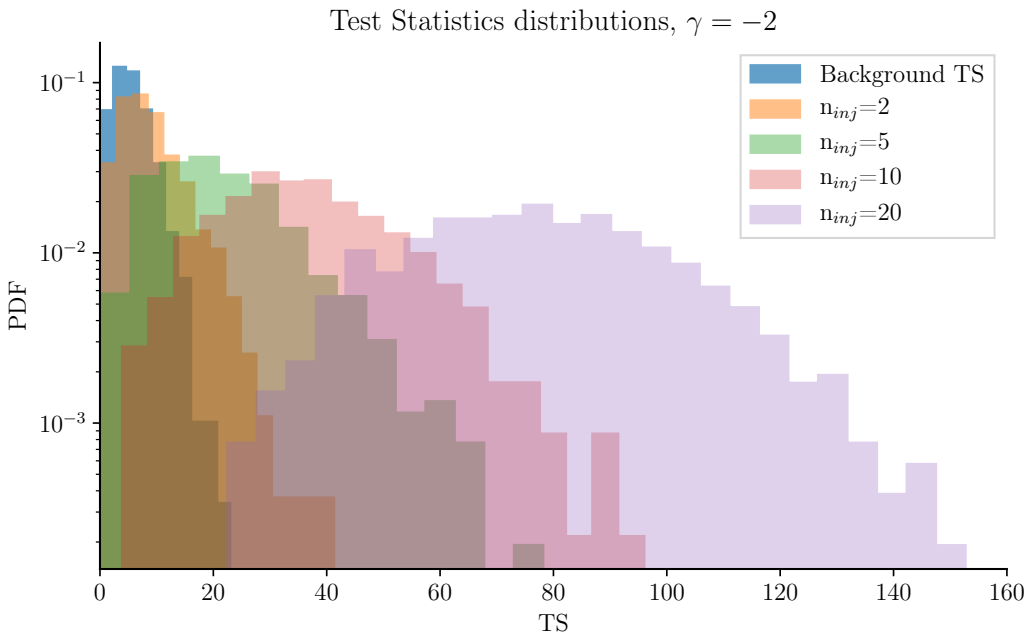

Figure 5.4: Test Statistics distribution of the best fit of the time-dependent analysis for a simulated spectral index of $\gamma = -2$. The blue histogram represents the background, the others correspond to different numbers of injected signal events.

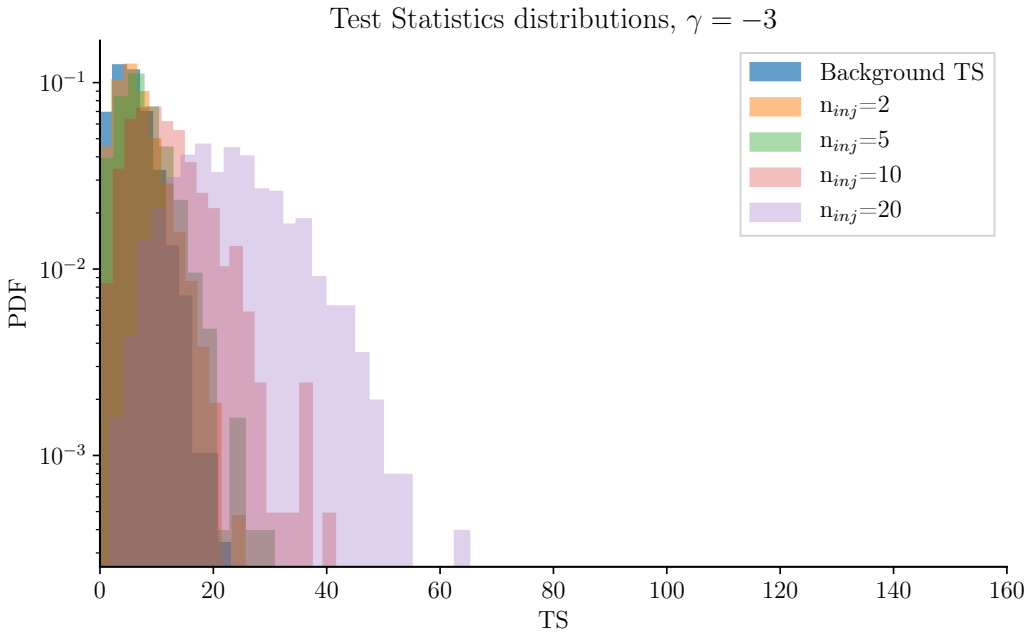

Figure 5.5: Test Statistics distribution of the best fit of the time-dependent analysis for a simulated spectral index of $\gamma = -3$. The blue histogram represents the background, the others correspond to different numbers of injected signal events.

5.4 Reconstruction of Neutrino Flares Parameters

The two parameters of the likelihood analysis are the number of signal events that contribute to the alert, n_s, and the estimated spectral index, γ.

In this section, we test the efficiency in the reconstruction for both the time-integrated and time-dependent analysis.

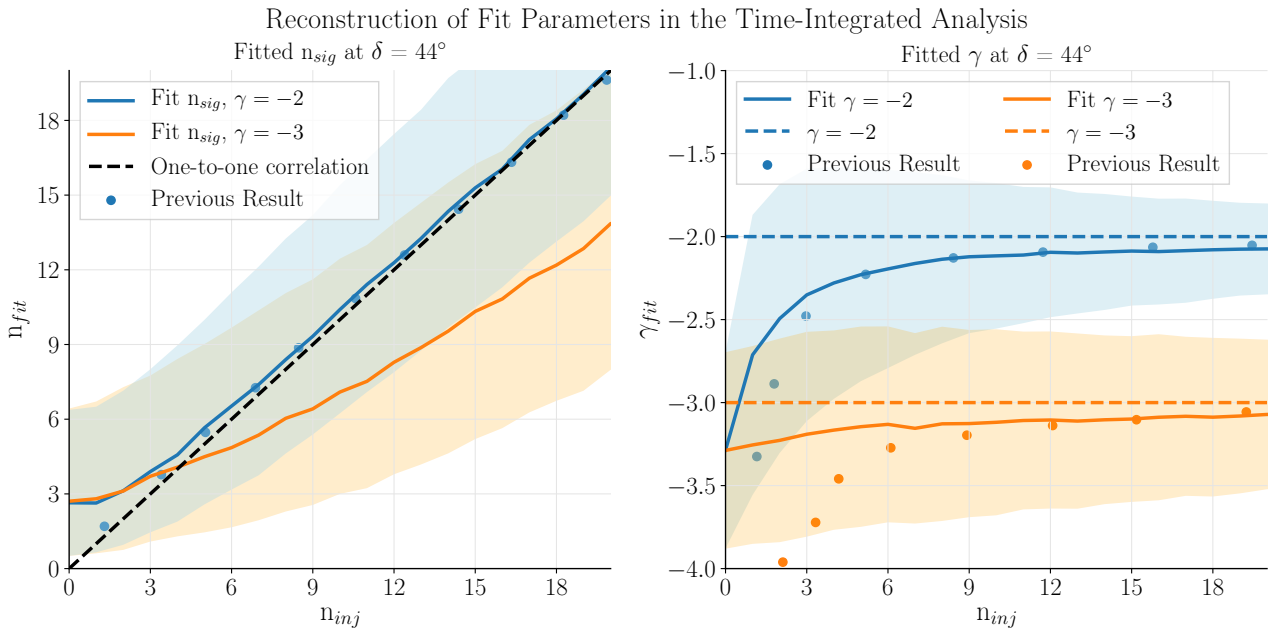

Figure 5.6: Reconstruction of fit parameters for two different injected spectral indices ($\gamma = -2, -3$) and 0 to 20 injected events for a simulated source at $\delta = 44°$. Left: Number of events. The dashed line corresponds to the one-to-correlation between the number of injected events and the fit result. Right: Spectral index: the dashed lines in the right plot represent the true injected parameters. The shadowed areas represent the 68% probability contours of the distributions. The dots represent the previous GFU results [50].

5.4.1 Time-integrated analysis

The time-integrated analysis performs the likelihood fit considering all the events of the analysed sample. The study of the reconstruction of the fit parameters, in this case, allows us to evaluate the performances of the likelihood fit and understand if it is feasible for this kind of analysis.

In Figure 5.6 we test the reconstruction of the fit parameters for different simulated spectral indices and number of injected events.
We compare our results with the previous GFU results. We notice that, except for a low number of injected events, the results superimpose with the previous ones. The discrepancies we notice for a low number of events are probably due to the fact that, especially in a time-integrated analysis, where we neglect the temporal distribution of the events, short flares are difficult to be identified, thus the algorithm is more likely to return background fluctuations rather than the injected flares. For the same reason, we observe a large spread in the estimate of the spectral index γ for a low number of injected events.

The number of injected events, instead, is well reconstructed for a spectral index $\gamma = -2$, while it is systematically underestimated for $\gamma = -3$. This is probably due to the fact that for a soft flux some events are interpreted as background.

5.4.2 Time-dependent analysis

We can test the performances of our analysis also in the time-dependent case. This is done studying the best fit of the MonteCarlo simulated flares. If the algorithm manages to recognise properly the injected flares, then the best fit result should provide an estimate of the parameters compatible with the simulated ones.

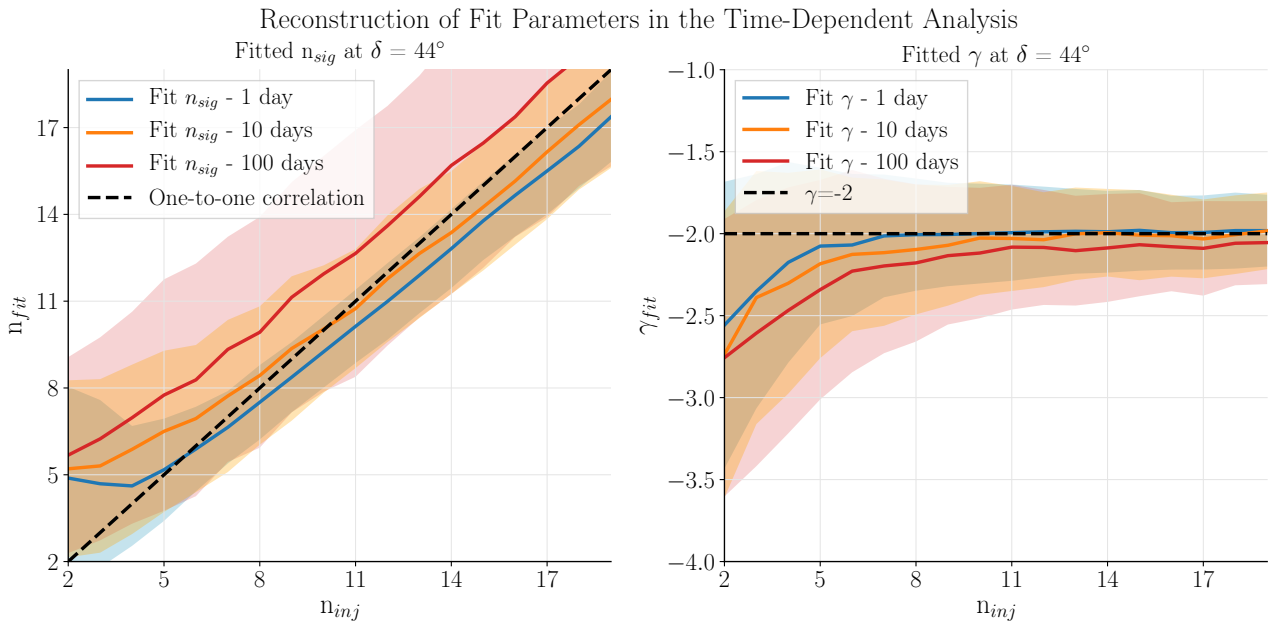

Figure 5.7: Reconstruction of fit parameters for three different flare duration, an injected spectral index $\gamma = -2$ and 2 to 20 signal events for a simulated source at $\delta = 44°$. Left: Number of injected parameters. The dashed line corresponds to the one-to-correlation between the number of injected events and the fit result. Right: Spectral index: the dashed line in the right plot represent the true injected parameters. The shadowed areas represent the 68% probability contours of the distributions.

In Figure 5.7 we show the reconstruction of the best fit parameters for three different flare durations. The number of events is overestimated for small signal strengths but converges as the number of events increases. In particular, for short flares (1 day and 10 days) the fit result converges to the expected value, while it is slightly overestimated for longer flares. This can be explained considering that, the longer is the time window, the higher is the probability of having some background events that are misidentified as signals. The spectral index estimate, instead, always converges to the true value for sufficiently strong signals.

Since we are now working with a time-dependent analysis, we have an additional fit parameter, i.e. the duration of the flare time window. In Figure 5.8 we show the reconstruction of the duration of the flare performed by the Time-Clustering algorithm. We can see that, in all the tested cases, for sufficiently high signal strengths, the estimate of the flare duration converges to the true value with approximately the same behaviour. This indicates that the Time-Clustering algorithm behaves in the same way for different flare durations. For small signal strengths, instead, we suffer the presence of the atmospheric background. This means that the best fit result is likely to be found in correspondence of a background fluctuation rather than in the time window corresponding to the simulated flare, producing a bias in the estimate of the flare duration. The reason why we don't observe this discrepancy for the other fit parameters is due to the fact that the background alerts are characterised, on average, by $n_s \approx 3 \sim 5$ and $\gamma \approx -3 \sim -2.5$, which are numerically close to the fit parameters of the simulated flares at small signal strengths, but their duration can vary in a wide range of values, from days up to several weeks, so differences emerge.

Nevertheless, we observe relevant discrepancies from the simulated values only for the estimate of the flare duration in the case of small injected signal strengths, thus we can conclude that the time-dependent analysis allows us to identify neutrino flares. Further results regarding the performances of the Time-Clustering algorithm for faint flares will be discussed in the next chapter.

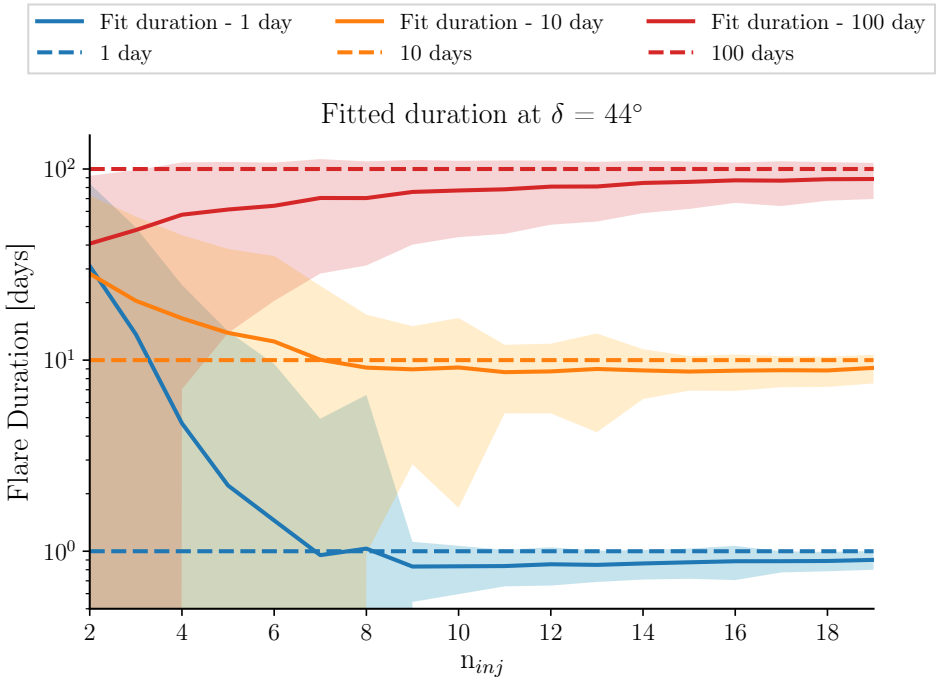

Figure 5.8: Reconstruction of the duration of the flare for three different injected flare durations, an injected spectral index $\gamma = -2$ and 2 to 20 injected events for a simulated source at $\delta = 44°$. The shadowed areas represent the 68% probability contours of the distributions.

5.5 Time After an Alert is Sent

An other relevant information is related to the time needed for the Time-Clustering algorithm to trigger an alert when a flare is injected. In fact, the sooner we recognise a neutrino flare, the more efficient we are in notifying the astronomical community of those signal excesses.

The time needed for the Time-Clustering algorithm to recognise a flare and produce an alert depends on the flux and on the coordinates. In Figure 5.9 we show the reproduction of the historical results [50]. On the horizontal axis we display the fraction of time needed for the Time-Clustering algorithm to trigger an alert normalised to the total flare duration. We show the results for three different flare durations: 1 day, 10 days and 100 days.

We can see that our results overlap fairly well with the previous ones. As expected, the stronger the flare, i.e. the higher the number of injected events, the sooner the algorithm will generate an alert. This means that intense flares are more suitable for real-time studies and follow-up observation than the faint ones.

The fact that the curves follow approximately the same behaviour for all the three tested durations indicates that the Time-Clustering algorithm has the same performances over different time windows, from timescales of the order of a few days up to several months. For long injected flares (100 days), we notice a saturation effect for small fluxes. This is probably due to the fact that very long and faint flares are difficult to identify, and, as a consequence, the reconstructed alerts are contaminated by background fluctuations. In fact, the plotted quantity saturates at approximately 60% of the total flare, and, since we are showing the average time that the Time-Clustering algorithm needs to produce an alert, and background fluctuations are random processes uniformly distributed in time and space, an average value of one half of the tested time window is compatible with a background scenario.

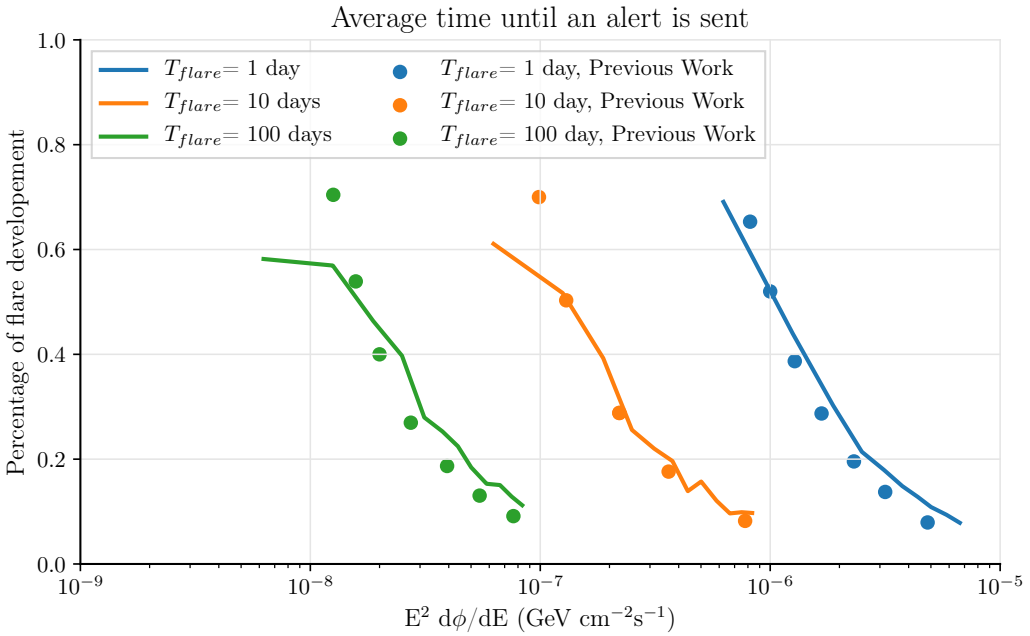

Figure 5.9: Average time after an alert is sent. This plot represents the amount of time the Time-Clustering algorithm needs to trigger an alert with respect to the total flare duration as a function of the flux. We show the results for a simulated source at $\delta = 30°$ for three different flare durations, a variable flux (i.e. a variable number of injected events) and a spectral index $\gamma = -2$.

This effect arises with very long flares (100 days, green line), it slightly modifies the behaviour of the curve for intermediate flare durations (10 days, orange line) and is negligible for short flares (1 day, blue line).

5.6 Historical Gamma-ray Follow-Up Alerts

The most recent results of the GFU analysis, obtained scanning approximately 8 years of IceCube data, from May 2011 to March 2019, are reported in [50]. The GFU alerts sent over the past year are only available starting from January 2019. In this section, we show the reproduction of the previous Gamma-ray Follow-Up (GFU) alerts and the best fit results for the source catalogue analysis. We compare the fit parameters and the significance of the alerts with the results stored in IceCube live catalogue and we compute the pre-trial and post-trial probabilities of the most significant flare recorded from all the monitored sources.

The pre-trial probability corresponds to the significance of the flare, evaluated from the value of the TS provided by the Time-Clustering algorithm, which performs the likelihood analysis multiple times over different combinations of events (further details are reported in Section 4.2.2). This introduces a bias in the evaluation of the significance of the fit. In fact, the more we analyse the signal coming from the monitored sources, i.e. the more trials we perform, the higher is the probability of obtaining an apparently statistically significant result produced by a background fluctuation. For this reason, the pre-trial probability needs to be corrected for trials. By construction, the tested time windows and combinations of events analysed by the Time-Clustering algorithm are highly correlated. This means that post-trial probability cannot be computed entirely analytically. The trials are evaluated performing simulations of background-only scrambled data over the fixed time scale of 1 year. Since the maximum duration of the tested time window for the Time-Clustering algorithm is 180 days, for time scales longer than one year, self-correlations vanish and we can therefore compute the additional trial corrections analytically [74].

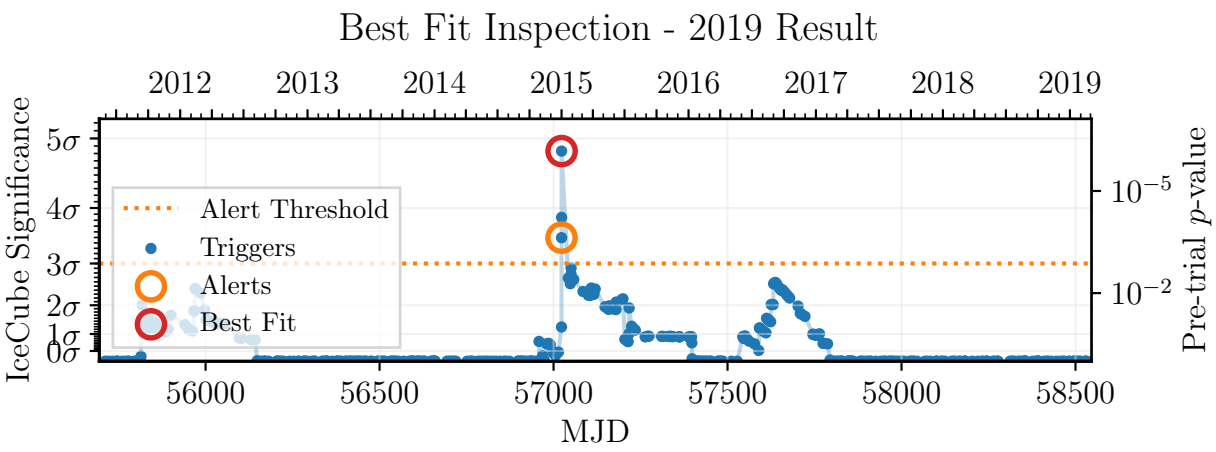

Figure 5.10: Best Fit result of the inspection of highest significance trigger for source catalogue analysis for data up to July 2019. The blue dots represent the triggers, the alerts are marked in orange and the best fit is marked in red. On the bottom horizontal axis MJD stands for Modified Julian Dates, a dating convention widely used in astronomy to facilitate chronological calculations [75].

Source Name	1ES 0347-121
Flare start	2014-12-31 20:32
Flare stop	2015-01-01 03:28
Flare duration	6.9 h
Flare uptime	5.4 h (77.8%)
Test Statistics Λ	31.77
Fitted n_s	3.93
Fitted γ	-2.47
Pre-trial p-value	$6.74 \cdot 10^{-7} (4.83\sigma)$
Post-trial p-value	$2.36 \cdot 10^{-2} (1.99\sigma)$

Table 5.1: Fit parameters and significance of the 2019 best fit result.

5.6.1 Reproduction of the 2019 GFU best fit result

As we mentioned in Section 4.2.3, the best fit of the source catalogue analysis corresponds to the output of the Time-Clustering Algorithm that leads to the highest significance flare. This means that we need to inspect all the triggers, also the muted ones. Here we show the neutrino curve of the best fit and we report both the pre-trial and post-trial probabilities.

The post-trial probability computed over 1 year of data needs to be corrected for the total number of monitored sources (which are, currently, 339) and for the number of years of data we use for our analysis.

In Figure 5.10 we show the 2019 result of the inspection for the highest significance trigger. In Table 5.1 we show the pre-trial and post-trial significance. The results we obtained are exactly the same as the ones reported in the previous work.

5.6.2 Reproduction of online alerts

In IceCube live catalogue the results of all the online alerts sent starting from January 2019 are stored. We ran the Time-Clustering algorithm on archival data scanning all the sources monitored for the Gamma-ray Follow-Up program reproducing the alerts.

Between January 2019 and November 2021, 53 GFU online alerts were sent.

Running the analysis offline we produced 61 alerts. This means that there are a number of alerts that weren't produced by the online real-time system. Moreover, we also noticed some minor differences in the p-value and in the fit parameters. In the following sections, we discuss the results obtained from the detailed study of those differences.

We classify the differences into three categories:

- Numerical Differences
- Coordinate Differences
- Missed Alerts

Numerical differences

The offline reproduction of GFU neutrino alerts is carried out using the same likelihood analysis, the same data and the same Test Statistics distributions used for the online analysis.

For 41 out of the 53 alerts stored in IceCube catalogue, we obtained the exact same results running the analysis online and offline. In 12 cases, instead, we notice minor differences in the significance of the alerts. The average difference in the $\log_{10}(p)$[1] between the online alerts and offline reconstructed ones is 0.02. Since those differences are small, of the order of 0.7%, they are probably due to different numerical approximations that arise when running the algorithms on different machines.

Coordinate differences

Some sources are monitored by more than one Čerenkov Telescope. During Summer 2021, two alerts were received from the source PKS 0420-01, monitored both by H.E.S.S. and MAGIC telescopes. The first of these two alerts was notified only to MAGIC telescope, and it wasn't communicated to H.E.S.S..

The GFU source catalogue analysis monitors 339 sources, and 128 of them are monitored by more than one Čerenkov telescope. The coordinates of the sources are defined in the source lists, and each Čerenkov telescope has its own source list. The coordinates are fixed and they are used to initialise the likelihood analysis.

When a source is monitored by more than one telescope, i.e. it is present in more than a source list, the analysis is run in parallel and independently for each partner telescope.

Some sources, including PKS 0420-01 source, present slightly different coordinates in different source lists. The differences are small, they are of the order of 0.006°, but they produce differences in the output of the likelihood analysis.

From January 2019, 12 alerts associated with 5 sources that present differences in the coordinates were sent, and all of them present differences both in the p-value and in the estimate of the number of signal events.

- The average difference in the $\log_{10}(p)$ is 0.05
- The average difference in the number of signals n_S is 0.05.

[1] Logarithm of the p-value

Also in this case the differences don't affect dramatically the output of the Time-Clustering algorithm, but they could possibly affect the production of an alert when the significance of the trigger is very close to the alert threshold.

The significance of the alert that was notified to MAGIC telescopes and not to H.E.S.S. was 3.03σ, and we believe that the H.E.S.S. alert was missed because of these coordinate differences.

Missed alerts

As we mentioned before, there are 53 alerts produced between January 2019 and November 2021 in IceCube catalogue, but running the analysis offline, we produced 61 alerts. This means that there is a number of alerts which is produced offline but not stored in the catalogue.

In particular, we found:

- 12 alerts that are produced running the analysis offline but they were not notified in real-time
- 4 alerts that are stored in the catalogue but they are not produced running the analysis offline

For what concerns the first case, these 12 alerts are all found to be produced during the summer of 2019 and January 2020. While from February 2020 we didn't miss any alert. The fact that those missed alerts are all produced in the same months suggests a malfunction in the infrastructure that produces the alerts. This hypothesis was confirmed by a member of the Real-time Oversight Committee, responsible for the maintenance of the real-time system.

The 4 alerts that are stored in the online catalogue but are not reproduced offline, instead, are all related to the MG1 J181841+0903 source and they were all produced between May 27$^{\text{th}}$ 2019 and June 5$^{\text{th}}$ 2019. There are actually 5 alerts produced for this source. The first one is the only one that we reconstruct by running the analysis offline, the other 4 are missed. This is probably due to the fact that the muting mechanism described in REF was implemented after the notification of these alerts. So, these 4 additional alerts are probably 4 triggers above the threshold received after the one that produced the first alert, that weren't muted yet.

Chapter 6

New Approaches to Increase the Signal-to-Noise Ratio

Due to the irreducible background and the low fluxes of astrophysical neutrinos, the detection of neutrino flares is particularly challenging. Additionally, to favour multi-messenger observations, we need to increase the coverage of electromagnetic data. For these reasons, IceCube Gamma-ray Follow-Up (GFU) alerts are released with a relatively low threshold on their significance and, as a consequence, they can be due to background fluctuations.

In this chapter, the development of new approaches to increase the purity of astrophysical alerts will be presented, focusing on increasing their signal-to-noise ratio. In particular, we will study the changes in the alerts when acting on the conditions the neutrino events need to fulfil to trigger the Time-Clustering algorithm. First of all, we will outline the typical characteristics of the GFU alerts discussing the signal-to-background weights of the events that contribute to the analysis, their energy and their distance from the source. Then we will discuss how and why rising the signal-to-background ratio of the events that trigger the Time-Clustering algorithm might help increase the purity of the alerts. Finally, we will reproduce the GFU analysis using different S/B thresholds and we will discuss the differences in the production of alerts and in their significance.

6.1 Typical Characteristics of the Alerts

Before trying new approaches for increasing the signal-to-noise ratio of GFU neutrino alerts, it is necessary to study the typical characteristics of the alerts produced using the current configuration of the analysis, described in Section 4.2.

The relevant parameters that were used to classify the alerts are:

- The weight of the events
- The distance of the events from the source
- The energy of the events

Moreover, we study the distribution of these quantities as a function of the significance of the alerts.

In Figure 6.1 we show the distribution of all the events that contributed to the GFU neutrino alerts received between January 2019 and November 2021 as a function of their distance from

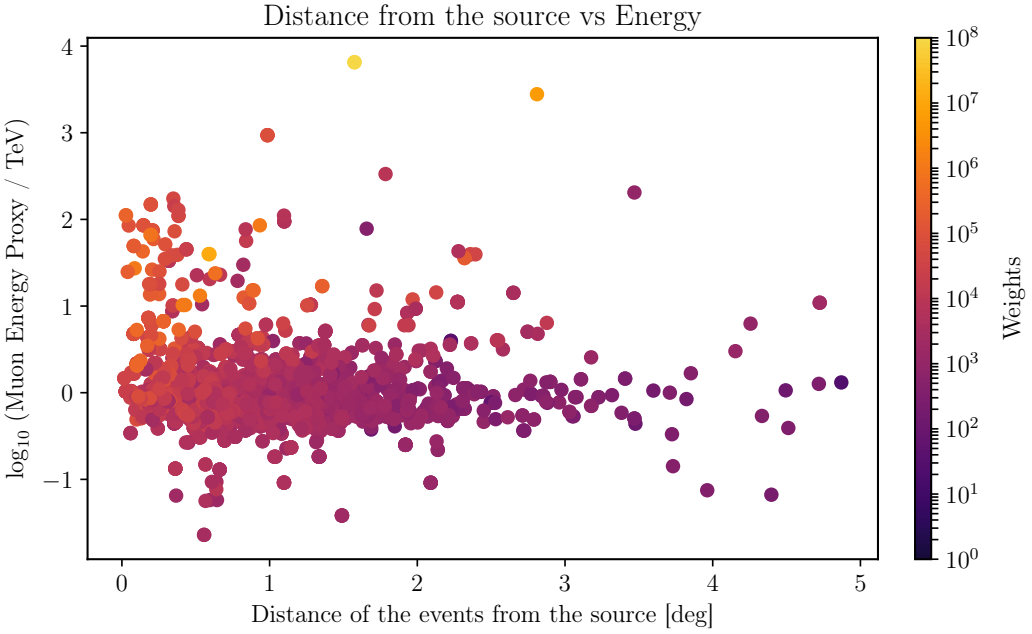

Figure 6.1: Distribution of the events that contributed to the GFU neutrino alerts received between January 2019 and November 2021 as a function of the distance of the events from the source and the reconstructed energy of the events. The colours represent the weights of the events.

the monitored source, the reconstructed energy and the weights. According to the spatial and energy probability density functions described in Section 4.2.1, the more an event is close to the monitored source, or the higher its energy, the higher its signal-to-noise ratio, i.e. its weight.

The majority of the events is detected in the vicinity of the source and they have an energy of the order of the TeV. We also notice a few events having particularly high energy. Those events could be a symptom of the presence of interesting neutrino flares and may deserve to be analysed in detail. However, only a small fraction of all the considered events present these characteristics.

The events displayed in Figure 6.1 are the ones that contribute with the highest weights to the likelihood fits that produce an alert. These events are published in the IceCube Live catalogue, thus they are already unblinded. Anyways, at this stage of the analysis, in order to avoid biases, we only study the overall distributions of these events without studying in detail the single events that contribute to the alerts.

In Figure 6.2 the distribution of the significance of the alerts as a function of the average distance of the events from the source is shown. We expect that the closer to the source the events are, the higher the significance of the alert. But we don't see any correlation between those quantities. This is probably a direct consequence of the fact that the signal-to-background (S/B) threshold used to trigger the analysis is currently set to a very low value and that we release alerts with a relatively low threshold on the significance. These choices affect the signal purity. In the next sections, we will discuss new approaches to increase the S/B ratio of the alerts and we will study how they affect the signal purity.

A relevant piece of information that needs to be taken into account when addressing the problem of the purity of the neutrino alerts has to do with the weights of the events. In Figure 6.1 and Figure 6.2 we can clearly observe that the great majority of the events that contribute to the alerts have a weight of the order of $\approx 10^2 - 10^3$, but the S/B threshold that triggers the analysis is currently set to 1. So, the triggers that produce the alerts are

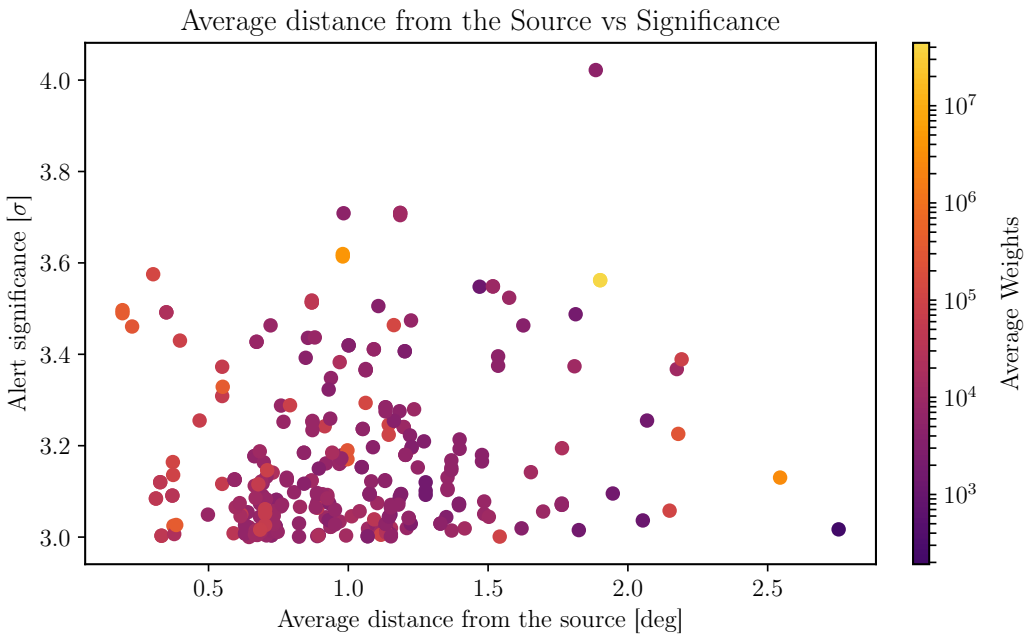

Figure 6.2: Distribution of the significance of the alerts as a function of the average distance of the events from the source. The colours represent the average weight of the events.

characterised by a S/B event weight of more than 2 orders of magnitude greater than the one used for triggering the analysis.

First of all, we need to understand how the weights of the events are calculated and how they are distributed. In Section 4.2.1 we introduced the signal S and background B probability density functions (4.19). The weight of an event is defined as:

$$S/B = \frac{P^S_{\text{energy}}(E|\vec{x},\gamma) \cdot P^S_{\text{spatial}}(\vec{x}|\vec{x_{src}},\sigma)}{P^B_{\text{energy}}(E|\vec{x}) \cdot P^B_{\text{spatial}}(\vec{x})} \tag{6.1}$$

So it has a spatial and an energy component.

In Figure 6.3 we show the distribution of the weights of the events both in the GFU sample and in the simulated sample. To preserve blindness, we show only 10% of the events of the GFU sample, chosen randomly in time and coordinates. For comparison, we show also the distribution of the weights of the simulated background sample. Being a simulated sample, we don't need to use a blind approach, thus we display the distribution of all the events of the data set. We can see that the events are distributed over the same weight range, but the events of the simulated background sample have a broader energy weight distribution. This is due to the fact that by displaying the whole distribution of the events, we observe more background fluctuations, i.e. high energy events that emerge from the background. The major contribution to the total weight of the alerts is given by the spatial component, which ranges from ≈ 0 up to 10^8. The energy component, instead, is of the order of a few units for a background-only scenario, and it increases with increasing energy. The colour code represents the total weight. We can notice that a significant amount of events have a S/B ratio greater than one. In Table 6.1 we show the percentage of events above the threshold for different S/B ratios.

Since a significant amount of events have a S/B ratio greater than one, we run simulations using higher thresholds and we study how this affects the production of alerts. We will focus, in particular, on the study of the rate and the significance of alerts.

S/B ratio	Events above threshold
1	46%
10	39%
100	28%
1000	8.0%
5000	1.5%
10000	0.6%

Table 6.1: Fraction of events that are considered for the likelihood analysis having a S/B ratio greater than a certain threshold value.

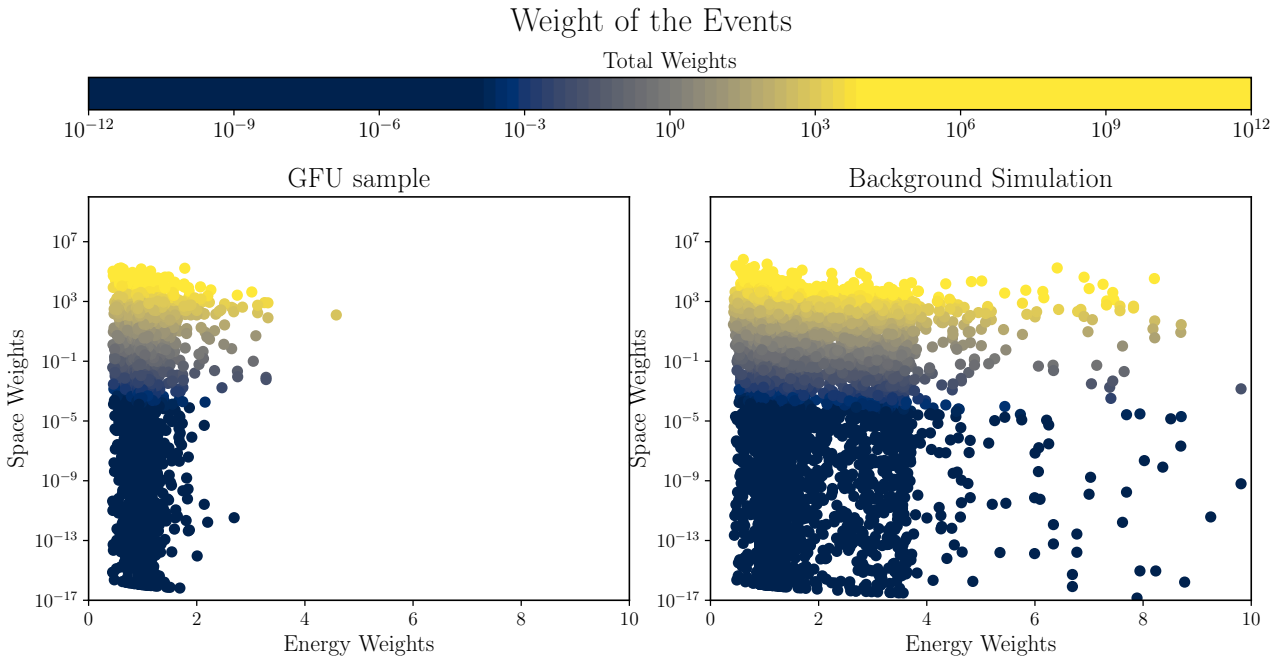

Figure 6.3: Distribution of the weights of the events that contribute to the likelihood analysis in the GFU sample (left) and, for comparison, in the simulated background sample (right). To preserve blindness, we show only 10% of the events of the GFU sample, the displayed events are randomly sampled from the entire data set. The colour code represents the total weight of the events, the blue dots are the ones that are under the S/B = 1 threshold and the yellow ones represent the events that are above the current threshold.

6.2 Increasing the Signal-to-Noise Ratio of the Neutrino Events

As explained in Section 4.2.2, the Time-Clustering algorithm, in the current configuration, is triggered whenever an event with a signal-to-noise ratio greater than one is detected. The approach we use to increase the signal-to-background of the alerts consists in rising the minimum S/B threshold that the events need to have to trigger the Time-Clustering algorithm. This reduces the number of generated triggers, it impacts the Test Statistics distribution and, as a consequence, the calculation of the p-value of the alerts.

In this section, we compare the results obtained keeping S/B = 1 with the ones obtained rising the threshold. The threshold values we test are the ones reported in Table 6.1.

We simulate neutrino flares of different duration injecting a different number of events and we test the reconstruction of the fit parameters, the alert rate and the significance of alerts.

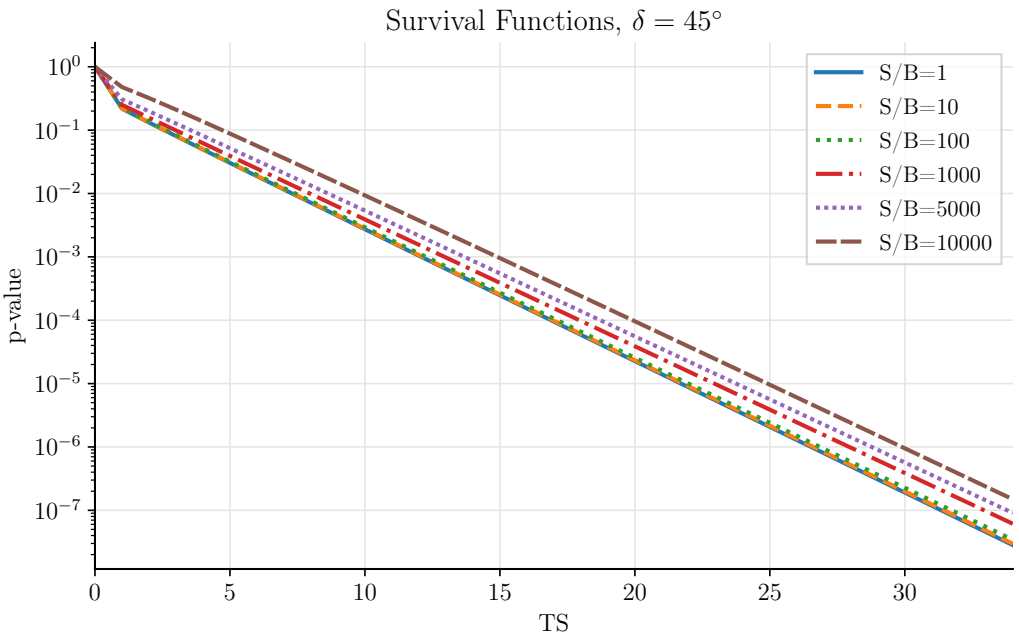

Figure 6.4: Survival Function for different values of the S/B ratio used to trigger the Time-Clustering algorithm for the source catalogue analysis performed for a simulated source at $\delta = 45°$.

6.2.1 Survival function and p-value maps

The significance of the alerts is evaluated from the Test Statistic Statistics distributions obtained from simulations. In particular, the survival functions are calculated for 40 different values over the whole declination range and stored in JSON files [76].

Rising the S/B ratio used to trigger the Time-Clustering algorithm affects the output of the algorithm and, as a consequence, the Test Statistics distributions. This means that the survival functions change.

In Figure 6.4 we show the survival functions for different values of the S/B ratio for the Time-Clustering algorithm applied to the source catalogue analysis for a source at a declination of $\delta = 45°$. We can clearly see that survival functions for S/B ratios of 1, 10 and 100 present extremely small differences, they are almost overlapping. Significant differences start to arise with a S/B ratio of 1000, and the differences increase at higher thresholds.

This is in agreement with what we noticed in the previous section. Since the average weight of the events that contribute to the alerts is around 10^3, this is the S/B ratio value for which we start observing differences in the output of the algorithm.

6.2.2 Time-Clustering algorithm trigger rate

While operating on the S/B threshold that triggers the analysis, we should also take care of the rate of the triggers. Despite our goal is to increase the purity of astrophysical alerts, we need also to set up the analysis in such a way that we are able to frequently perform a time scan of the signals coming from the monitored sources.

In Figure 6.5 we show the distribution of the rate of triggers for all the different S/B ratios over all the declinations. For S/B ratios up to 1000, we can see that, as expected, the rate is lower in the Southern Sky ($\delta < 0°$) and higher in the Northern Sky ($\delta > 0°$), with a peak at the horizon, where we have the best sensitivity. For very high S/B ratios, instead, not only the rate drastically decreases, but also the structures change. The rates displayed in Figure

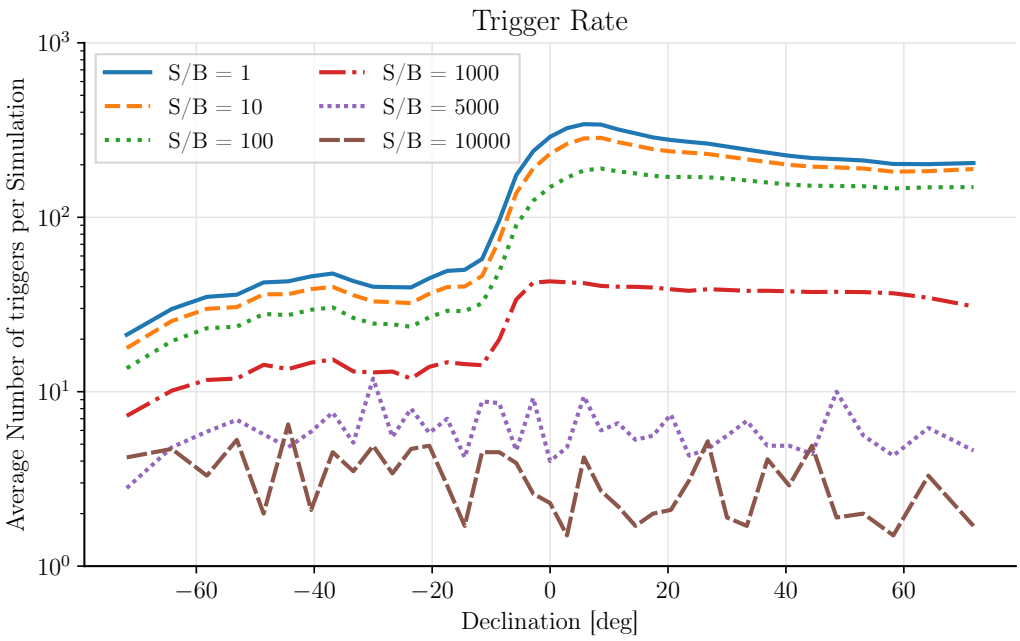

Figure 6.5: Rate of the triggers analysed by the Time-Clustering algorithm for simulations performed over 1 year of scrambled background for different S/B ratios.

6.5 refer to background simulations performed over one year of scrambled background.

In Figure 6.6 we show the temporal evolution of the triggers related to simulated flares of different lengths and intensities for all the tested S/B ratios. In order to give an idea of the simulated flares, we also display the injected events. We can see that, in all the cases, the alert threshold is overcome in correspondence of the simulated signal events. Following the expectations, the Time-Clustering algorithm produces fewer triggers at very high S/B ratios, but, in all the tested cases, it produces approximately the same results.

We can notice that for S/B ratios up to 1000, the temporal evolutions of the triggers are very well overlapped. For higher S/B thresholds, instead, the trigger rate decreases and, in some cases, they don't cover the whole scanned time period. For example, both in the case of 100 days flare with 4 events and 20 events, the S/B = 10000 triggers stop well before the end of the scanned time window.

For short and weak flares, i.e. 1 day flare with 2 events, the flare was recognised in all the tested cases apart from S/B = 10000. In fact, the neutrino curve that corresponds to this threshold is close to 0. Also in the case of a 100 days flare with 4 injected events the Time-Clustering algorithm fails in recognising the flare when using S/B = 10000. However, we can see that the injected events, displayed in red in Figure 6.6, have S/B $>$ 10000, meaning that they satisfy the trigger condition for the Time-Clustering algorithm. On the other hand, the Time-Clustering algorithm requires the presence of at least two events that satisfy this condition, so that it is possible to define the time window in which the likelihood fit is performed. Since no alerts were produced, the Time-Clustering algorithm probably didn't manage to converge or it didn't find any other event that overcame the S/B threshold to define the analysed time window. This means that the algorithm may be inefficient in identifying weak flares at high S/B thresholds. This issue will be discussed in the next sections (see 6.2.4).

Despite the Time-Clustering algorithm produced approximately the same results in most of the tested cases, with very high S/B thresholds we lose our capability of following efficiently the temporal evolution of the triggers and producing alerts in correspondence of simulated

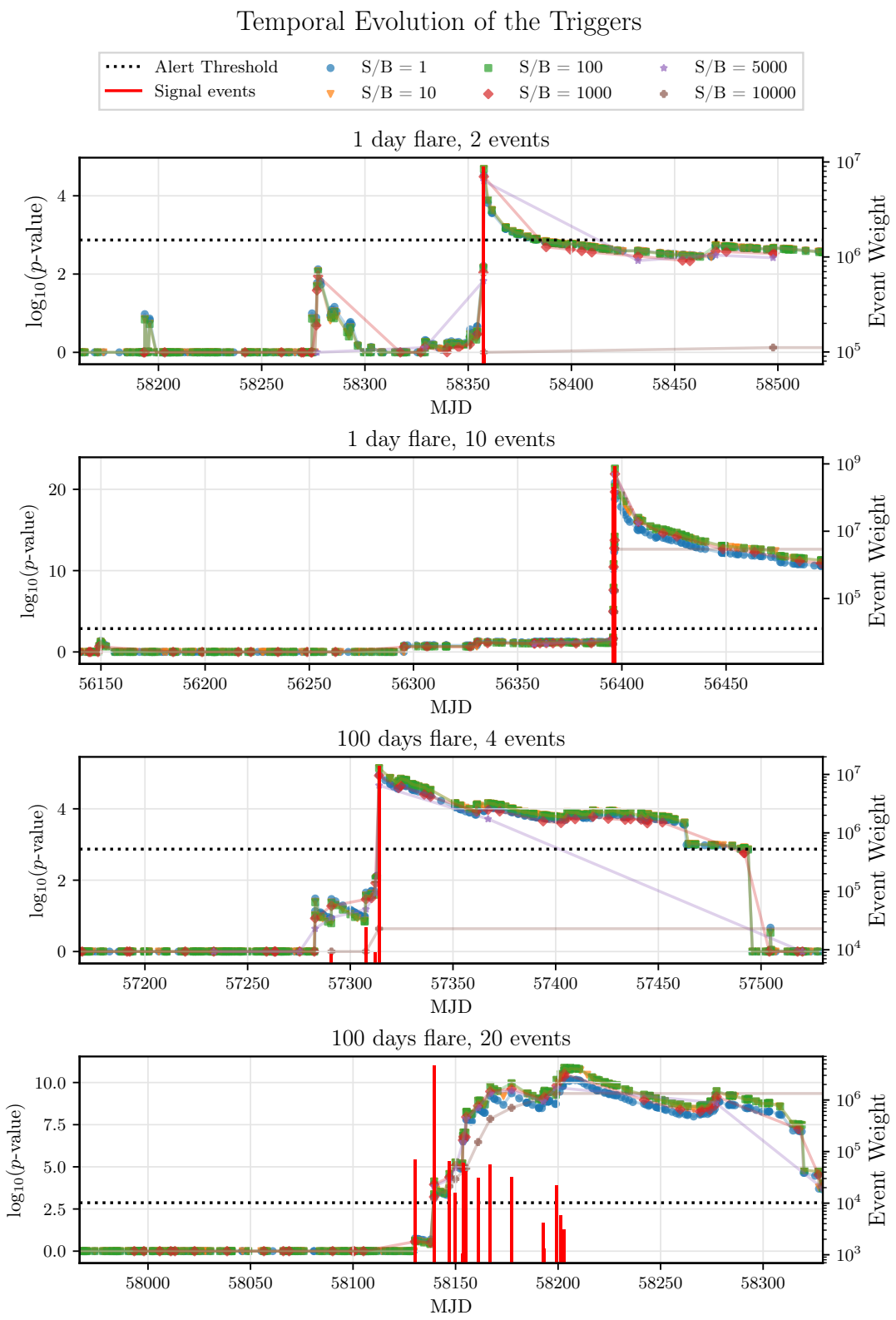

Figure 6.6: Temporal evolution of the triggers for different simulated flares over 1 year of data (365 MJD) for all the tested S/B ratios. The red bars represent the events that contributed to the best fit flare, in the right vertical axis their weight is displayed. For short flares (1 day, i.e. 1 MJD) the bars are very close, thus they overlap. MJD stands for Modified Julian Dates [75].

flares. This is due to the drastic decrease of the trigger rate displayed in Figure 6.5.

Together with the trigger rate, also the CPU time decreases with an increasing S/B threshold.

S/B ratio	Relative CPU time		
	Southern Sky	Horizon	Northern Sky
10	88%	85%	81%
100	53%	32%	42%
1000	49%	3.8%	3.2%
5000	55%	2.4%	1.9%
10000	58%	2.3%	1.8%

Table 6.2: CPU time needed to run a background simulation of 1000 trials for each tested S/B ratio in three different regions of the sky. The percentages are calculated with respect to the S/B = 1 case.

In Table 6.2 we report the average CPU time necessary to run a background simulation of 1000 trials in the IceCube computing cluster in three different regions of the sky for all the tested S/B ratios. The values are reported as the percentage of time needed to complete the simulations with respect to the S/B = 1 case. The CPU time scales proportionally to the trigger rate, the fewer are the triggers, the faster is the algorithm. This explains the difference in the time gain between the Northern and the Southern Sky. In the Southern Sky, where the event rate is lower (see Figure 6.5) and, as a consequence, the analysis is faster, the CPU time doesn't decrease as much as in the Northern Sky.

Additionally, since the percentage of time needed to complete a simulation is approximately constant in the Southern Sky for S/B $>$ 100, this suggests that the Time-Clustering algorithm in these cases reaches its maximum performance, thus it is not possible to further diminish the CPU time acting on the S/B ratio that triggers the analysis. The same happens in the Northern Sky and at the horizon for very high values of the S/B ratio.

6.2.3 Reconstruction of flare parameters

One of the most important points of this analysis has to do with the performances of the Time-Clustering algorithm. In fact, before studying how changing the S/B ratio affects the production of alerts, we need to be sure that the Time-Clustering algorithm still manages to properly reconstruct the characteristics of the flares when operating on the S/B ratio that triggers the analysis.

We run simulations for all the values of the S/B ratios displayed in Table 6.1. The simulated flares are characterised by a spectral index $\gamma = -2$, the number of injected events that range from 2 to 20 events, and three different flare durations: 1 day, 10 days and 100 days.

We test the performances of the algorithm simulating sources both in the Northern and in the Southern Sky, $\delta = 30^\circ$ and $\delta = -30^\circ$ respectively. The results for S/B = 1 are discussed in the previous chapter (see Figure 5.7), in Figure 6.7 we show an example of the reconstruction of the number of signal events for two of the tested S/B ratios. For S/B = 10 the convergence of the number of injected signal events is still good, while, for S/B = 10000, instead, we observe an underestimation of the number of injected events, meaning that the algorithm loses efficiency at high S/B thresholds.

The spectral index and the duration of the flare are always properly reconstructed by the Time-Clustering algorithm. For very high S/B ratios we observe some irregularities for a low number of injected events. This is due to the fact that the trigger rate with these thresholds is extremely low and thus we suffer statistical fluctuations due to low statistics. In Appendix A.1 we report all the plots concerning the test of the reconstruction of the fit

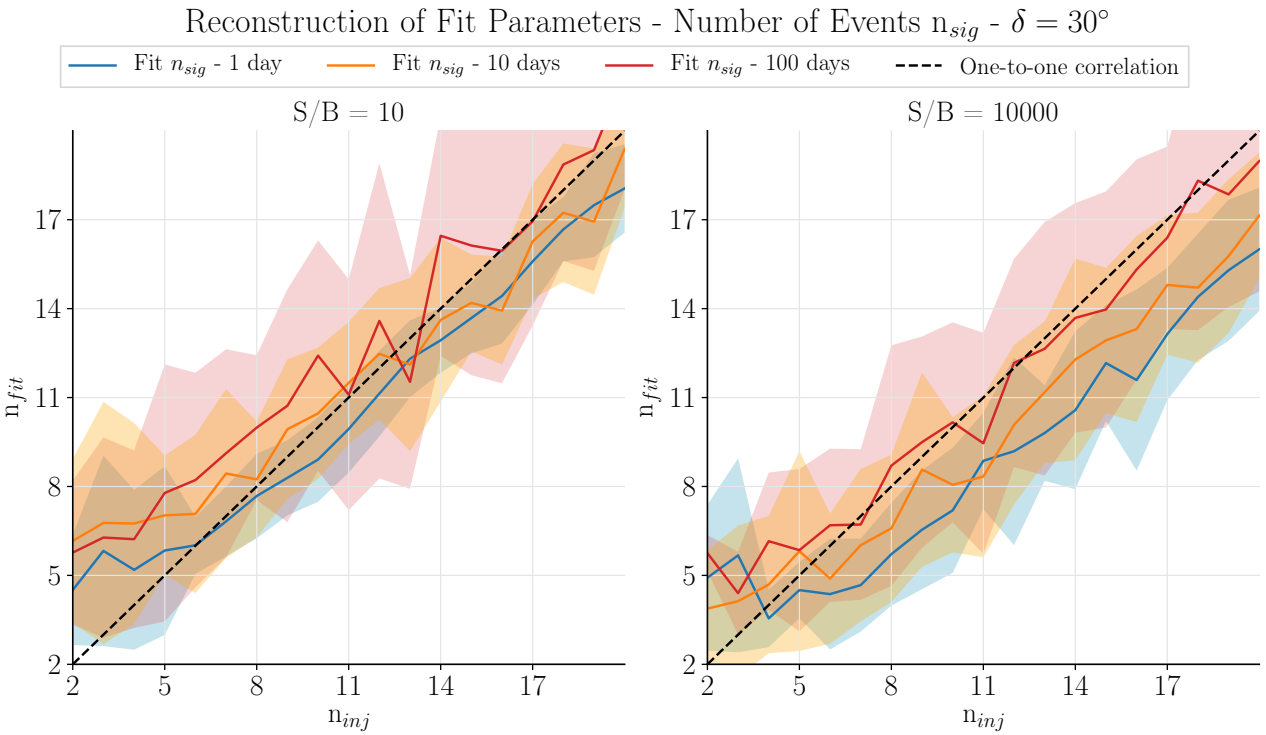

Figure 6.7: Example of reconstruction of fit parameters for simulations performed with two different S/B ratios. In particular, here we show the estimate of the number of signal events that contribute to the flare as a function of the simulated value for flares having three different durations and spectral index equal to $\gamma = -2$.

S/B ratio	Percentage of Failed fits
1	4.3%
10	3.8%
100	3.1%
1000	3.1%
5000	3.5%
10000	4.1%

Table 6.3: Fraction of failed fits in the analysis for the reconstruction of fit parameters.

parameters.

The results displayed in Figure 6.7 and all the other results stored in the appendix don't correspond to the entire sample of simulated flares. In fact, especially when rising the threshold, the likelihood fit minimizer does not converge, thus a maximum is not found. The displayed data only correspond to the physical and consistent outputs of the Time-Clustering algorithm.

The reason why the likelihood fit sometimes fails providing negative Test Statistics values and non-physical estimates of the fit parameters goes beyond the scope of this work, but, to give an idea of the presented results, in Table 6.3 we provide an estimate of the percentage of failed fits per each tested S/B ratio. The percentage of failed fits is approximately constant and relatively low. By the way, this low amount of failed fits still affect the reconstruction of the fit parameters. In fact, the Monte Carlo simulated files contain 475 trials each, 25 for each different number of injected events (from 2 to 20 events). On average, we have therefore one failed fit for each different simulated flare. Since the values of the failed fits are completely

non-physical and far from the expectations, one single failed fit strongly affects the outcome of the analysis, and thus were here rejected.

Nevertheless, the algorithm still succeeds in properly reconstructing the simulated flares in the majority of the examined cases. In fact, the overall result is always compatible with the true injected value and the convergence follows the same behaviour that we observe at lower thresholds and that has been already discussed in 5.4.2.

6.2.4 Effects on the typical characteristics of the alerts

In this section, we will discuss how the typical characteristics of the alerts are affected by changing the S/B threshold.

In order to do this, we need to reproduce the distribution of the events that we already displayed for the real data in Figure 6.1 for all the tested S/B ratios. Moreover, to guarantee a consistent study of the changes in the alert production caused by rising the S/B ratio, it will be necessary to distinguish between short and long flares and more intense and less intense flares. In Figure 6.8 we report, as a reference, the results for only two declinations, one in the Southern Sky and one in the Northern Sky and we compare the distributions of the events for two of the tested S/B ratios.

We can clearly notice that, in both cases, the distribution of the events that contribute to the alerts doesn't change increasing the S/B ratio: the events have approximately the same energies, the weights of the events are always of the order of 10^3 and they are mostly localised near the observed source. This indicates that, despite the trigger rate drastically decreases, the Time-Clustering algorithm still manages to produce alerts characterised by events having the same properties of the ones produced with lower thresholds. This means that by rising the S/B ratio we don't lose any information regarding the events that contribute to the alerts.

We also notice that, in the Southern Sky, the average energy of the events is approximately one order of magnitude greater than the ones that contribute to the alerts coming from sources in the Northern Sky. This is due to the fact that the BDT cuts applied to the MuEX energy estimates of the single muon tracks are set to 10 GeV in the Northern Sky, and to 316 GeV in the Southern Sky [50]. Tighter cuts are necessary in the Southern Sky because of the irreducible atmospheric background. The event distributions displayed in Figure 6.8 are compatible with the above-mentioned cuts.

Moreover, the simulations at $\delta = 30^\circ$ show that also the angular distribution of the events in the Northern Sky is broader than the one in the Southern Sky. This effect can still be imputed to the atmospheric background. In the Northern sky, the atmospheric background is suppressed and we can put less stringent constraints on the arrival direction of the events.

In Figure 6.9 we show the distribution of the average significance of the alerts as a function of the average distance of the events from the simulated sources for the same cases we just considered for the distribution of the events. The colour code represents the average weight of the events that contribute to the alerts. As we already observed in Figure 6.2, in both cases there is no evidence of any correlation between the significance of an alert and the distance of the events from the source; and rising the S/B ratio doesn't produce any clear difference in the distributions of these quantities.

We notice there is an accumulation of alerts whose events have an average distance from the source of about 0.5° in the Southern Sky, and around 1° in the Northern Sky. The reason why, the events are, on average, closer to the position of the source in the Southern Sky than

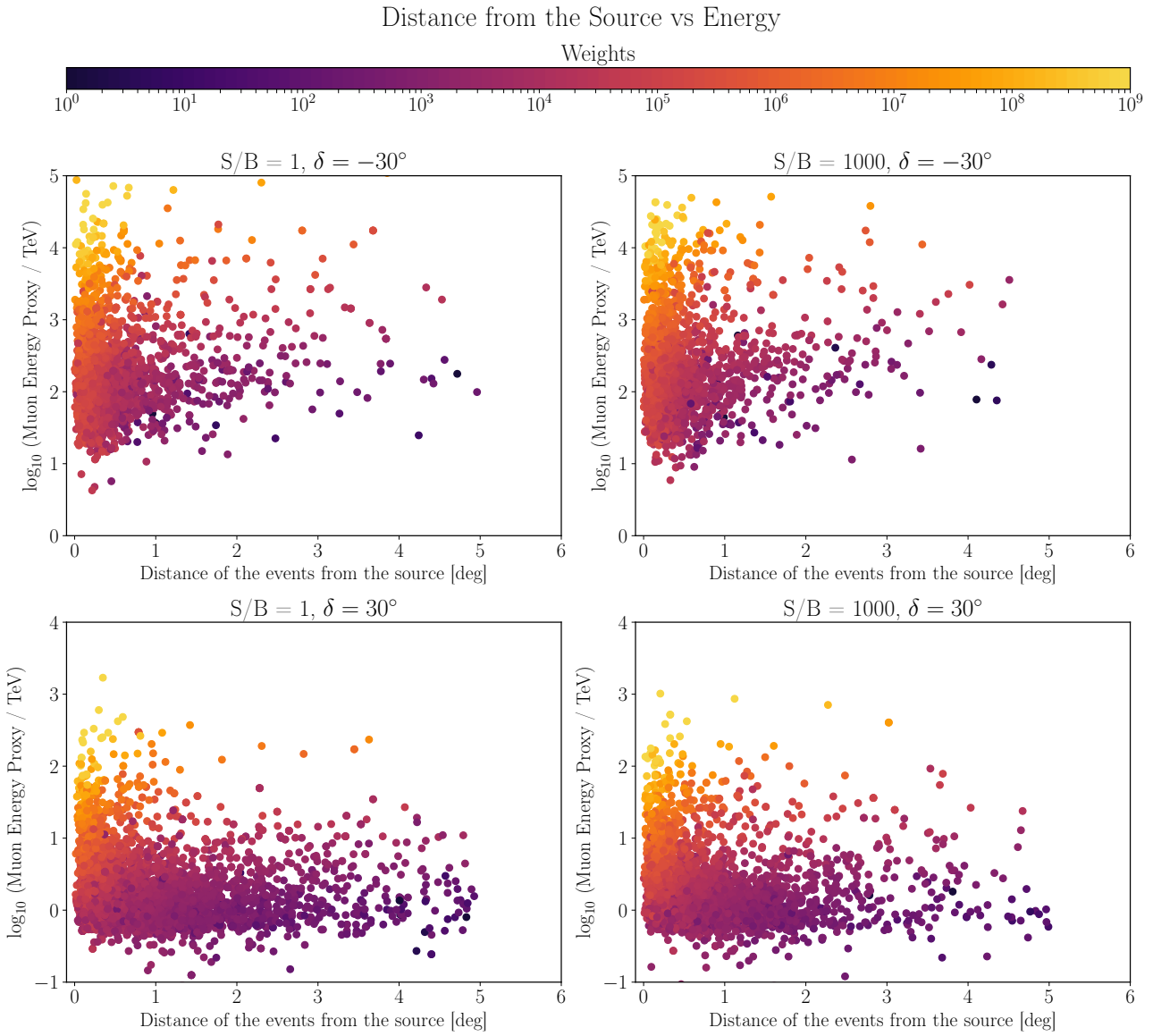

Figure 6.8: Distribution of the events that contribute to the alerts for two different declinations and two different S/B ratios.

in the Northern Sky is, once again, related to the different treatment of data coming from the two hemispheres.

A remarkable result about the alert production when rising the S/B ratio concerns the number of alerts. As we mentioned before (Section 6.2.2), the trigger rate drastically decreases when rising the trigger threshold. At the same time, the number of produced alerts doesn't decrease as much as the number of triggers, and also the number of events that contribute to the alerts doesn't decrease as much as the trigger rate (see Table 6.4).

Taking a closer look at the alert production, we study separately the characteristics and the rate of the alerts when rising the S/B threshold with respect to the signal strength and the duration of the flares. We distinguish between *faint* fluxes, characterised by a low number of injected events, *intermediate* fluxes and *strong* fluxes, characterised by a large number of injected signal events. Results are shown in Table 6.4.

A difference in the alert rate between the Northern and the Southern sky can be observed, especially for intermediate and strong fluxes. While in the Northern Sky the number of

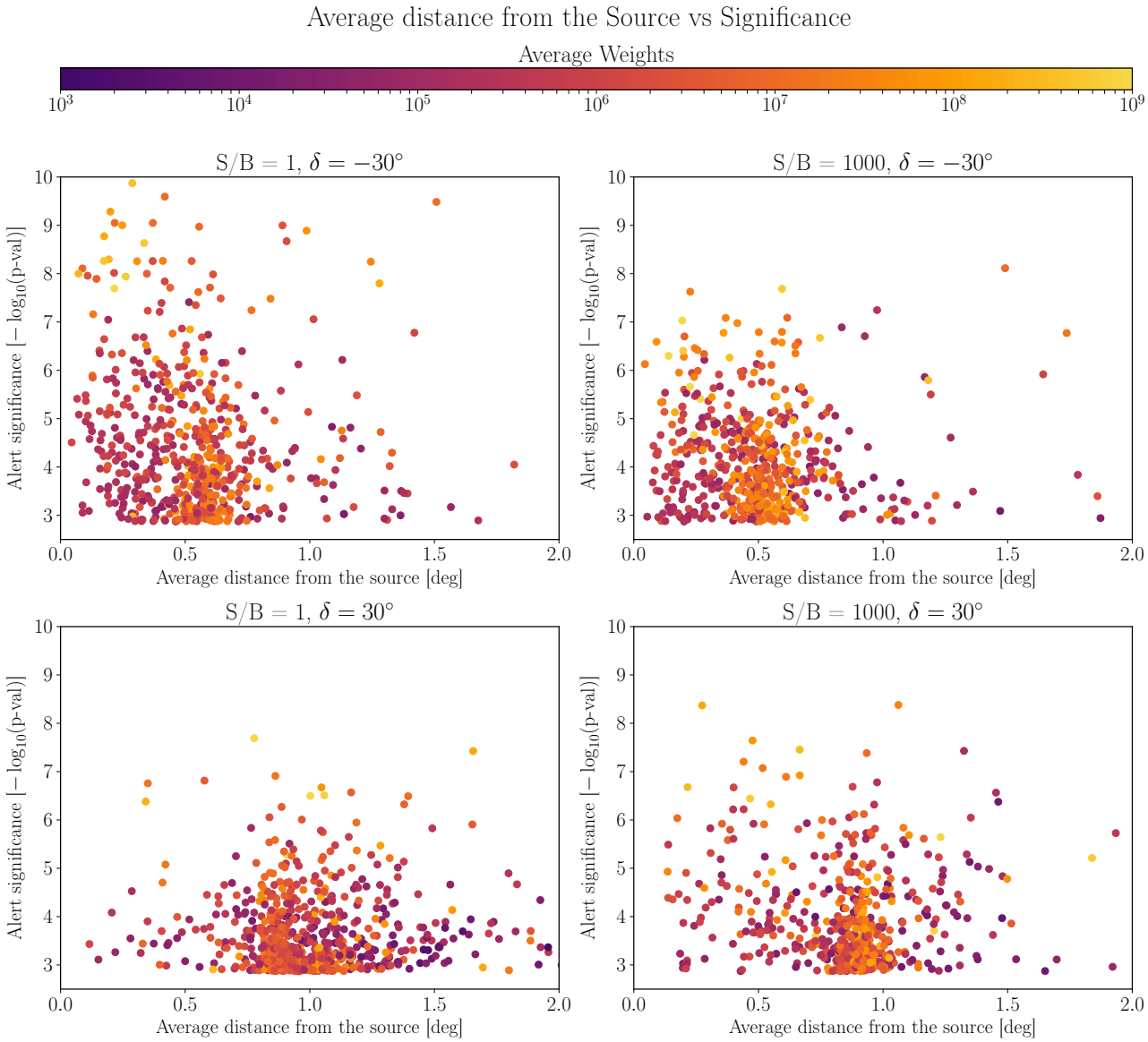

Figure 6.9: Distribution of the significance of the alerts as a function of the average distance of the events form the source for two different declinations and two different S/B ratios.

alerts decreases by approximately 20% when rising the threshold, in the Southern Sky it is approximately constant. For faint fluxes, instead, we observe a significant loss of alerts at high thresholds. As expected, fainter fluxes are mostly affected by rising the S/B threshold.

In observing this loss we have to pay particular attention to the number of simulated MonteCarlo maps. We simulate one flare per map, our results show that in the Northern Sky, for low S/B thresholds and intermediate and strong fluxes, the number of alerts is higher than the number of maps, meaning that the Time-Clustering algorithm finds more than one alert per map. In fact, especially for long flares and strong signals, there might be fluctuations in the temporal evolution of the triggers along the flare causing the significance level of the triggers to drop below the 3σ threshold and then overcome it again during the flare window. Rising the threshold, this effect is mitigated. However, the algorithm still manages to identify, on average, at least one alert for each reconstructed flare, i.e. the number of alerts is approximately equal to the number of maps.

In the Southern Sky, instead, this doesn't happen. The number of alerts is always close to the number of total injected flares. We don't observe the same effect we find in the Northern

Number of Alerts

S/B ratio	$\delta = 30^\circ$				$\delta = -30^\circ$			
	Bkg	Faint	Intermediate	Strong	Bkg	Faint	Intermediate	Strong
1	25	60	286	275	42	97	245	247
10	26	43	293	275	40	83	250	244
100	32	73	302	274	33	81	248	245
1000	16	42	247	246	13	93	241	249
5000	8	36	235	244	4	70	240	240
10000	≈ 2	15	233	240	≈ 0	53	240	242
# MC sim	200	120	240	240	200	120	240	240

Table 6.4: Number of alerts generated by the Time-Clustering algorithm for two different declinations, three different intensities and the background. The terms in the second rows refer to the characteristics of the injected flares. Bkg stands for background and it means there is no injected flare, faint refers to a low number of injected events (2 or 3 events), strong is assigned to flares that are characterised by an high number of events (more than 17 events) and intermediate corresponds to a flux in between what we call faint and what we consider strong (from 9 to 12 events). In the last row we reported the total number of performed trials.

Sky. This means that the different reconstruction of events and the different trigger rate in the two hemispheres affects the production of alerts. Nevertheless, the fact that we still manage to reconstruct a number of alerts approximately equal to the number of injected flares confirms that the Time-Clustering algorithm manages to recognise interesting flares coming from both hemispheres, despite the atmospheric background in the Southern Sky.

For small signal strengths, instead, we can see that we often fail in recognising the simulated flares. In fact, the number of alerts is always smaller than the number of MonteCarlo maps. This is probably due to the fact that faint signals may be below our sensitivity, thus we are not able to distinguish them. In this case, not only the Time-Clustering algorithm doesn't manage to reconstruct all the injected flares, but faint flares are the only ones for which we observe a drastic decrease in the number of alerts at increasing S/B thresholds, meaning that the algorithm is inefficient at low signal strengths. Additionally, we notice that, for small signal strengths, we generate more alerts in the Southern Sky than in the Northern Sky. This suggests that the better directional reconstruction of down-going tracks favours the production of alerts, making the algorithm more efficient for sources in the Southern Sky in the case of faint flares.

The background alert rate is drastically suppressed when rising the S/B threshold, this is compatible with what we already discussed previously. Since the trigger rate decreases, the probability of finding a background fluctuation over the threshold decreases too. This is a direct consequence of the way the Time-Clustering algorithm works. To run the likelihood analysis we need at least two events above the S/B threshold, and at very high S/B thresholds the number of events that can satisfy this condition is very small (see Figure 6.5). The fact that at such high thresholds we are able to identify simulated alerts but not to produce background alerts could suggest that rising the S/B threshold allows to increase the purity of GFU alerts. On the other hand, also the rate of alerts related to faint fluxes decreases, meaning that the algorithm has worse performances.

The quantities reported in Table 6.4 refer to different durations (1 day, 10 days, 100 days), but no relevant difference is observed for the tested cases. Further information about the detailed study of alerts produced in different conditions can be found in Appendix A.1.

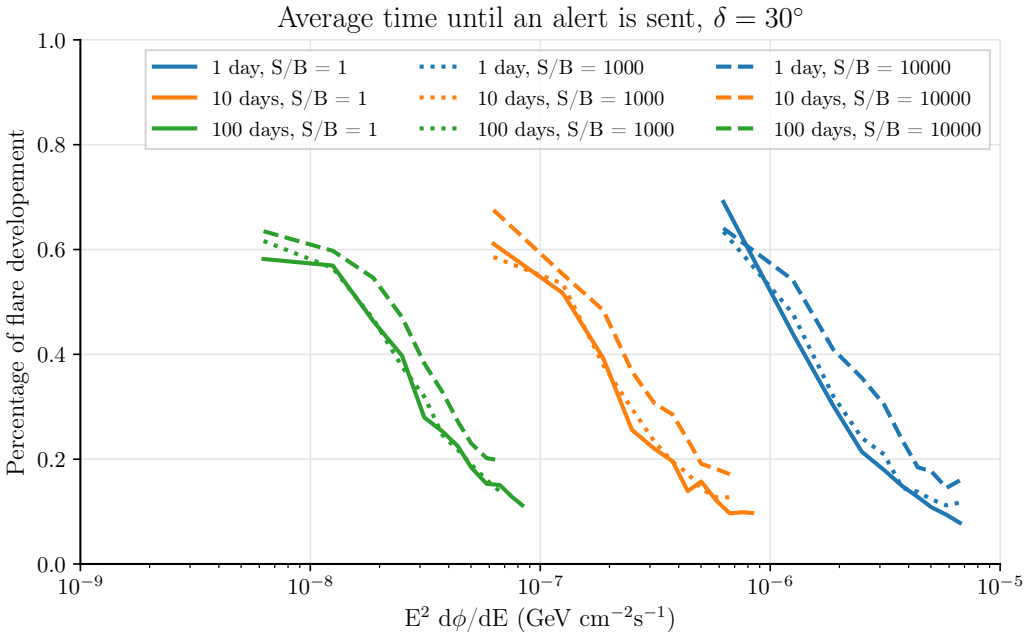

Figure 6.10: Average time necessary to trigger an alert for a source located in the Northern Sky ($\delta = 30°$) for three different flare durations as a function of the injected flux. We show the results for three different S/B ratios: 1, 1000 and 10000.

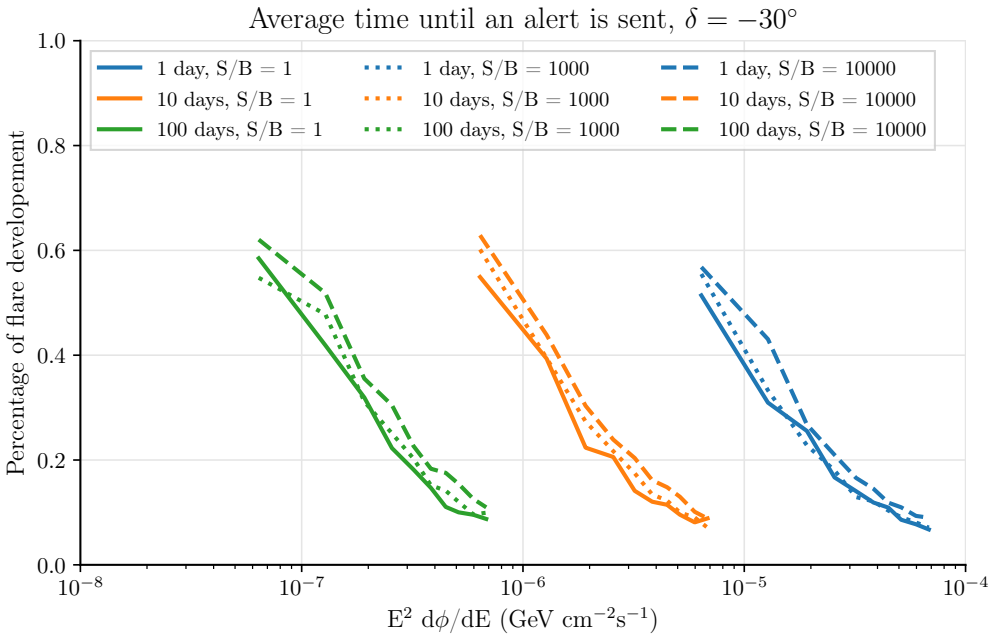

Figure 6.11: Average time necessary to trigger an alert for a source located in the Southern Sky ($\delta = -30°$) for three different flare durations as a function of the injected flux. We show the results for three different S/B ratios: 1, 1000 and 10000.

6.2.5 Time after an alert is sent

One last consideration about the consequences of rising the S/B ratio of the Time-Clustering algorithm concerns the time that the algorithm needs to produce a trigger that overcomes the 3σ threshold and transmits an alert.

In Figure 6.10 and 6.11 we show the results for $\delta = 30°$ and $\delta = -30°$ respectively. We display only the results for only three of the tested S/B ratios because the relevant differences in this quantity start to arise with S/B > 1000. The trigger rate decreases as we rise the

S/B ratio (see Section 6.2.2), thus we lose information about the temporal evolution of the triggers. As a consequence, for flares having the same characteristics, the Time-Clustering algorithm takes more time to generate a trigger over the threshold for high S/B ratios. This means that, for real-time analyses, where we want to be as fast as possible in obtaining information about interesting neutrino flares, low S/B ratios have a better performance than higher ones.

We also notice that, in the Southern Sky, the alerts are triggered, on average, earlier than in the Northern Sky. This is due to the fact that, since the trigger rate is lower in this region of the Sky, the algorithm is faster. This may seem in contrast with the fact that the time needed to trigger an alert increases at increasing S/B thresholds, i.e. at decreasing rates. However, when changing the S/B ratio, we have to take into account that also the Test Statistics distributions and the p-value maps change, and this also impacts the production of the alerts. In fact, since the higher is the S/B ratio the higher is the frequency of high values of the TS (see Figure 6.4), the 3σ threshold will be overcome, on average, at higher TS values when rising the S/B ratio. The direct consequence of this fact is that the Time-Clustering algorithm will take more time to trigger an alert. As we can see, this effect is mitigated in the Southern Sky, where the three curves don't differ as much as in the Northern Sky, but this is due to the different characteristics of the data coming from the two hemispheres.

One final consideration has to do with the fact that in the southern Sky we don't observe the same saturation behaviour we see in the Northern Sky for low fluxes and that we already commented in Section 5.5. This is probably due to the different efficiency of the Time-Clustering algorithm in the two hemispheres. We just mentioned that, despite being affected by the irreducible atmospheric background, at small signal strengths the Time-Clustering algorithm seems to have better performances in Southern Sky. In the Northern Sky, instead, the high trigger and the consequent high number of background fluctuations affect the identification of very faint flares and, as a consequence, the time needed for the Time-Clustering algorithm to trigger an alert in the case of faint fluxes.

6.2.6 Efficiency of the analysis

To conclude this chapter, in Figure 6.12 and 6.13 we show the efficiency of the Time-Clustering algorithm as a function of the injected signal strength for sources located both in the Northern and Southern Sky.

The efficiency is calculated as a ratio between the number of MonteCarlo simulations we performed injecting flares with different signal strengths and the number of alerts. A 100% efficiency corresponds to the case in which we generate on average one alert per map, i.e. as many alerts as the number of simulated maps.

As we already mentioned in Section 6.2.4, for low signal strengths the algorithm is not efficient, and the efficiency decreases at increasing thresholds, dropping below 20% in the Northern Sky and 30% in the Southern Sky. However, from intermediate signal strengths ($\approx 6 \sim 7$ injected events), the algorithm reaches efficiencies close to 100% for all the tested S/B ratios. Additionally, we notice better performances for sources located in the Southern sky, indicating that the better angular reconstruction of down-going tracks could improve the significance of the alerts.

Despite the Time-Clustering algorithm seems to recover all the injected flares at all the tested thresholds for sufficiently strong signals, we also need to take into account that we observe an inefficiency in the reconstruction of the flare parameters for high S/B thresholds. We

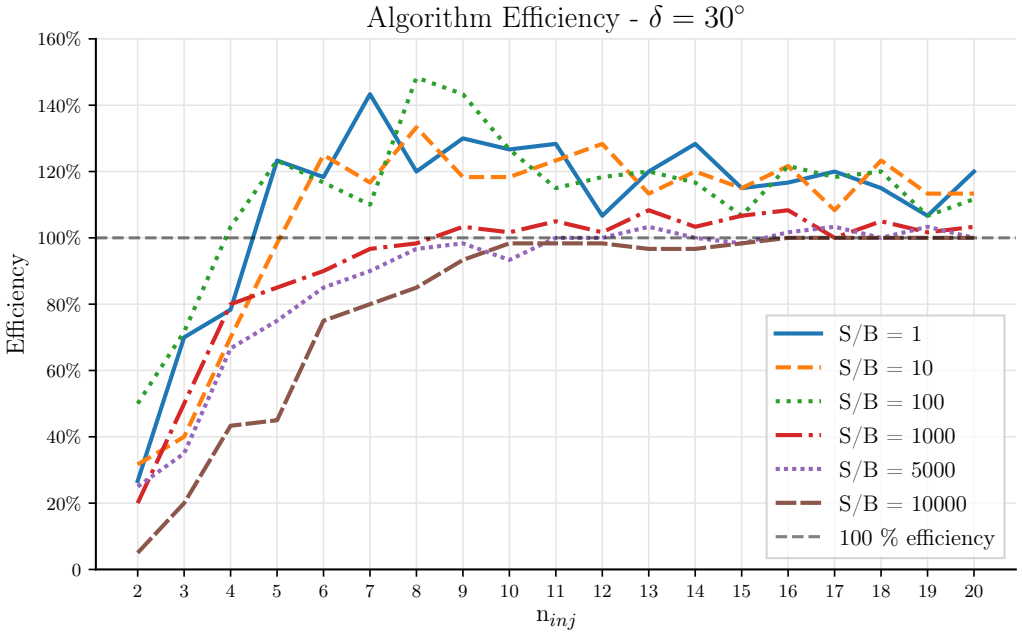

Figure 6.12: Efficiency of the Time-Clustering algorithm as a function of the injected signal for a source in the Northern Sky ($\delta = 30°$). The efficiency represents the number of produced alerts with respect to the total number of MonteCarlo maps.

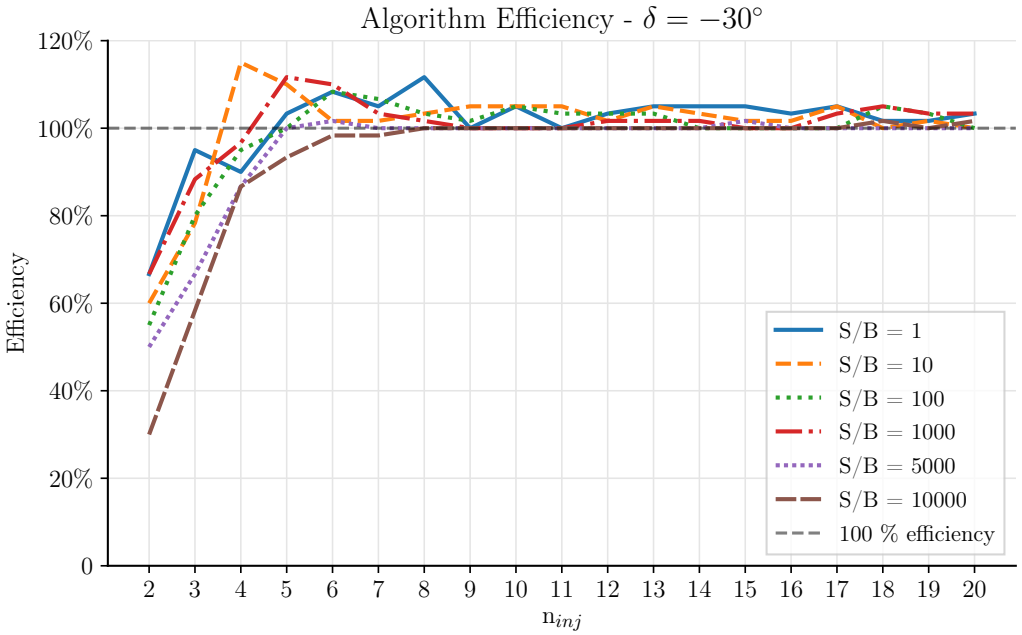

Figure 6.13: Efficiency of the Time-Clustering algorithm as a function of the injected signal for a source in the Northern Sky ($\delta = -30°$). The efficiency represents the number of produced alerts with respect to the total number of MonteCarlo maps.

discussed this result in Section 6.2.3 and we reported all the plots concerning the reconstruction of the fit parameters in Appendix A.1. These results suggest that using S/B ratios above 1000 prevents us from properly recognising all the events that contribute to the flare, thus losing efficiency in our analysis.

Our results show that at very high S/B thresholds we lose efficiency in our analysis. On the other hand, for low S/B ratios, we don't observe substantial changes in the GFU analysis for catalogue sources, but the lower trigger rates allow us to reduce the computational time

needed to run the Time-Clustering algorithm up to almost a factor 2 for a S/B = 100 (see Table 6.2). The reduction of the computational time needed to run the analysis allows the implementation of more precise and time-consuming algorithms during the reconstruction and filtering procedure, which could improve the purity of the events and, consequently, the significance of the alerts.

Finally, we proved that using a low S/B threshold ensures to recognise the neutrino flares earlier with respect to higher S/B thresholds. So, for real-time studies, it's more convenient to use low S/B thresholds.

Chapter 7

Conclusions and Future Outlook

In this work, we studied the performances of the Gamma-ray Follow-Up analysis for catalogue sources, with the purpose of improving them. This is done by reproducing the historical results concerning the test statistics distributions, the sensitivity curves and the reconstruction of the fit parameters, and also through the offline reproduction of the GFU neutrino alerts and the study of the systematic differences between the results obtained from the real-time online analysis and the offline ones. Subsequently, a detailed study of the typical characteristics of the GFU neutrino alerts is performed, and a strategy to increase the signal-to-background ratio of the alerts is presented.

We performed several tests changing the minimum S/B threshold that the events need to have to trigger the Time-Clustering algorithm, which produces the neutrino alerts, and we discussed the effects on the performances of the likelihood fit and on the production of the alerts.

Our results show that, regardless of the chosen S/B ratio, the Time-Clustering algorithm always manages to reconstruct the characteristics of the simulated flares, except for a slight underestimation of the number of events that contribute to the alert at very high S/B thresholds.

On the other hand, we observe a loss in the efficiency of the Time-Clustering algorithm for what concerns the production of alerts. Especially for small signal strengths, the algorithm isn't capable of producing an alert for each simulated flare, and the efficiency decreases at increasing S/B ratios. In the case of intermediate or strong signal strengths, instead, the algorithm manages to recognise the simulated flares and produce an alert for all the tested S/B ratios.

In particular, for low S/B thresholds, we don't observe significant changes in the performance of the algorithm but we see a decrease in the trigger rate and a consequent reduction of the computational time needed to run the algorithm. This means that, by rising the S/B ratio to these values, we reject triggers below the 3σ alert threshold, allowing for a faster analysis with unchanged performances.

The reduction of the computational time at low thresholds represents a key point of our results. In fact, it allows the implementation of more precise and time-consuming algorithms in the reconstruction and filtering procedures that would be too computationally demanding otherwise.

We observed that acting on the algorithm we don't improve the performance of the analysis, but a better directional reconstruction of the event tracks and a smaller angular uncertainty

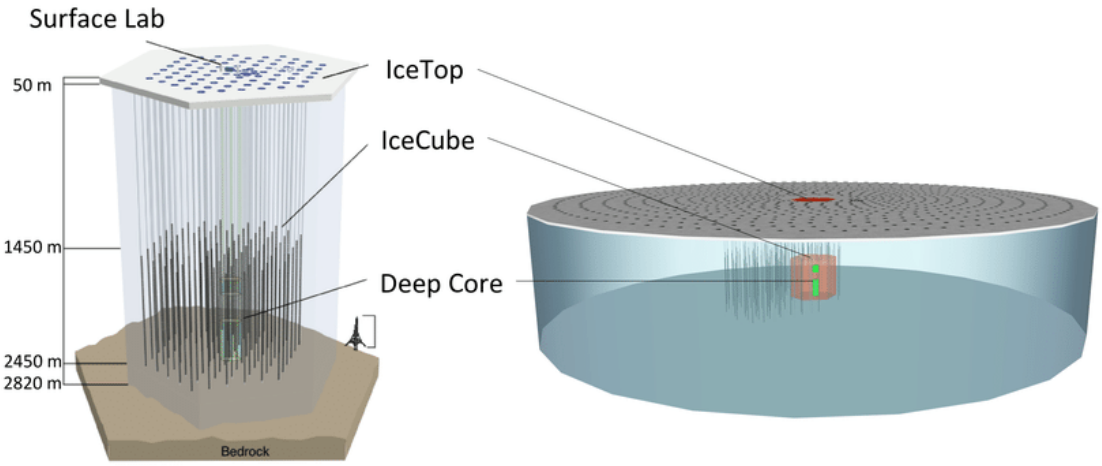

Figure 7.1: Left: current configuration of IceCube neutrino observatory. Right: sketch of IceCube-Gen2 with an extended version of the surface veto. (Image credit: `https://www.researchgate.net/publication/283017058_IceCube-Gen2_-_The_Next_Generation_Neutrino_Observatory_at_the_South_Pole_Contributions_to_ICRC_2015/figures?lo=1`)

would probably enhance the probability of identifying significant neutrino flares. For example, it was proven that running more iterations of the current algorithms for the directional reconstruction improves the track quality, but, up to now, it wasn't possible to apply this strategy due to the need of having a fast real-time analysis. Moreover, new techniques involving neural networks are starting to be implemented for other analyses and could represent a useful tool to improve the angular direction and the quality of the reconstruction of the tracks.

Additionally, an upgrade of the performance of the detector would also contribute to the improvement of the performance of the analysis. The upcoming IceCube-Gen2, sketched in Figure 7.1 will be a 10 km^3 volume detector. It will increase the annual rate of observed astrophysical neutrinos by a factor ten, and it will be able to detect sources five times fainter than its predecessor [77]. Such a large volume detector will allow to reveal astrophysical neutrinos having energies up to the EeV range and it will provide a better sensitivity at lower energy ranges.

The search for point-like sources of astrophysical neutrinos will surely benefit from the Gen2 improvements, increasing the probability of revealing new sources and shading light on the origin and production mechanisms of astrophysical neutrinos.

Appendix A

Plots

A.1 Reconstruction of Fit Parameters

In this appendix, we report all the results concerning the test of the performances of the Time-Clustering algorithm raising the S/B ratio. The algorithm is described in detail in Section 4.2.2, and the comments about the performances of the algorithm at different S/B ratios are reported in Section 6.2.3.

We show the results for both a simulated source located in the Southern Sky (Figures A.1, A.2, A.3) and for a source located in the Northern Sky (Figures A.4, A.5, A.6).

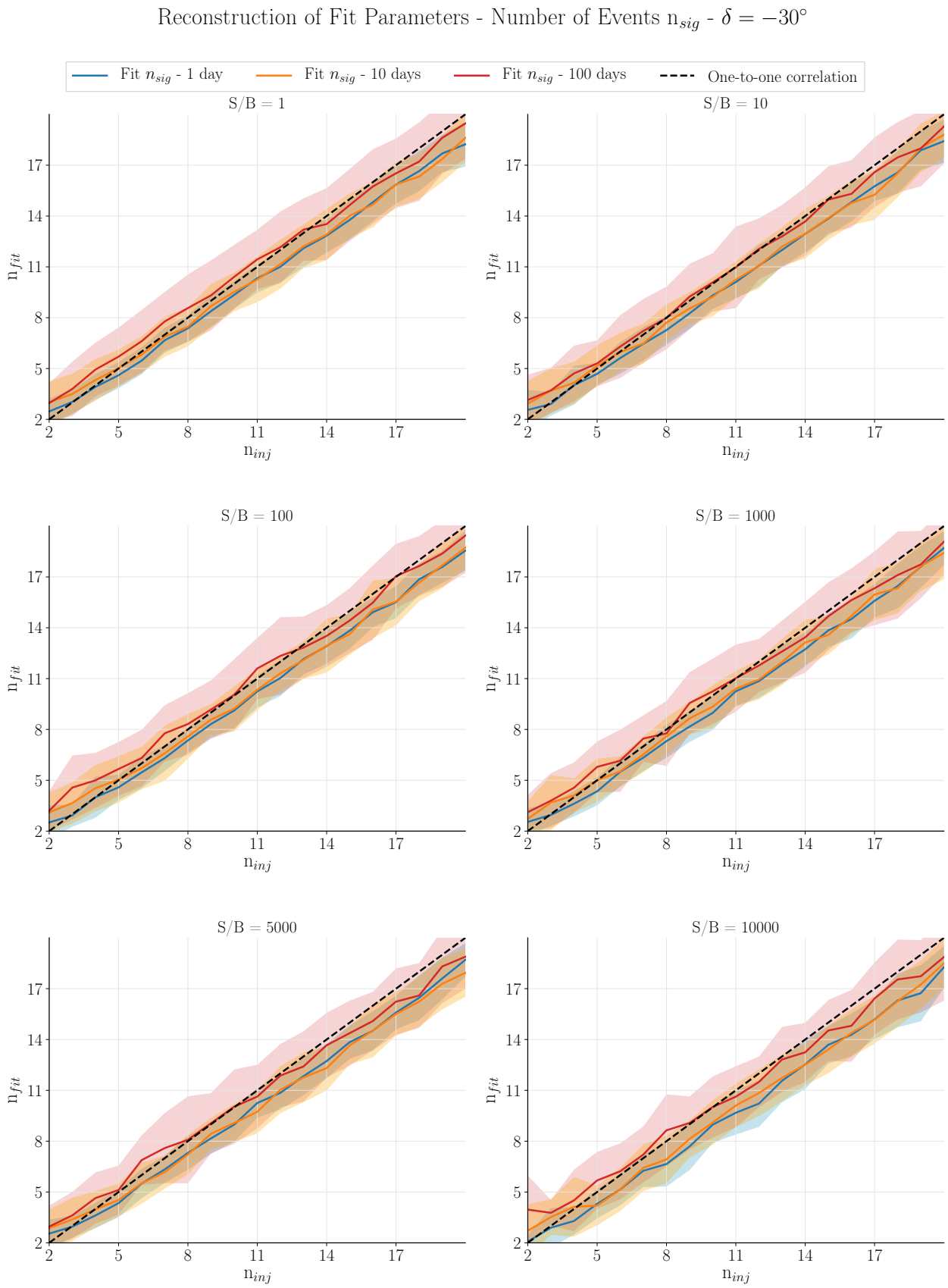

Figure A.1: Reconstruction of the number of injected events for all the tested S/B ratios. The results displayed in this picture are obtained from time-dependent simulations of flares of three different duration (1 day, 10 days, 100 days) from a source located at a declination $\delta = -30°$. The flares are simulated with a spectral index $\gamma = -2$ and a number of injected events that ranges from 2 to 20. The solid lines represent the average reconstructed n_{sig}. The shaded areas represent the 68% probability contours.

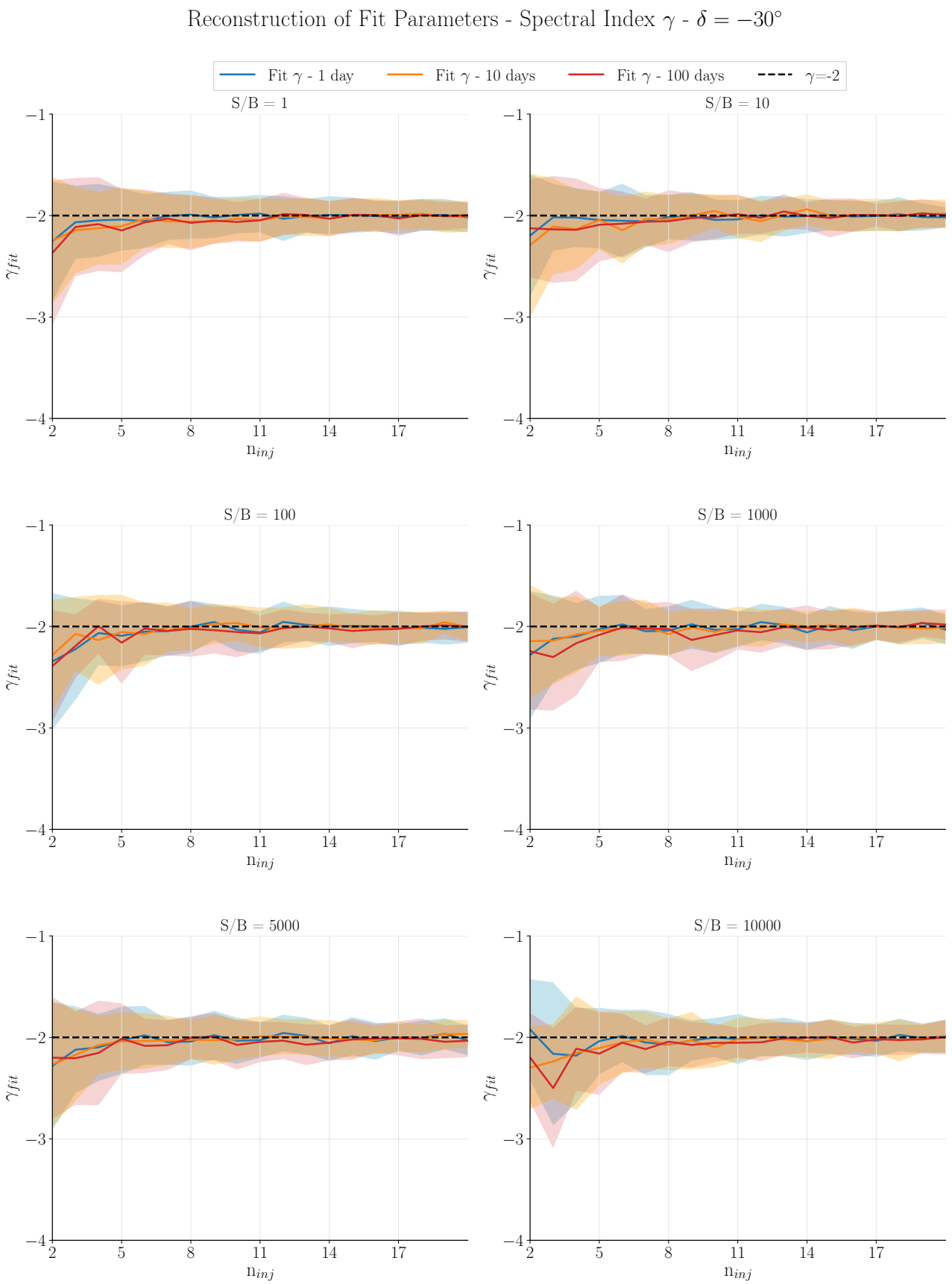

Figure A.2: Reconstruction of the spectral index γ for all the tested S/B ratios. The results displayed in this picture are obtained from time-dependent simulations of flares of three different duration (1 day, 10 days, 100 days) from a source located at a declination $\delta = -30°$. The flares are simulated with a spectral index $\gamma = -2$ and a number of injected events that ranges from 2 to 20. The solid lines represent the average reconstructed γ. The shaded areas represent the 68% probability contours.

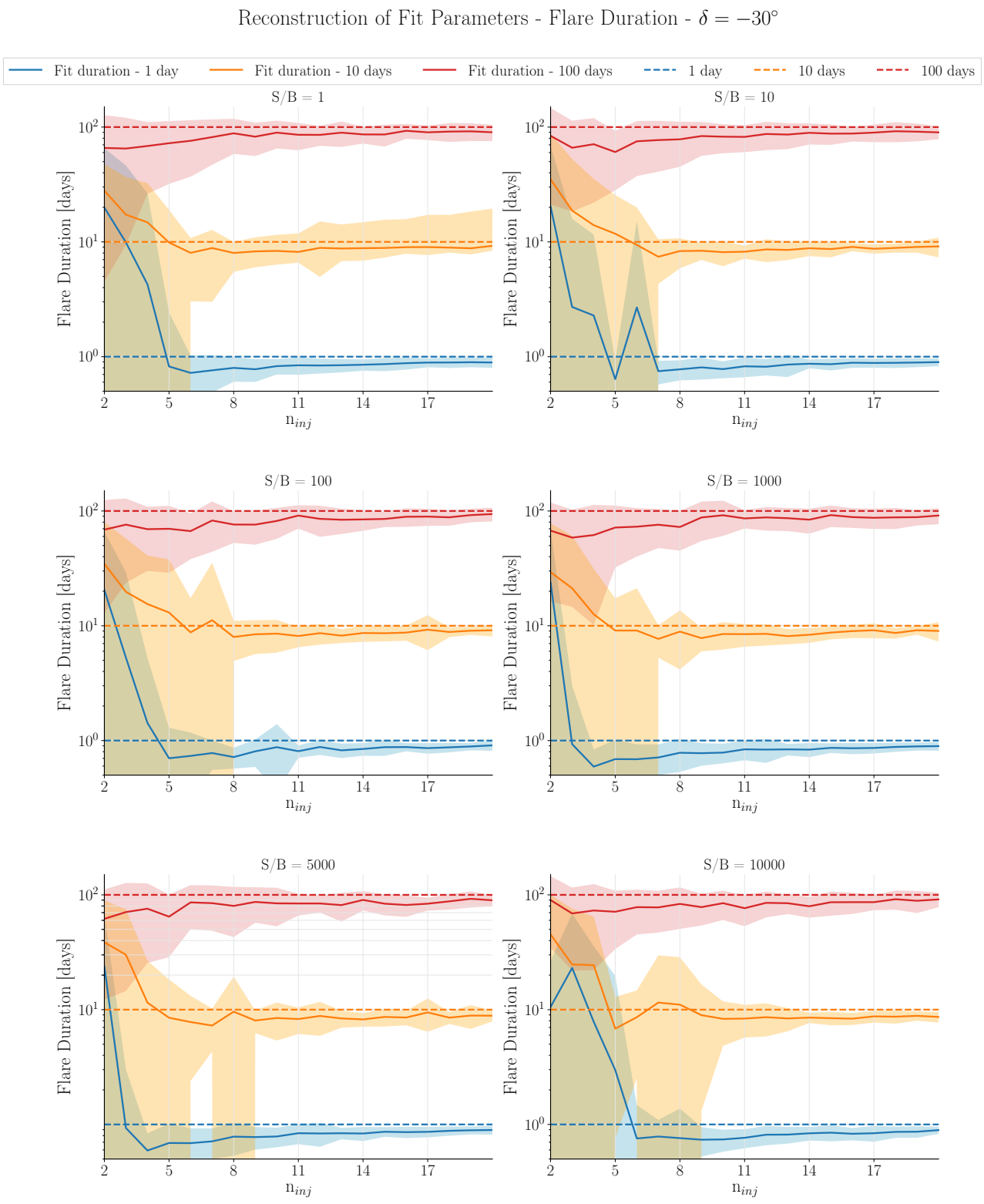

Figure A.3: Reconstruction of the duration of the flare for all the tested S/B ratios. The results displayed in this picture are obtained from time-dependent simulations of flares of three different duration (1 day, 10 days, 100 days) from a source located at a declination $\delta = -30°$. The flares are simulated with a spectral index $\gamma = -2$ and a number of injected events that ranges from 2 to 20. The solid lines represent the average reconstructed flare duration. The shaded areas represent the 68% probability contours.

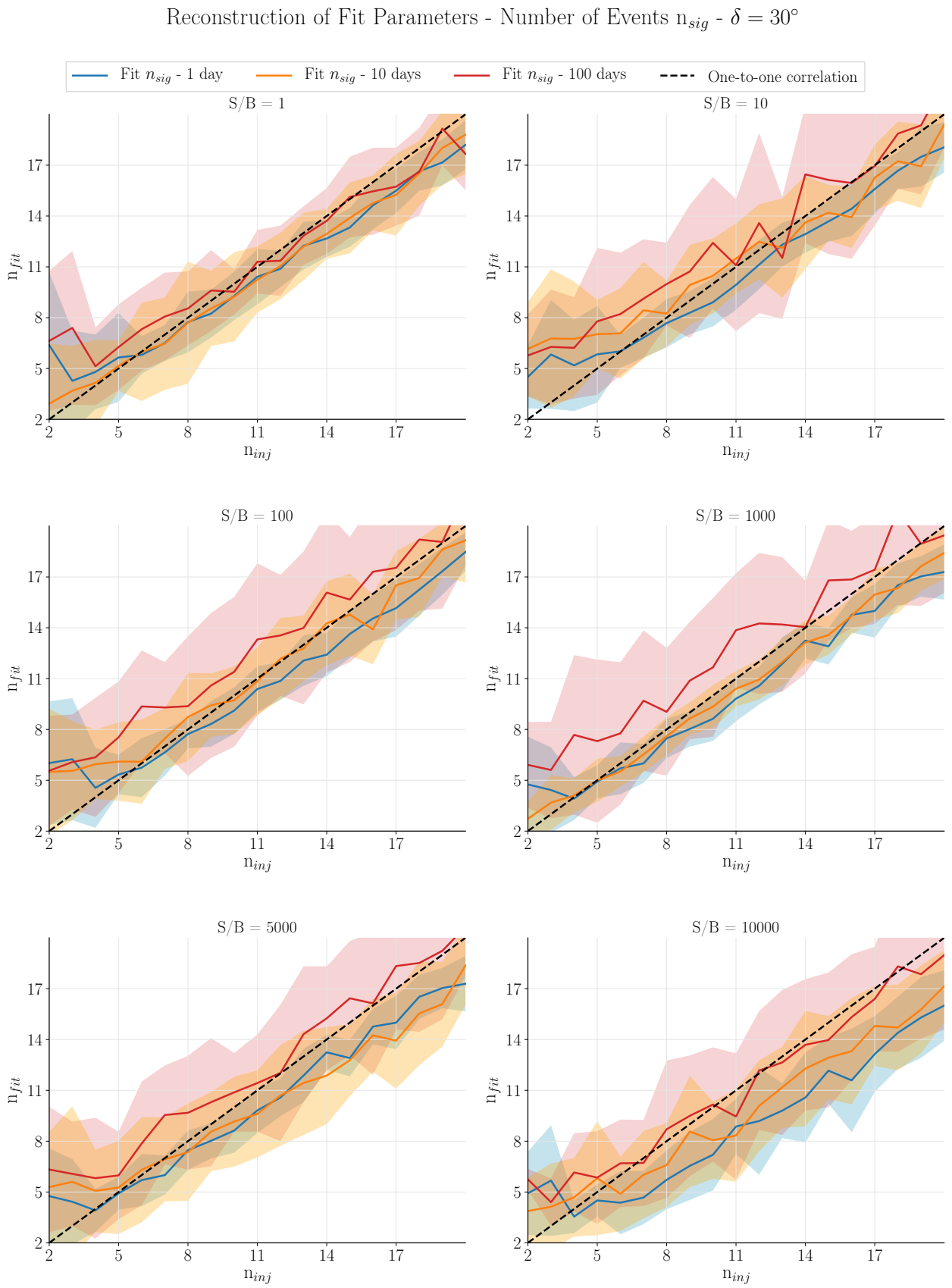

Figure A.4: Reconstruction of the number of injected events for all the tested S/B ratios. The results displayed in this picture are obtained from time-dependent simulations of flares of three different duration (1 day, 10 days, 100 days) from a source located at a declination $\delta = 30°$. The flares are simulated with a spectral index $\gamma = -2$ and a number of injected events that ranges from 2 to 20. The solid lines represent the average reconstructed n_{sig}. The shaded areas represent the 68% probability contours.

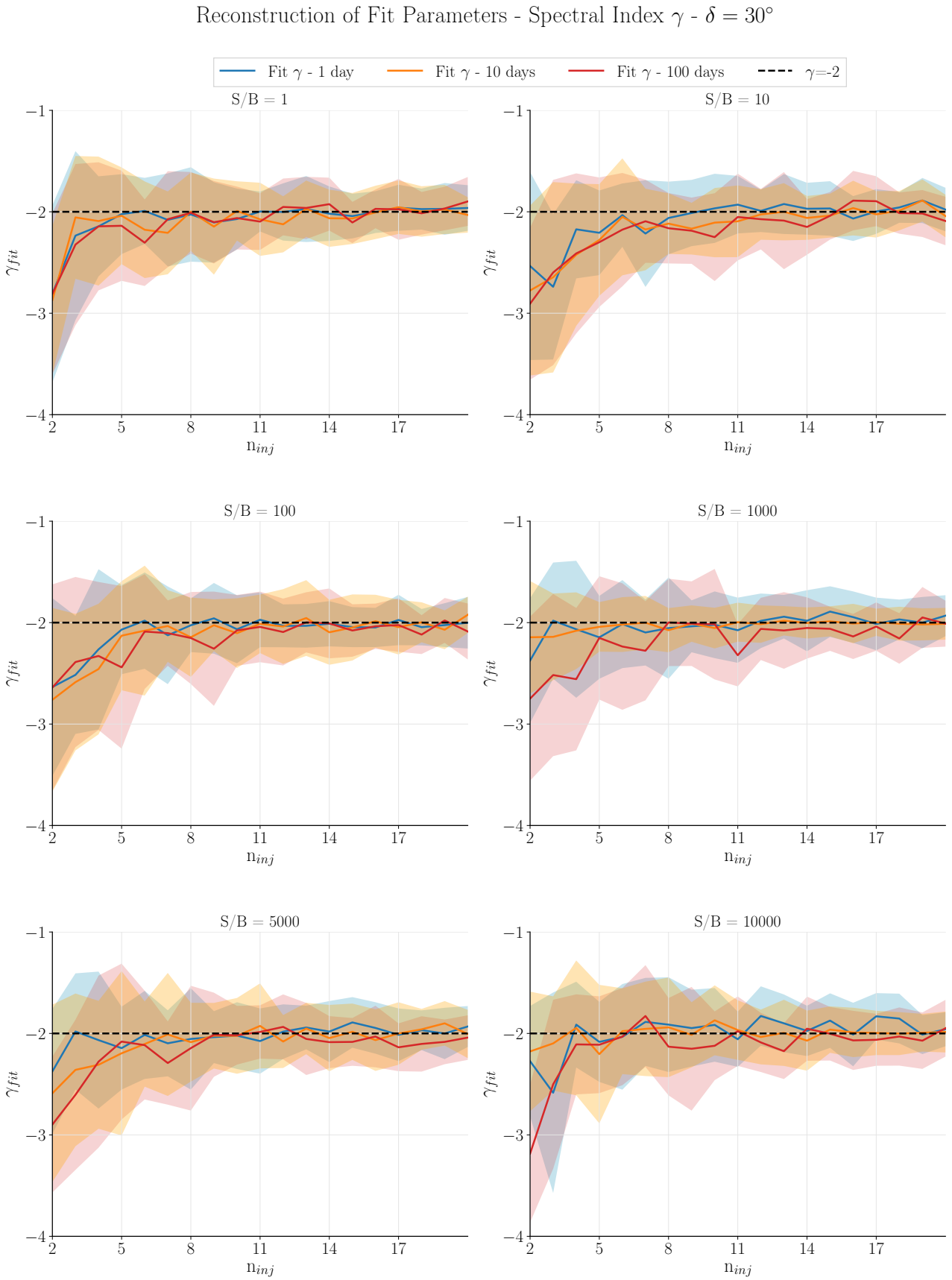

Figure A.5: Reconstruction of the spectral index γ for all the tested S/B ratios. The results displayed in this picture are obtained from time-dependent simulations of flares of three different duration (1 day, 10 days, 100 days) from a source located at a declination $\delta = 30°$. The flares are simulated with a spectral index $\gamma = -2$ and a number of injected events that ranges from 2 to 20. The solid lines represent the average reconstructed γ. The shaded areas represent the 68% probability contours.

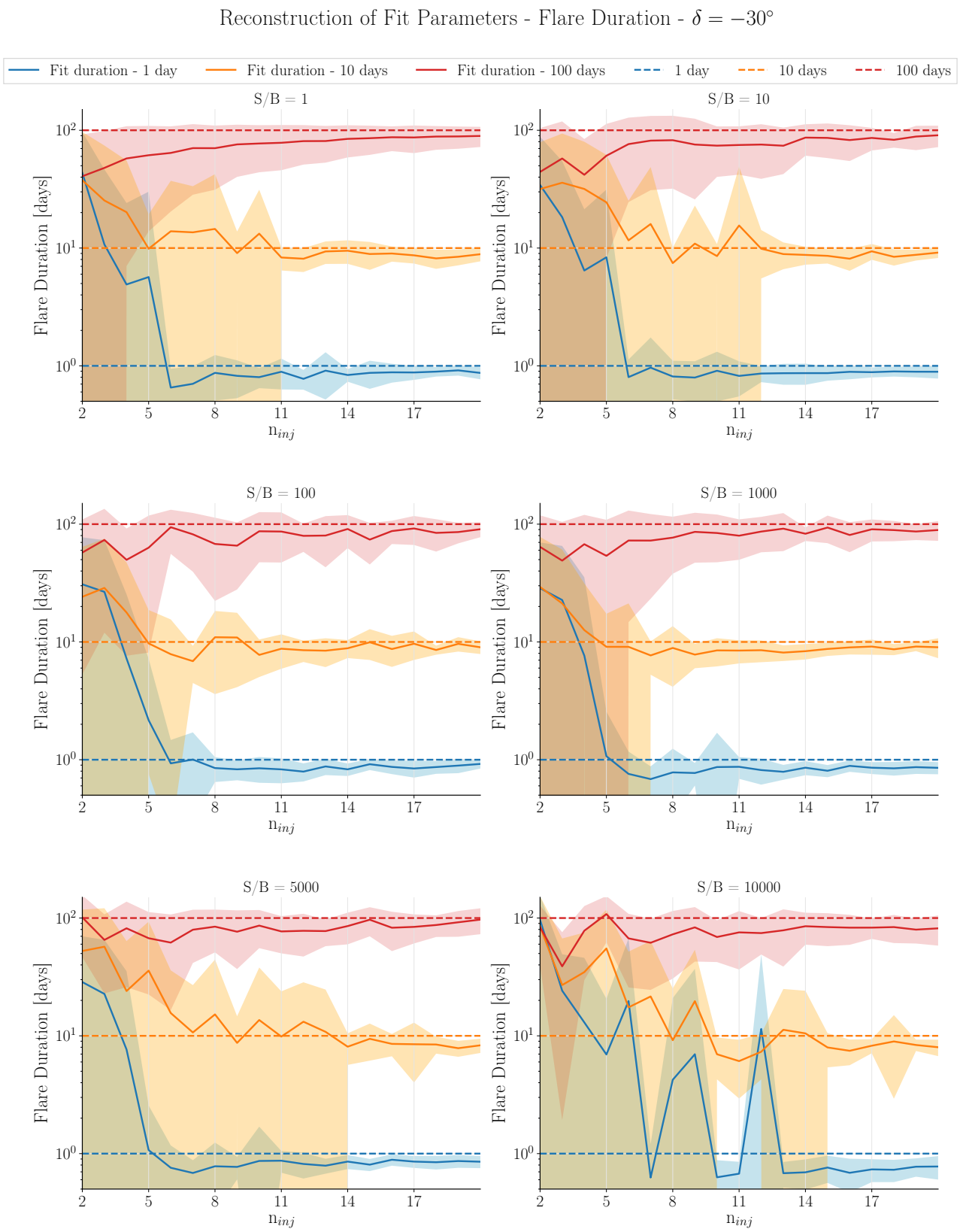

Figure A.6: Reconstruction of the duration of the flare for all the tested S/B ratios. The results displayed in this picture are obtained from time-dependent simulations of flares of three different duration (1 day, 10 days, 100 days) from a source located at a declination $\delta = 30°$. The flares are simulated with a spectral index $\gamma = -2$ and a number of injected events that ranges from 2 to 20. The solid lines represent the average reconstructed flare duration. The shaded areas represent the 68% probability contours.

A.2 Typical Characteristics of the Alerts

In this section, we report the distribution of the events that contribute to the alerts as a function of the relevant parameter explained in Section 6.1 for all the tested S/B ratios. A summary of the results can be found in Section 6.2.4.

We show the results for both a simulated source located in the Southern Sky (Figures A.7 and A.9) and for a source located in the Northern Sky (Figures A.8 and A.10).

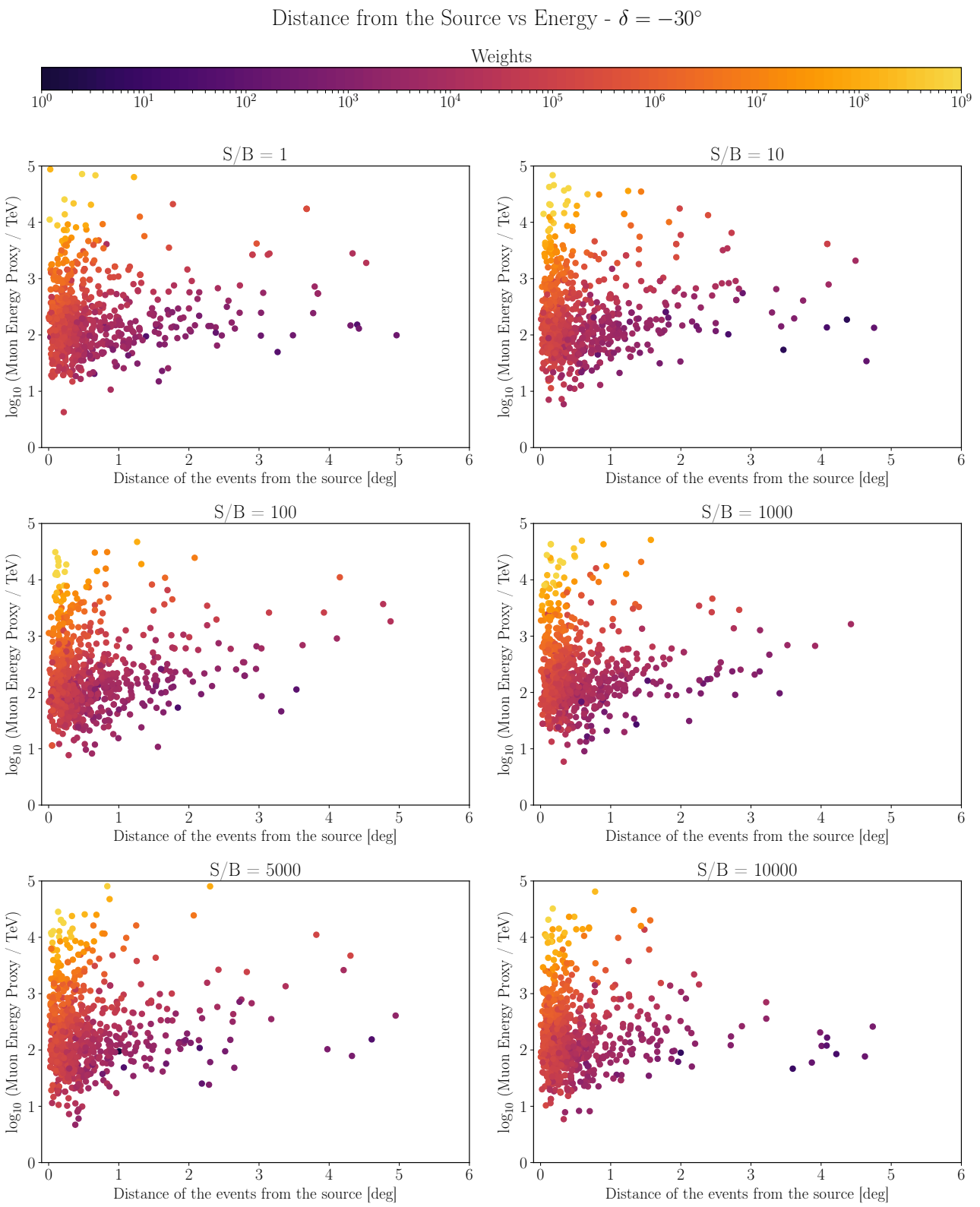

Figure A.7: Distribution of the events that contribute to the alerts as a function of their energy, distance from the source and weight for a simulated source at $\delta = -30°$ for all the tested S/B ratios.

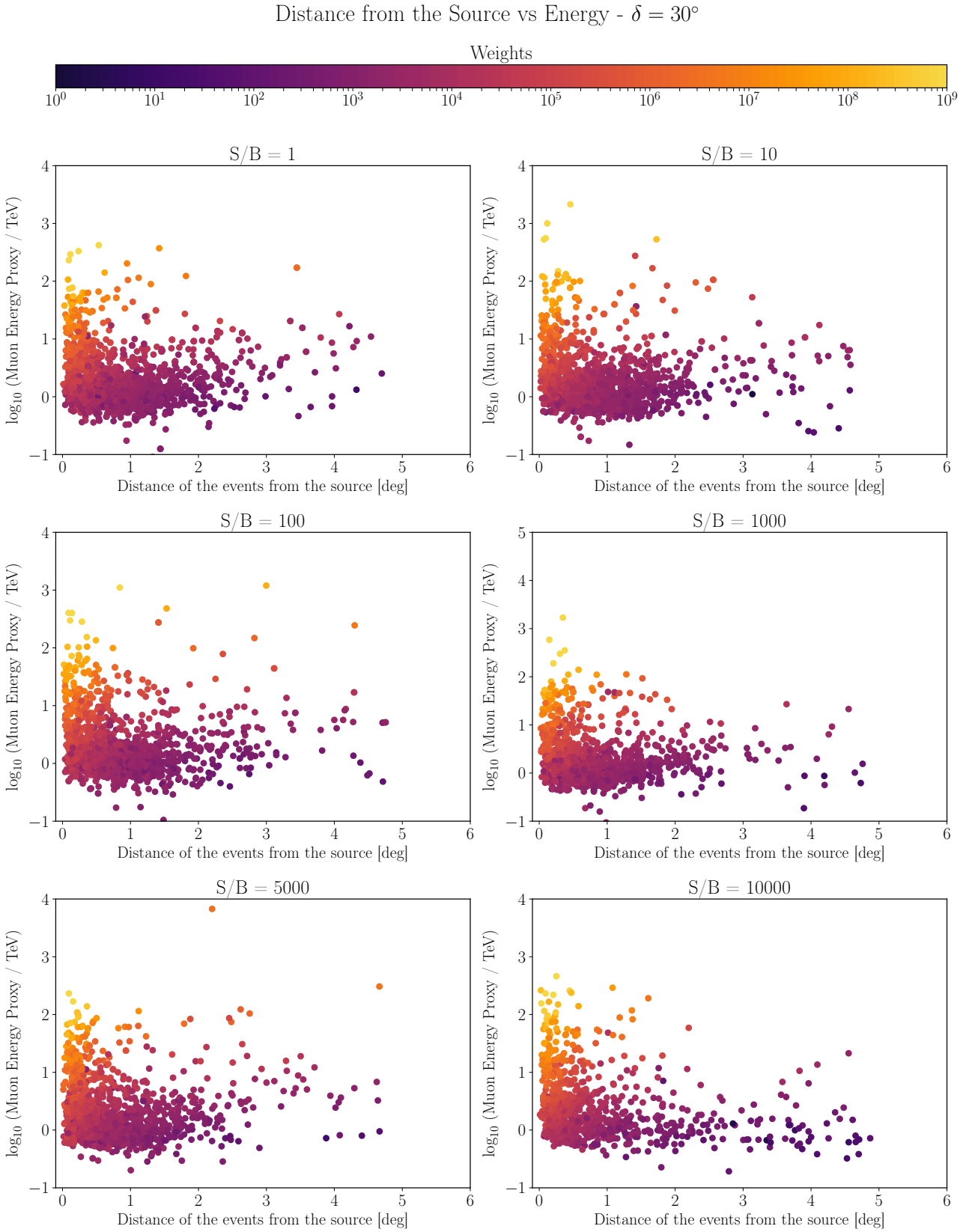

Figure A.8: Distribution of the events that contribute to the alerts as a function of their energy, distance from the source and weight for a simulated source at $\delta = 30°$ for all the tested S/B ratios.

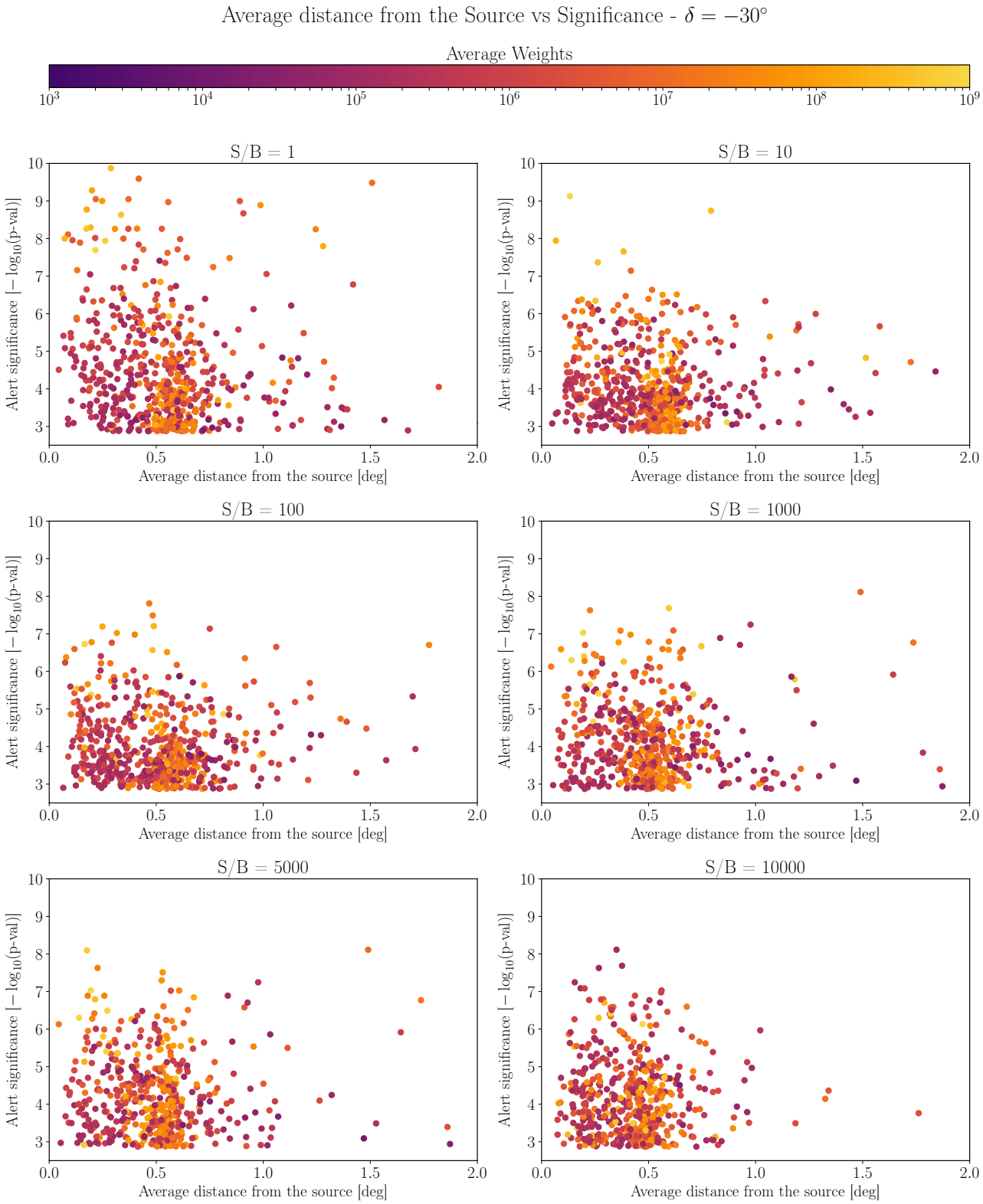

Figure A.9: Distribution of the significance of the alerts as a function of the average distance of the events from the source for each of the tested S/B ratios. The colour code represents the average weight of the events.

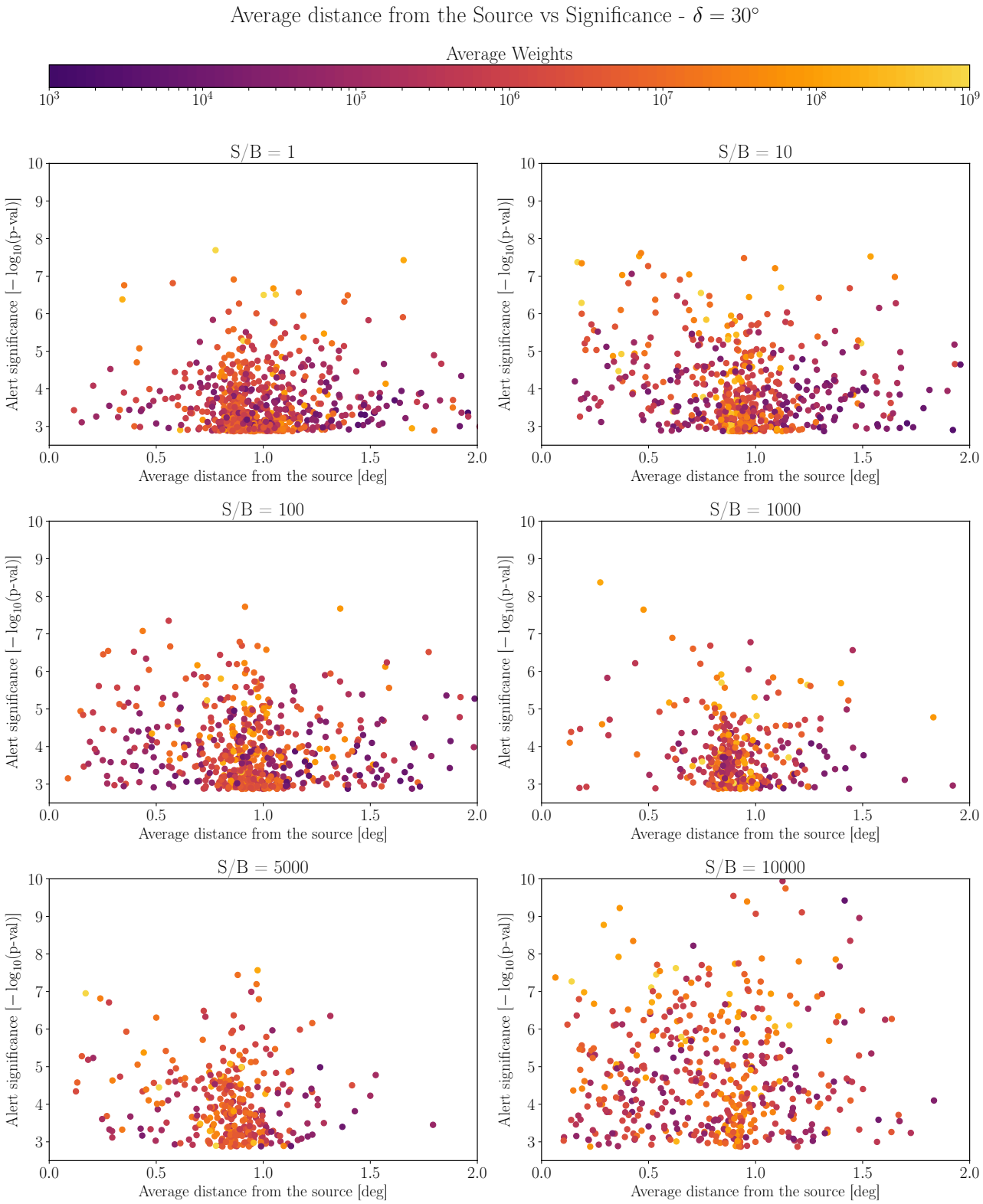

Figure A.10: Distribution of the significance of the alerts as a function of the average distance of the events from the source for each of the tested S/B ratios. The colour code represents the average weight of the events.

Acknowledgements

I would like to thank Elisa Bernardini for introducing me to multi-messenger astrophysics and guiding me through my thesis work. I always felt welcome and appreciated and I will always treasure the advice you've given me.

I would also like to thank Caterina Boscolo Meneguolo and Ilaria Viale for hosting me in their office and being so patient in answering my phone calls at any hour asking them to come open the corridor door for me. You have been the nicest office mates during these months.

Bibliography

[1] V. Hess, "Über beobachtungen der durchdringenden strahlung bei sieben freiballonfahrten, [on observations of penetrating radiation during seven free balloon flights]," *Physikalische Zeitschrift*, 1912.

[2] M. G. Aartsen *et al.*, "Evidence for high-energy extraterrestrial neutrinos at the icecube detector," *Science*, 2013.

[3] M. G. Aartsen *et al.*, "Icecube data for neutrino point-source searches: Years 2008–2018," *Physical Review Letters*, 2019.

[4] M. G. Aartsen *et al.*, "The icecube realtime alert system," *Astroparticle Physics*, 2017.

[5] M. Aartsen *et al.*, "Multi-messenger observations of a flaring blazar coincident with high-energy neutrino icecube-170922a," *Science*, 2018.

[6] B. Abbot *et al.*, "Ligo: The laser interferometer gravitational-wave observatory," *Reports on Progress in Physics*, 2007.

[7] "Fermi gamma-ray space telescope." `https://fermi.gsfc.nasa.gov/`. (accessed: 12.08.2022).

[8] B. Abbot *et al.*, "Multi-messenger observations of a binary neutron star merger," *Astrophysical Journal Letters*, 2017.

[9] K. Greisen, "End to the cosmic-ray spectrum?," *Physical Review Letters*, 1966.

[10] F. G. Schröoder, "Radio detection of extensive air showers," *XXV European Cosmic Ray Symposium*, 2016.

[11] A. Bykov, D. Ellison, A. Marcowith, and S. Osipov, "Cosmic ray production in supernovae," *Space Science Reviews*, 2018.

[12] M. Ackermann *et al.*, "Detection of the characteristic pion-decay signature in supernova remnants," *Science Magazine*, 2013.

[13] J. Abraham *et al.*, "Correlation of the highest-energy cosmic rays with the positions of nearby active galactic nuclei," *Astroparticle Physics*, 2008.

[14] P. M. Bauleo and J. R. Martino, "The dawn of the particle astronomy era in ultra-high-energy cosmic rays," *Nature*, 2009.

[15] A. de Angelis and M. Pimenta, *Introduction to Particle and Astroparticle Physics*. Springer, 2018. (See Chapter 10).

[16] J. W. V. Thomas Schwetz, Mariam Tortola, "Three-flavour neutrino oscillation update," *New Journal of Physics*, 2008.

[17] "Super kamiokande experiment." https://www-sk.icrr.u-tokyo.ac.jp/sk/publications/result-e.html. (accessed: 13.08.2022).

[18] "T2k experiment." https://t2k-experiment.org/. (accessed: 13.08.2022).

[19] "Juno experiment." http://juno.ihep.cas.cn/. (accessed: 13.08.2022).

[20] C. Spieringo, "Towards high-energy neutrino astronomy - a historical review," *European Physics Journal*, 2012.

[21] J. F. Babson *et al.*, "Cosmic rays muons in the deep ocean," *Physics Review*, 1990.

[22] C. Spiering *et al.*, "The baikal experiment," *Astrophysics and Particle Physics*, 1990.

[23] V. A. Balkanov *et al.*, "Registration of atmospheric neutrinos with the baikal neutrino telescope nt-96," *Astroparticle Physics*, 1999.

[24] "Antares." https://antares.in2p3.fr/. (accessed: 07.08.2022).

[25] E. Andrés *et al.*, "The amanda experiment," *Astrophysical Journal*, 1997.

[26] "Icecube neutrino observatory." https://icecube.wisc.edu/. (accessed: 07.08.2022).

[27] M. Aartsen *et al.*, "Detection of a particle shower at the glashow resonance with icecube," *Nature*, 2021.

[28] E. Waxman and J. Bahcall, "High energy neutrinos from astrophysical sources: An upper bound," *Physics Review*, 1998.

[29] J. Stettner, "Measurement of the diffuse astrophysical muon-neutrino spectrum with ten years of icecube data," *36th International Cosmic Ray Conference (ICRC2019)*, 2019.

[30] R. Abbasi *et al.*, "Searches for neutrinos from gamma-ray bursts using the icecube neutrino observatory," *arXiv:2205.11410[astro-ph.HE]*, 2022.

[31] J. Aleksić *et al.*, "The major upgrade of the magic telescopes, part i: The hardware improvements and the commissioning of the system," *Astroparticle Physics*, 2014.

[32] J. Aleksić *et al.*, "The major upgrade of the magic telescopes, part ii: A performance study using observations of the crab nebula," *Astroparticle Physics*, 2014.

[33] J. Holder *et al.*, "Status of the veritas observatory," *in 4th Heidelberg International Symposium on High-Energy Gamma Ray Astronomy*, 2008.

[34] M. de Naurois, "H.e.s.s.-ii - gamma ray astronomy from 20 gev to hundreds of tev's," *in 6th Roma International Workshop on Astroparticle Physics (RICAP)*, 2016.

[35] R. Zanin, "Cherenkov telescope array: the world's largest vhe gamma-ray observatory," *PoS ICRC2021*, 2021.

[36] S. E. Woosley and J. S. Bloom, "The supernova gamma-ray burst connection," *Annual Review of Astronomy and Astrophysics*, 2006.

[37] A. Einstein, "Die grundlage der allgemeinen relativit ätstheorie," *Ann. Phys.*, 1916.

[38] B. Abbot *et al.*, "Observation of gravitational waves from a binary black hole merger," *Physical Review Letters*, 2016.

[39] S. Vitale, "The first 5 years of gravitational-wave astrophysics," *Science*, 2021.

[40] A. Albert *et al.*, "Search for multi-messenger sources of gravitational waves and high-energy neutrinos with advanced ligo during its first observing run, antares and icecube," *Astrophysical Journal*, 2018.

[41] "Baikal-gvd." `https://baikalgvd.jinr.ru/`. (accessed: 07.08.2022).

[42] "Km3net." `https://www.km3net.org/`. (accessed: 07.08.2022).

[43] "P-one." `https://www.pacific-neutrino.org/`. (accessed: 07.08.2022).

[44] M. Ackermann *et al.*, "Optical properties of deep glacial ice at the south pole," *Journal of Geophysical Research*, 2006.

[45] P. Askebjer *et al.*, "Optical properties of deep ice at the south pole: absorption," *Applied Optics*, 1997.

[46] J. R. Petit *et al.*, "Climate and atmospheric history of the past 420,000 years from the vostok ice core, antarctica," *Nature*, 1999.

[47] R. Abbasi *et al.*, "The icecube data acquisition system: Signal capture, digitization, and timestamping," *Nuclear Instrumentation Methods*, 2009.

[48] M. Aartsen *et al.*, "Energy reconstruction methods in the icecube neutrino telescope," *Journal of Instrumentation*, 2016.

[49] A. Achterberg *et al.*, "First year performance of the ice cube neutrino telescope," *Astroparticle Physics*, 2008.

[50] T. Kintscher, *Rapid Response to Extraordinary Events: Transient Neutrino Sources with the IceCube Experiment*. PhD thesis, Humboldt Universität zu Berlin, 2020.

[51] M. Aartsen *et al.*, "Search for astrophysical sources of neutrinos using cascade events in icecube," *Astrophysical Journal*, 2017.

[52] "Gcn/amon notices." `https://gcn.gsfc.nasa.gov/amon.html`. (accessed: 07.08.2022).

[53] M. Ackermann, E. Bernardini, N. Galante, F. Goebel, M. Hayashida, K. Satalecka, M. Tluczykont, and R. M. Wagner, "Neutrino triggered target of opportunity (ntoo) test run with amanda-ii and magic," *ICRC 2007*, 2007.

[54] M. G. Aartsen *et al.*, "The icecube neutrino observatory: instrumentation and online systems," *Journal of Instrumentation*, 2017.

[55] D. Pandel, *Destimmung von Wasser- und Detektorparametern und Rekonstruktion von Myonen bis 100 TeV mit dem Baikal-Neutrinoteleskop NT-72*. PhD thesis, Diploma Thesis, Humboldt Universität zu Berlin, 1996.

[56] J. Ahrens *et al.*, "Muon track reconstruction and data selection techniques in amanda," *Nuclear Instruments & Methods A*, 2004.

[57] M. Voge, *Searches for Neutrinos from Supernovae Using Cherenkov In-Ice Detectors*. PhD thesis, Rheinischen Friedrich-Wilhelms-Universität Bonn, 2016. (see pp. 115-117).

[58] N. Whitehorn, J. van Santen, and S. Lafebre, "Penalized splines for smooth representation of high-dimensional monte carlo datasets," *Computer Physics Communications*, 2018.

[59] F. Pedregosa *et al.*, "Scikit-learn: Machine learning in python," *Journal of Machine Learning Research*, 2011.

[60] M. G. Aartsen *et al.*, "Lowering icecube's energy threshold for point source searches in the southern sky," *The Astrophysical Journal*, 2016.

[61] C. F. Tung, "The next generation of icecube realtime neutrino alerts," *36th International Cosmic Ray Conference -ICRC2019-*, 2019.

[62] H. Cramér, . *Mathematical Methods of Statistic*. Princeton: Princeton University Press, 1999.

[63] M. Aartsen *et al.*, "Very high-energy gamma-ray follow-up program using neutrino triggers from icecube," *JNIST*, 2016.

[64] B. Efron, "Bootstrap methods: Another look at the jackknife," *The Annals of Statistics*, 1979.

[65] R. Abbasi *et al.*, "All-sky search for time-integrated neutrino emission from astrophysical sources with 7 years of icecube data," *Astrophysical Journal*, 2016.

[66] A. Pizzuto, A. Desai, and R. Hussain, "Realtime follow-up of astrophysical transients with the icecube neutrino observatory," *37th International Cosmic Ray Conference (ICRC 2021)*, 2021.

[67] P. Correa, "Searching for high-energy neutrinos from ultra-luminous infrared galaxies with icecube," *Journal of Physics: Conference Series*, 2022.

[68] R. Abbasi *et al.*, "Search for high-energy neutrino emission from galactic x-ray binaries with icecube," *The Astrophysical Journal Letters*, 2022.

[69] J. Braun, J. Dumm, F. D. Palma, C. Finley, A. Karle, and T. Montaruli, "Methods for point source analysis in high energy neutrino telescopes," *Astroparticle Physics*, 2008.

[70] R. Abbasi *et al.*, "Time-integrated searches for point-like sources of neutrinos with the 40-string icecube detector," *Astrophysical Journal*, 2011.

[71] M. L. Ahnen *et al.*, "Detection of very high energy gamma-ray emission from the gravitationally-lensed blazar qso b0218+357 with the magic telescopes," *Astronomy & Astrophysics*, 2016.

[72] "Healpix." `https://healpix.sourceforge.io/`. (accessed: 01.08.2022).

[73] G. Feldman and R. Cousins, "A unified approach to the classical statistical analysis of small signals," *Physics Review*, 1999.

[74] C. E. Bonferroni, *Teoria statistica delle classi e calcolo delle probabilità*. Istituto Superiore di Scienze Economiche e Commerciali di Firenze, 1936.

[75] "Modified julian dates (mjd)." `https://core2.gsfc.nasa.gov/time/`. (accessed: 23.08.2022).

[76] "Json format." `https://developer.mozilla.org/en-US/docs/Learn/JavaScript/Objects/JSON`. (accessed: 31.08.2022).

[77] M. G. Aartsen *et al.*, "Icecube-gen2: the window to the extreme universe," *Journal of Physics G: Nuclear and Particle Physics*, 2021.